

# LTE Technology: Antenna, RF Front-Ends, and Channel Modeling

Guest Editors: Qingfeng Zhang, Sai Wai Wong, Cheng Jin, Xiu Yin Zhang,  
Yifan Chen, Dimitrios Sounas, and Nima Chamanara



---



## **LTE Technology: Antenna, RF Front-Ends, and Channel Modeling**

## **LTE Technology: Antenna, RF Front-Ends, and Channel Modeling**

Guest Editors: Qingfeng Zhang, Sai Wai Wong, Cheng Jin,  
Xiu Yin Zhang, Yifan Chen, Dimitrios Sounas,  
and Nima Chamanara



Copyright © 2015 Hindawi Publishing Corporation. All rights reserved.

This is a special issue published in "International Journal of Antennas and Propagation." All articles are open access articles distributed under the Creative Commons Attribution License, which permits unrestricted use, distribution, and reproduction in any medium, provided the original work is properly cited.

## Editorial Board

Ana Alejos, Spain	Feifei Gao, China	Marco Mussetta, Italy
Mohammad Ali, USA	Junping Geng, China	N. Nasimuddin, Singapore
Jaume Anguera, Spain	Claudio Gennarelli, Italy	Miguel Navarro-Cia, UK
Ercument Arvas, USA	Rocco Guerriero, Italy	Mourad Nedil, Canada
Alexei Ashikhmin, USA	Kerim Guney, Turkey	Symeon Nikolaou, Cyprus
Herve Aubert, France	Song Guo, Japan	Giacomo Oliveri, Italy
Paolo Baccarelli, Italy	Qian He, China	Athanasisos D. Panagopoulos, Greece
Xiulong Bao, Ireland	Mohamed Himdi, France	Ikmo Park, Korea
Toni Björninen, Finland	Heng-Tung Hsu, Taiwan	Matteo Pastorino, Italy
Djuradj S. Budimir, UK	Jun Hu, China	Mugen Peng, China
Paolo Burghignoli, Italy	Tamer S. Ibrahim, USA	Massimiliano Pieraccini, Italy
Shah N. Burokur, France	Mohammad T. Islam, Malaysia	Xianming Qing, Singapore
Giuseppe Castaldi, Italy	Weixiang Jiang, China	Ahmad Safaai-Jazi, USA
Felipe Cátedra, Spain	M. R. Kamarudin, Malaysia	Safieddin Safavi-Naeini, Canada
Chih-Hua Chang, Taiwan	Kyeong Jin Kim, USA	Magdalena Salazar-Palma, Spain
Deb Chatterjee, USA	Ahmed A. Kishk, Canada	Stefano Selleri, Italy
Shih Yuan Chen, Taiwan	Slawomir Koziel, Iceland	John J. Shynk, USA
Yu Jian Cheng, China	Luis Landesa, Spain	Prabhakar Singh, India
Renato Cicchetti, Italy	Ding-Bing Lin, Taiwan	Raffaele Solimene, Italy
Lorenzo Crocco, Italy	Angelo Liseno, Italy	Seong-Youp Suh, USA
Claudio Curcio, Italy	Giampiero Lovat, Italy	Sheng Sun, Hong Kong
Francesco D'Agostino, Italy	Lorenzo Luini, Italy	Larbi Talbi, Canada
Maria E. De Cos, Spain	Atsushi Mase, Japan	Luciano Tarricone, Italy
Tayeb A. Denidni, Canada	Diego Masotti, Italy	Parveen Wahid, USA
Giuseppe Di Massa, Italy	Giuseppe Mazzarella, Italy	Yuanxun Ethan Wang, USA
Michele D'Urso, Italy	C. F. Mecklenbräuker, Austria	Wen-Qin Wang, China
Francisco Falcone, Spain	Massimo Migliozzi, Italy	Shiwen Yang, China
Quanyuan Feng, China	Mark Mirotznik, USA	Yuan Yao, China
Miguel Ferrando Bataller, Spain	Ahmed T. Mobashsher, Australia	Jingjing Zhang, Denmark
Flaminio Ferrara, Italy	Ananda S. Mohan, Australia	
Vincenzo Galdi, Italy	Jose-Maria Molina-Garcia-Pardo, Spain	

## Contents

**LTE Technology: Antenna, RF Front-Ends, and Channel Modeling**, Qingfeng Zhang, Sai Wai Wong, Cheng Jin, Xiu Yin Zhang, Yifan Chen, Dimitrios Sounas, and Nima Chamanara  
Volume 2015, Article ID 764178, 2 pages

**DOA Estimation for Mixed Uncorrelated and Coherent Sources in Multipath Environment**, Heping Shi, Wen Leng, Anguo Wang, and Tongfeng Guo  
Volume 2015, Article ID 636545, 8 pages

**Compact Unequal Power Divider with Filtering Response**, Wei-Qiang Pan, Jin-Xu Xu, Kai Xu Wang, and Xiao Lan Zhao  
Volume 2015, Article ID 658102, 7 pages

**2D Active Antenna Array Design for FD-MIMO System and Antenna Virtualization Techniques**, Ioannis Tzanidis, Yang Li, Gary Xu, Ji-Yun Seol, and JianZhong (Charlie) Zhang  
Volume 2015, Article ID 873530, 9 pages

**A CPW-Fed Quasi-PIFA Antenna Using Quasi-Lumped Resonators for Mobile Phones**, Majid Rafiee, Mohd Fadzil bin Ain, and Aftanasar Md. Shahar  
Volume 2015, Article ID 715958, 8 pages

**High Selectivity Dual-Band Bandpass Filter with Tunable Lower Passband**, Wei-Qiang Pan, Xiao-Lan Zhao, Yao Zhang, and Jin-Xu Xu  
Volume 2015, Article ID 762504, 6 pages

**Map-Based Channel Model for Urban Macrocell Propagation Scenarios**, Jose F. Monserrat, Saúl Inca, Jordi Calabuig, and David Martín-Sacristán  
Volume 2015, Article ID 172501, 5 pages

**Dual Zeroth-Order Resonant USB Dongle Antennas for 4G MIMO Wireless Communications**, Yan Shi, Lu Zhang, and Chang-Hong Liang  
Volume 2015, Article ID 816051, 8 pages

**The Communication Solution for LTE System under Radar Interference Circumstance**, Hang Zheng, Yunjie Li, and Yunpeng Zhu  
Volume 2015, Article ID 849695, 8 pages

## Editorial

# LTE Technology: Antenna, RF Front-Ends, and Channel Modeling

**Qingfeng Zhang,<sup>1</sup> Sai Wai Wong,<sup>2</sup> Cheng Jin,<sup>3</sup> Xiu Yin Zhang,<sup>2</sup> Yifan Chen,<sup>1</sup> Dimitrios Sounas,<sup>4</sup> and Nima Chamanara<sup>5</sup>**

<sup>1</sup>Department of Electronics and Electrical Engineering, South University of Science and Technology of China, Shenzhen 518055, China

<sup>2</sup>Department of Electronic and Information Engineering, South China University of Technology, Guangzhou 510640, China

<sup>3</sup>Center for Microwave Technology, Beijing Institute of Technology, Beijing 100081, China

<sup>4</sup>Department of Electrical and Computer Engineering, The University of Texas at Austin, Austin, TX 78712, USA

<sup>5</sup>Department of Electrical Engineering, École Polytechnique de Montréal, Montréal, QC, Canada H3T 1J4

Correspondence should be addressed to Qingfeng Zhang; zhang.qf@sustc.edu.cn

Received 10 June 2015; Accepted 11 June 2015

Copyright © 2015 Qingfeng Zhang et al. This is an open access article distributed under the Creative Commons Attribution License, which permits unrestricted use, distribution, and reproduction in any medium, provided the original work is properly cited.

Mobile communications are more and more involved in our daily life. The long term evolution (LTE) standard is proposed to provide high data rate due to the exploding demands for faster and ubiquitous communication nowadays. It has dramatically driven the technology advances in wireless communication systems. This special issue is aimed at presenting the most recent advances in LTE technology, including the front-end component design and channel modeling techniques. The collected papers represent the state-of-the-art work being carried out in this topic area.

Reducing the antenna size while maintaining a wide bandwidth and high efficiency is highly demanded but also challenging in the design of LTE antennas. The paper by M. Rafiee et al. presents a planar inverted-F antenna (PIFA) used in LTE band 7. They employed interdigital coupling structure to reduce the antenna size and meanwhile to tune the resonant frequency. An interesting benefit of such antenna is that the working frequency can be easily tuned by changing the interdigital part while being able to maintain the size of the whole antenna if required.

Multiple input multiple output (MIMO) technology provides high channel capacity and high data throughput in LTE and the next generation communication systems. However, the compact arrangement of the antennas without mutual coupling remains the most challenging problem in the design

of MIMO antennas. The paper by Y. Shi et al. proposes a compact MIMO antenna. The zeroth-order modes of the composite right- and left-hand transmission line (CRLH-TL) greatly reduce the size of the antenna. And a pair of L-shaped parasitic strips and an etching slot on the ground are employed to reduce the mutual coupling between two antennas. The paper by I. Tzanidis et al. provides a system level simulation of a 2D active antenna array for FD-MIMO systems. It is found that the proposed antenna array with alternating polarization scheme yields the highest throughput gain. The port virtualization techniques for the antenna array are also discussed in this paper. The paper by H. Shi et al. proposes a direction-of-arrival estimation approach to cope with the scenario where uncorrelated and coherent sources are simultaneously presented in multipath environment. This proposed technique could be potentially applied to MIMO communication.

In addition to antennas, other front-end components, such as filters and power dividers, also exhibit great importance in the efficiency enhancement of LTE communication systems. The paper by W.-Q. Pan et al. presents a dual-band tunable bandpass filter based on a trimode resonator. Another paper by W.-Q. Pan et al. provides a combined solution for power divider and filters, that is, filtering power divider. The integration of filters into other front-end components, for

example, antennas, amplifiers, and power dividers, greatly reduces the size and meanwhile enhances the performance of the whole system. This topic is getting more and more popular nowadays.

Moreover, this collection includes two papers on channel modeling and interference elimination techniques for LTE communications. The paper by J. F. Monserrat et al. presents a map-based realistic channel model for urban macrocell scenarios, exhibiting a tradeoff between realism and implementation complexity. The paper by H. Zheng et al. carries out an interesting study on the interference problem of the LTE system under radar interference circumstance. They apply the principle of cognitive radio to study the interference between the radar and LTE system and subsequently propose a scheme to get rid of the radar interference.

## Acknowledgments

The editors would like to thank all the authors and the anonymous reviewers for their contributions to this special issue.

*Qingfeng Zhang  
Sai Wai Wong  
Cheng Jin  
Xiu Yin Zhang  
Yifan Chen  
Dimitrios Sounas  
Nima Chamanara*

## Research Article

# DOA Estimation for Mixed Uncorrelated and Coherent Sources in Multipath Environment

Heping Shi, Wen Leng, Anguo Wang, and Tongfeng Guo

School of Electronic Information Engineering, Tianjin University, Tianjin 300072, China

Correspondence should be addressed to Heping Shi; shiheping1119@163.com

Received 8 July 2014; Accepted 7 October 2014

Academic Editor: Yifan Chen

Copyright © 2015 Heping Shi et al. This is an open access article distributed under the Creative Commons Attribution License, which permits unrestricted use, distribution, and reproduction in any medium, provided the original work is properly cited.

A novel direction-of-arrival (DOA) estimation method is proposed to cope with the scenario where a number of uncorrelated and coherent narrowband sources simultaneously impinge on the far-field of a uniform linear array (ULA). In the proposed method, the DOAs of uncorrelated sources are firstly estimated by utilizing the property of the moduli of eigenvalues of the DOA matrix. Afterwards, the contributions of uncorrelated sources and the interference of noise are eliminated completely by exploiting the improved spatial differencing technique and only the coherent components remain in the spatial differencing matrix. Finally, the remaining coherent sources can be resolved by performing the improved spatial smoothing scheme on the spatial differencing matrix. The presented method can resolve more number of sources than that of the array elements and distinguish the uncorrelated and coherent sources that come from the same direction as well as improving the estimation performance. Simulation results demonstrate the effectiveness and efficiency of the proposed method.

## 1. Introduction

Direction-of-arrival (DOA) estimation is a major research issue in array signal processing including radar, guidance systems, sonar, seismic exploration, and electronic surveillance [1]. Several high-resolution algorithms, such as multiple signal classification (MUSIC) [2] and estimation of signal parameter via rotation invariance techniques (ESPRIT) [3], have been proposed to resolve the far-field uncorrelated sources. However, highly correlated or coherent source signals are common in multipath propagation environments due to the reflection and refraction of source signals in practical. Based on such scenario, the coherent sources facilitate the rank loss of the covariance matrix, which could result in the failure of the conventional high-resolution estimation algorithms. That is, those high-resolution algorithms may fail in localizing when uncorrelated and coherent source signals coexist.

To solve the aforementioned coherency problem, various effective techniques have been proposed. Some preprocessing techniques referred to as spatial smoothing (SS) have been developed. The SS method divides the total array elements into a few overlapping subarrays and then averages

the subarray output covariance matrices to form the spatially smoothed covariance matrix to decorrelate the coherence between the incoming sources [4, 5]. However, the SS method generally reduces the array aperture. Besides, the number of signals the SS method resolved cannot exceed the number of array sensors. In [6], a JADE approach is presented to estimating the angle-of-arrival and delays of the multipath source signals, which can estimate more parameters than the number of antennas. A DOA estimation technique [7] is proposed to eliminate the possible false DOAs of uncorrelated signals. Unfortunately, this method shows an unsatisfactory estimation performance. The approach based on higher-order cumulants (HOC), such as [8, 9], can estimate the DOAs of coherent source signals. But this method generally requires large number of snapshots and suffers from burdensome computation. The algorithm proposed in [10] decorrelates the coherent sources by reconstructing a Toeplitz matrix and achieves good performance. However, the main disadvantage is that the number of resolved sources is restricted within the number of reduced array sensors no matter whether the sources are coherent or not. In [11], a deflation approach is introduced, but the number of resolvable coherent sources is less than half of the number of array elements. Recently,

a relevance vector machine algorithm [12], based on spatial filtering, is proposed to estimate DOAs of coherent incoming signals. However, it can only deal with coherent sources and the number of sources resolved by this method is less than that of array elements. In order to deal with more sources, a non-Toeplitz matrix is constructed by exploiting the symmetric configuration of uniform linear array (ULA) [13]. However, the computational load is too high for practical application when all of the constructed matrices are utilized, whereas the performance degrades if just one constructed matrix is used. In [14], the contributions of uncorrelated and partially correlated source signals are removed by exploiting the oblique projection (OP algorithm). However, it needs to estimate the DOAs of uncorrelated and coherent sources in sequence. Besides, the estimation performance is unsatisfactory. The approach with fewer sensors is presented in [15]. In this approach, the DOA matrix is directly constructed by performing multiple eigenvalue decomposition (EVD) on the covariance matrix, which could result in a high probability of failure; moreover, the computational complexity is not very attractive. The approach introduced in [16] exploits the property of the moduli of eigenvalues to distinguish uncorrelated sources from coherent sources. However, this approach cannot completely eliminate the cross-term effects and the computational complexity is not very attractive, either. The differencing method is introduced in [17–19]. Based on covariance differencing and iterative spatial smoothing, the method introduced in [17] requires information about the covariance matrix of uncorrelated source signals, which may be difficult in realization. The number of sources resolved by the technique in [18] is less than that of array elements. The method in [19] can resolve more source signals. However, the difference smoothing matrix will lead to rank deficient once the coherent group contains an odd number of source signals. Therefore, it needs extra processing to recover the rank. Furthermore, the performance of the method is just verified by simulation results without any theoretical analysis.

In this paper, a high-resolution DOA estimation method is proposed when uncorrelated and coherent source signals are together. Firstly, the uncorrelated sources are distinguished from coherent sources by using the property of the moduli of eigenvalues. Then based on the improved spatial differencing method, the contributions of uncorrelated source signals and the interference of noise are removed such that only coherent source signals are reserved in the constructed differencing matrix. Finally, by performing the improved SS method on the differencing matrix, whose rank is equal to the number of coherent sources, the coherent sources can be achieved.

The rest of the paper is organized as follows. The signal model is briefly introduced in Section 2. The algorithm of DOA estimation is explained in detail in Section 3. In Section 4, simulation results are presented to validate the effectiveness of the proposed algorithm. Finally, some concluding remarks for the proposed algorithm are provided in Section 5.

Throughout this paper, the following notations are used.  $(\cdot)^T$ ,  $(\cdot)^H$ , and  $(\cdot)^\dagger$  denote the transpose, conjugate transpose, and pseudo inverse of a matrix, respectively. The notation  $|\cdot|$

stands for the moduli of a complex scalar, while  $E[\cdot]$  is the expectation operator. Moreover, the notation  $\text{blkdiag}[\mathbf{R}_1, \mathbf{R}_2]$  represents the block diagonal matrix with diagonal entries  $\mathbf{R}_1$ ,  $\mathbf{R}_2$ . The notation  $\mathbf{L}(a : b, c : d)$  denotes submatrix containing the elements from  $a$ th to  $b$ th rows and  $c$ th to  $d$ th columns of matrix  $\mathbf{L}$ , respectively.

## 2. Signal Model

Consider  $K$  narrowband far-field signals with  $\theta$  impinging on a ULA with  $N$  equispaced sensors, where the distance between adjacent sensors is equal to half the wavelength. Let the first sensor be the reference, and then the steering vector can be given:

$$\mathbf{a}(\theta) = [1, z, \dots, z^{N-1}]^T, \quad z = e^{-j2\pi d/\lambda \sin \theta}, \quad (1)$$

where  $\lambda$  denotes the carrier wavelength of the source signal. Without loss of generality, assume that the first  $K_u$  source signals are uncorrelated, and the source signal that comes from direction  $\theta_k$  corresponds to the propagation of the far-field source signal  $s_k(t)$  with power  $\sigma_k^2$  for  $k = 1, \dots, K_u$ . The remaining are  $L$  groups of  $K_c = K - K_u$  coherent source signals, which come from  $L$  statistically independent far-field source signals  $s_k(t)$  with power  $\sigma_k^2$ , ( $k = K_u + 1, \dots, K_u + L$ ), and with  $P_k$  multipath sources for each source. Furthermore, in the  $k$ th coherent group, the source that comes from direction  $\theta_{kp}$  corresponds to the  $p$ th multipath propagation of source  $s_k(t)$ , for  $k = K_u + 1, \dots, K_u + L$  and  $p = 1, \dots, P_k$ . Assume that the coherent source signals in different groups are uncorrelated with each other and the uncorrelated source signals. The  $N \times 1$  received data vector is given by

$$\begin{aligned} \mathbf{x}(t) &= [x_1(t), \dots, x_N(t)]^T \\ &= \sum_{i=1}^{K_u} \mathbf{a}(\theta_i) \mathbf{s}_i(t) + \sum_{i=K_u+1}^{K_u+L} \sum_{p=1}^{P_i} \mathbf{a}(\theta_{ip}) \gamma_{ip} \mathbf{s}_i(t) + \mathbf{n}(t) \\ &= \mathbf{A}_u \mathbf{s}_u(t) + \mathbf{A}_c \mathbf{s}_c(t) + \mathbf{n}(t) \\ &= \mathbf{A} \mathbf{s}(t) + \mathbf{n}(t) \\ &= \widehat{\mathbf{A}} \Gamma \mathbf{s}(t) + \mathbf{n}(t), \end{aligned} \quad (2)$$

where  $\mathbf{a}(\theta_i) = [1, e^{-j2\pi d/\lambda \sin(\theta_i)}, \dots, e^{-j2\pi(N-1)d/\lambda \sin(\theta_i)}]^T$  is the steering vector.  $\gamma_{ip}$  is the complex fading coefficient of the  $p$ th multipath propagation corresponding to the  $i$ th source signal with  $|\gamma_{ip}| \leq 1$ ,  $\mathbf{y}_i = [\gamma_{i1}, \dots, \gamma_{iP_i}]^T$ . Also  $\mathbf{A} = [\mathbf{A}_u \quad \mathbf{A}_c]$ ,  $\mathbf{A}_u = [\mathbf{a}(\theta_1), \dots, \mathbf{a}(\theta_{K_u})]$ ,  $\mathbf{A}_c = [\mathbf{A}_1 \mathbf{y}_1, \dots, \mathbf{A}_L \mathbf{y}_L]$  with  $\mathbf{A}_i = [\mathbf{a}(\theta_{i1}), \dots, \mathbf{a}(\theta_{iP_i})]$ ,  $\widehat{\mathbf{A}} = [\mathbf{A}_u, \mathbf{A}_{c,K_u+1}, \dots, \mathbf{A}_{c,K_u+L}]$ ,  $\Gamma = \text{blkdiag}[\mathbf{I}_{K_u}, \mathbf{y}_{K_u+1}, \dots, \mathbf{y}_{K_u+L}]$ . Moreover  $\mathbf{s}(t) = [\mathbf{s}_u^T(t) \quad \mathbf{s}_c^T(t)]^T$ ,  $\mathbf{s}_c(t) = [s_{K_u+1}(t), \dots, s_{K_u+L}(t)]^T$ .  $\mathbf{n}(t)$  is the noise vector with the power of each entry being equal to  $\sigma_n^2$ ;  $\mathbf{n}(t) = [n_1(t), \dots, n_N(t)]^T$ . By assumption, the entries of  $\mathbf{s}(t)$  and  $\mathbf{n}(t)$  are zero-mean wide-sense stationary random processes and are uncorrelated to each other.

From (2), the array covariance matrix can be expressed as

$$\begin{aligned}\mathbf{R} &= E[\mathbf{x}(t)\mathbf{x}^H(t)] = \mathbf{A}\mathbf{R}_s\mathbf{A}^H + \sigma_n^2\mathbf{I}_N \\ &= \mathbf{R}_T + \mathbf{R}_{NT} + \sigma_n^2\mathbf{I}_N \\ &= \mathbf{A}_u\mathbf{R}_u\mathbf{A}_u^H + \mathbf{A}_c\mathbf{R}_c\mathbf{A}_c^H + \sigma_n^2\mathbf{I}_N,\end{aligned}\quad (3)$$

where  $\mathbf{R}_s = \text{blkdiag}\{\mathbf{R}_u, \mathbf{R}_c\}$  is block diagonal.  $\mathbf{R}_u = \text{diag}\{\sigma_1^2, \dots, \sigma_{K_u}^2\}$  is the covariance matrix of  $\mathbf{s}_u(t)$ , and  $\mathbf{R}_c = \text{diag}\{\sigma_{K_u+1}^2, \dots, \sigma_{K_u+L}^2\}$  is the covariance matrix of  $\mathbf{s}_c(t)$ .  $\mathbf{I}_N$  denotes the  $N \times N$  identity matrix.

### 3. DOA Estimation of Proposed Method

In this section, the DOA estimation will be carried out by using the proposed method. The processes of the estimation of uncorrelated and coherent sources are described in detail in Sections 3.1 and 3.2, respectively.

**3.1. DOA Estimation of the Uncorrelated Sources.** For the DOA estimation of the uncorrelated source signals, the EVD of  $\mathbf{R}$  can be expressed:

$$\mathbf{R} = \mathbf{U}_s\Lambda_s\mathbf{U}_s^H + \mathbf{U}_n\Lambda_n\mathbf{U}_n^H, \quad (4)$$

where  $\mathbf{U}_s = [\mathbf{u}_1, \dots, \mathbf{u}_{K_u+L}]$ ,  $\Lambda_s = \text{diag}\{\lambda_1, \dots, \lambda_{K_u+L}\}$ ,  $\mathbf{U}_n = [\mathbf{u}_{K_u+L+1}, \dots, \mathbf{u}_N]$ , and  $\Lambda_n = \text{diag}\{\lambda_{K_u+L+1}, \dots, \lambda_N\}$ . The columns of  $\mathbf{U}_s$  span the signal subspace corresponding to the  $K_u + L$  larger eigenvalues and the noise subspace  $\mathbf{U}_n$  is constructed by the eigenvectors corresponding to the  $N - (K_u + L)$  smaller eigenvalues. Furthermore, the  $\mathbf{U}_s$  is also spanned by  $\widehat{\mathbf{A}}\Gamma$ . Therefore

$$\mathbf{U}_s = \widehat{\mathbf{A}}\Gamma\Xi, \quad (5)$$

where  $\Xi$  is a full-rank matrix. The  $\mathbf{U}_s$  can be divided into two partially overlapped subarrays of size  $(N - 1) \times (K_u + L)$ . Then the two output submatrix can be expressed as

$$\begin{aligned}\mathbf{U}_1 &= \mathbf{U}_s(1 : N - 1, :) = \widehat{\mathbf{A}}_1\Gamma\Xi, \\ \mathbf{U}_2 &= \mathbf{U}_s(2 : N, :) = \widehat{\mathbf{A}}_2\Gamma\Xi = \widehat{\mathbf{A}}_1\Psi\Gamma\Xi,\end{aligned}\quad (6)$$

where  $\Psi = \text{diag}(e^{-j2\pi d \sin \theta_1/\lambda}, \dots, e^{-j2\pi d \sin \theta_k/\lambda}, \dots, e^{-j2\pi d \sin \theta_K/\lambda})$ .

Based on the above definition (6), a new matrix  $\mathbf{U}$  can be constructed as follows:

$$\begin{aligned}\mathbf{U} &= \mathbf{U}_1^\dagger\mathbf{U}_2 = \Xi^{-1}\Gamma^\dagger\Psi\Gamma\Xi \\ &= \Xi^{-1}\Delta\Xi \\ &= \Xi^{-1}\text{diag}(\mu_1, \dots, \mu_{K_u}, \mu_{K_u+1}, \dots, \mu_{K_u+L})\Xi,\end{aligned}\quad (7)$$

$$\Gamma^\dagger = \text{blkdiag}[\mathbf{I}_{K_u}, \boldsymbol{\beta}_{K_u+1}, \dots, \boldsymbol{\beta}_{K_u+L}],$$

$$\boldsymbol{\beta}_i = [\beta_{i1}, \dots, \beta_{iP_i}],$$

$$\mu_i = \begin{cases} e^{-j2\pi d \sin \theta_i/\lambda}, & i = 1, \dots, K_u \\ \beta_{i1}e^{-j2\pi d \sin \theta_{i1}/\lambda} + \beta_{i2}\gamma_{i1}e^{-j2\pi d \sin \theta_{i2}/\lambda} + \dots \\ + \beta_{iP_i}\gamma_{i(P_i-1)}e^{-j2\pi d \sin \theta_{iP_i}/\lambda}, & i = K_u + 1, \dots, K_u + L, \end{cases} \quad (8)$$

where  $\theta_i$  ( $i = 1, \dots, K_u$ ) represents the  $i$ th uncorrelated source and  $\theta_{if}$  ( $i = K_u + 1, \dots, K_u + L; f = 1, \dots, P_i$ ) represents the  $f$ th source in the  $i$ th coherent group.

According to mathematics knowledge, one can prove that  $\Delta$  possesses the following important property [16]:

$$\begin{aligned}|\mu_{K_u+L}| &\leq |\mu_{K_u+L-1}| \leq \dots \leq |\mu_{K_u+1}| \\ &< |\mu_{K_u}| = |\mu_{K_u-1}| = |\mu_1| = 1.\end{aligned}\quad (9)$$

Equation (9) implies that, by performing EVD of  $\mathbf{U}$ , the moduli values of the eigenvalues corresponding to the uncorrelated sources are all equal to 1. Meanwhile, the moduli values of the eigenvalues of the remaining coherent sources will not possess the characteristic of uncorrelated sources, whose moduli values are all less than 1. Therefore, we can choose a threshold  $\xi$  in practice to estimate the number of uncorrelated sources:

$$\delta_i = ||\mu_i| - 1|, \quad i = 1, \dots, K_u + L. \quad (10)$$

Substitute the moduli of the eigenvalues  $\mu_i$  ( $i = 1, \dots, K_u + L$ ), which is in descending order, into (10). If the  $\mu_w$  is the first to satisfy  $\delta_w = ||\mu_w| - 1| > \xi$ , then  $w - 1$  is the estimated number of the uncorrelated sources. That is, unlike the conventional approach as in [20], extra process will be avoided in the proposed algorithm to detect the number of sources. Suppose that  $\mu_1, \dots, \mu_{K_u}$  are the eigenvalues corresponding to the uncorrelated sources, and then the DOAs of uncorrelated sources can be obtained by computing

$$\theta_i = \arcsin\left(\frac{\lambda}{-j2\pi d}\text{angle}(\mu_i)\right), \quad i = 1, \dots, K_u. \quad (11)$$

**3.2. DOA Estimation of the Coherent Sources.** In this subsection, the improved spatial differencing technique is performed to resolve the DOAs of the coherent sources. From (4), the  $\hat{\sigma}_n^2$  can be achieved by the mean of the eigenvalues of  $\Lambda_n$ , which is expressed as follows:

$$\hat{\sigma}_n^2 = \frac{1}{N - (K_u + L)} \sum_{i=1}^{N-(K_u+L)} \lambda_i. \quad (12)$$

According to (3) and (12), a new matrix  $\widetilde{\mathbf{R}}$  can be further obtained:

$$\begin{aligned}\widetilde{\mathbf{R}} &= \mathbf{R} - \hat{\sigma}_n^2\mathbf{I}_N \\ &= \mathbf{A}_u\mathbf{R}_u\mathbf{A}_u^H + \mathbf{A}_c\mathbf{R}_c\mathbf{A}_c^H + \Delta_n.\end{aligned}\quad (13)$$

Due to the influence of the finite samples,  $\widetilde{\mathbf{R}}$  still includes the noise residual matrix  $\Delta_n$  in practical application. That is, the noise part cannot be eliminated completely in this step. Fortunately, (3) shows that the covariance matrix can be expressed as the sum of a Toeplitz matrix  $\mathbf{R}_T$  consisting of information on uncorrelated signals, a non-Toeplitz matrix  $\mathbf{R}_{NT}$  containing information on coherent signals, and

the noise covariance matrix. Since any Toeplitz matrix  $\mathbf{Z}$  satisfies the following property:

$$\mathbf{J}\mathbf{Z}^T\mathbf{J} = \mathbf{Z}, \quad (14)$$

where  $\mathbf{J}$  denotes the exchange matrix with ones on its antidiagonal and zeros elsewhere, therefore, this property can be used to cancel out the Toeplitz component and eliminate the residual noise part thoroughly, and then a spatial differencing matrix  $\mathbf{R}_{\text{Diff}}$  is defined as follows:

$$\begin{aligned} \mathbf{R}_{\text{Diff}} &= \widetilde{\mathbf{R}} - \mathbf{J}\widetilde{\mathbf{R}}^T \\ &= \widetilde{\mathbf{R}}_{NT} - \mathbf{J}(\widetilde{\mathbf{R}}_{NT})^T\mathbf{J}. \end{aligned} \quad (15)$$

Equation (15) clearly shows that only the information on coherent sources remains in the spatial differencing matrix  $\mathbf{R}_{\text{Diff}}$ . Then the EVD of the  $\mathbf{R}_{\text{Diff}}$  is achieved as follows:

$$\mathbf{R}_{\text{Diff}} = \mathbf{U}_{\text{Diff}}\Lambda_{\text{Diff}}\mathbf{U}_{\text{Diff}}^H \quad (16)$$

where  $\Lambda_{\text{Diff}} = \text{diag}(\mu_{\text{Diff},1}, -\mu_{\text{Diff},1}, \dots, \mu_{\text{Diff},L}, -\mu_{\text{Diff},L})$  with  $\mu_{\text{Diff},i}$  and  $-\mu_{\text{Diff},i}$  ( $i = 1, \dots, L$ ) corresponding to the positive and negative eigenvalues, respectively. Furthermore, the columns of  $\mathbf{U}_{\text{Diff}} = [u_{\text{Diff},1}, \hat{u}_{\text{Diff},1}, \dots, u_{\text{Diff},L}, \hat{u}_{\text{Diff},L}]$  are the eigenvectors corresponding to the aforementioned nonzero eigenvalues. Then, a new matrix  $\mathbf{H}$  can be formed by taking the absolute values of the eigenvalues in  $\Lambda_{\text{Diff}}$ :

$$\mathbf{H} = \mathbf{U}_{\text{Diff}}|\Lambda_{\text{Diff}}|\mathbf{U}_{\text{Diff}}^H. \quad (17)$$

Afterwards, the SS technique is performed on the new matrix  $\mathbf{H}$ . Here, it is assumed that the number of subarrays is  $D$ , and the size of the subarray is  $M$ . Thus,  $N = M + D - 1$ , and the  $k$ th subarray covariance matrix  $\mathbf{H}_k$  ( $k = 1, \dots, D$ ) is expressed as follows:

$$\mathbf{H}_k = \mathbf{H}(k : k + M - 1, k : k + M - 1). \quad (18)$$

Therefore, the smoothed matrix can be obtained:

$$\mathbf{R}'_S = \frac{1}{D} \sum_{k=1}^D (\mathbf{H}_k + \mathbf{J}\mathbf{H}_k^T\mathbf{J}). \quad (19)$$

Finally, by applying the high-resolution DOA techniques to  $\mathbf{R}'_S$ , the coherent sources can be obtained as long as  $K_c \leq M$  and  $P_{\max} \leq 2D$ .

Till now, under the coexistence of both uncorrelated and coherent source signals, the proposed method with the finite sampling data can be implemented as follows.

*Step 1.* Collect data and estimate the covariance matrix  $\mathbf{R}$  by (3).

*Step 2.* Obtain the signal subspace  $\mathbf{U}_s$  by performing the EVD of the matrix  $\mathbf{R}$ , and calculate  $\mathbf{U}_1$  and  $\mathbf{U}_2$  according to (6), respectively.

*Step 3.* Estimate the number of the uncorrelated sources by making full use of  $\xi$  as in (10), and obtain the DOAs of uncorrelated sources based on (11).

*Step 4.* Calculate the spatial differencing matrix  $\mathbf{R}_{\text{Diff}}$  as in (16), and construct the new matrix  $\mathbf{H}$  as in (17).

*Step 5.* Perform SS technique on  $\mathbf{H}$  to obtain the smoothed matrix  $\mathbf{R}'_S$  by (19).

*Step 6.* Estimate the DOAs of coherent sources by making use of high-resolution DOA methods on  $\mathbf{R}'_S$ .

**3.3. Discussion.** In this subsection, the advantages of the proposed method are discussed. In the proposed method, the uncorrelated and coherent source signals are estimated separately. That is, when an uncorrelated source signal comes from the same direction as a coherent source signal does, the presented method can still distinguish them. Furthermore, the proposed method is still valid when the maximal number of the incident source signals is greater than that of the array elements, which can be considered as another advantage. From the aforementioned analysis, the proposed method can resolve, at most,  $K_u + L + 1$  uncorrelated source signals, and the maximal number of incident coherent source signals is equal to  $[P_{\max}/2] + K_c$ , where  $[\tau]$  denotes the minimal integer no less than  $\tau$ . Thus, to resolve all the incoming source signals, the proposed method requires no less than maximum  $[(P_{\max}/2) + K_c, K_u + L + 1]$  array elements, while the FBSS in [5] requires  $K_u + 3/2K_c$ . It is noteworthy that the proposed method can largely reduce the required elements compared with the FBSS method.

The proposed method can suppress the effects of the uncorrelated sources and the additive Gaussian noise effectively based on the fact that the uncorrelated sources and the noise can be eliminated completely. Therefore, it can yield better DOA estimation than the compared methods in [5, 14]. To sum up, the proposed method offers three main advantages: resolving more sources, achieving better DOA estimation, and less restricting Gaussian noise fields.

## 4. Simulation Results

In this section, simulation results are presented to illustrate the validity of the proposed method. The array is an eight-element ULA with half wavelength interspacing. For simplicity, assume that all source signals are of equal power  $\sigma_s^2$ . The SNR and threshold  $\xi$  are set to  $10 \log(\sigma_s^2/\sigma_n^2)$  and 0.015, respectively. When using (11) and (19) to estimate the uncorrelated and coherent sources, respectively, the search range is performed over  $-90^\circ$  to  $90^\circ$  with the scanning interval  $0.1^\circ$ . All the simulation experiments are based on 200 Monte Carlo trials. Two performance indices, called the root-mean-square error (RMSE) and normalized probability of success (NPS), are defined to evaluate the performance of the proposed method:

$$\text{RMSE} = \sqrt{\frac{1}{200K} \sum_{i=1}^{200} \sum_{n=1}^K (\hat{\theta}_n(i) - \theta_n)^2}, \quad (20)$$

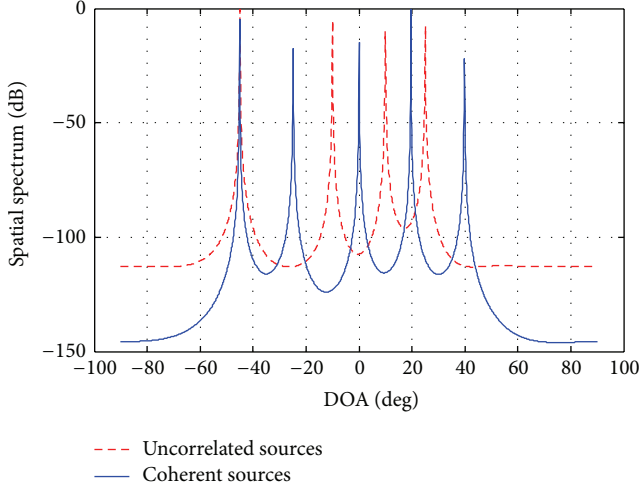


FIGURE 1: Spatial spectrum for uncorrelated (dotted line) and coherent (solid line) signals.

where  $\hat{\theta}_n(i)$  is the estimate of  $\theta_n$  for the  $i$ th Monte Carlo trial and  $K$  is the number of all the uncorrelated or all the coherent sources:

$$\text{NPS} = \frac{Y_{\text{suc}}}{T_{\text{total}}}, \quad (21)$$

where  $Y_{\text{suc}}$  and  $T_{\text{total}}$  denote the times of success and Monte Carlo trial, respectively. Furthermore, a successful experiment is the one satisfying  $\max(|\hat{\theta}_n - \theta_n|) < \varepsilon$ . Where  $\varepsilon$  equals 0.5 and 1.5 for estimation of uncorrelated and coherent sources, respectively.

In the first simulation, we consider the scenario in which the number of incident sources goes beyond the number of array sensors. Consider four uncorrelated sources coming from  $[-45^\circ, -10^\circ, 10^\circ, 25^\circ]$  and two groups of five coherent sources coming from  $[-45^\circ, -25^\circ, 0^\circ]$  and  $[20^\circ, 40^\circ]$ , respectively, when  $N = 8$ . Note that one of uncorrelated sources, namely,  $\theta = -45^\circ$ , has the same DOA with one of the first group of coherent sources. The fading coefficients of the two groups of coherent sources are  $[1, 0.93, 0.89]$  and  $[1, 0.9]$ , respectively. The number of snapshots is 1000, and the input SNR is 10 dB. The spatial spectrums of the uncorrelated and coherent source signals by the proposed method are shown in Figure 1. It can be seen that the sharp peaks are detected at the correct DOAs. Moreover, the uncorrelated source from  $-45^\circ$  and the coherent source from  $-45^\circ$  both can be detected due to the fact that the DOAs of uncorrelated sources and coherent sources are estimated in two stages. This is consistent with the theoretical analysis aforementioned.

The second simulation considers three uncorrelated source signals from  $[-45^\circ, 15^\circ, 30^\circ]$  and two groups of four coherent source signals from  $[-30^\circ, 11^\circ]$  and  $[45^\circ, 60^\circ]$ , respectively, when  $N = 8$ . The fading coefficients of the two groups of coherent sources are  $[1, 0.9]$  and  $[1, 0.85]$ , respectively. The number of snapshots is set to 1000. The RMSE of the DOAs versus input SNR is shown in Figure 2. Figure 2 illustrates that the RMSE of both uncorrelated and

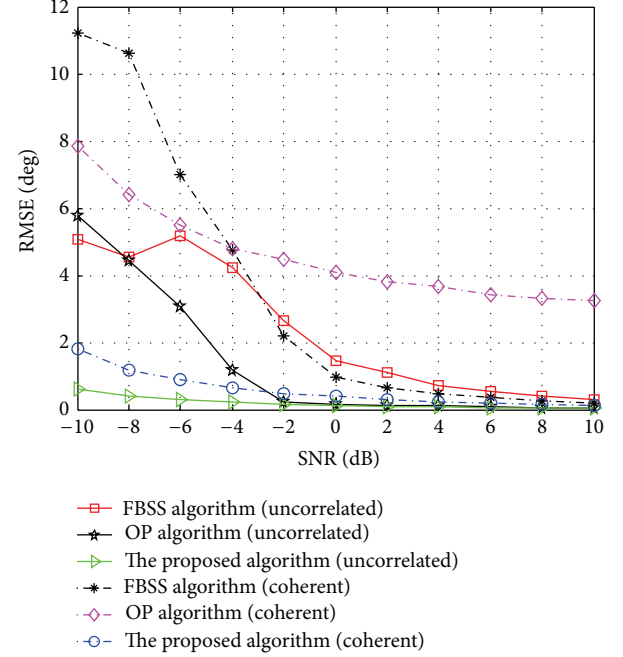


FIGURE 2: RMSE of the DOA estimates versus input SNR for the uncorrelated and coherent signals.

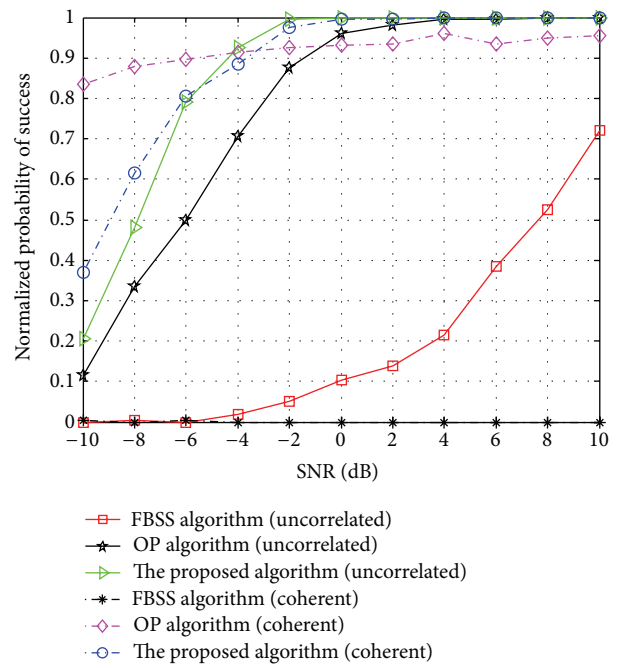


FIGURE 3: NPS of the DOA estimates versus input SNR for the uncorrelated and coherent signals.

coherent sources of the proposed method is more accurate than that of algorithms in [5] (FBSS) and [14] (OP), especially at low SNR. Figure 3 shows the NPS of the DOAs versus SNR, which illustrates that the performance of the proposed method is better than that of FBSS and OP algorithms as the SNR increases. The reason is that the proposed algorithm

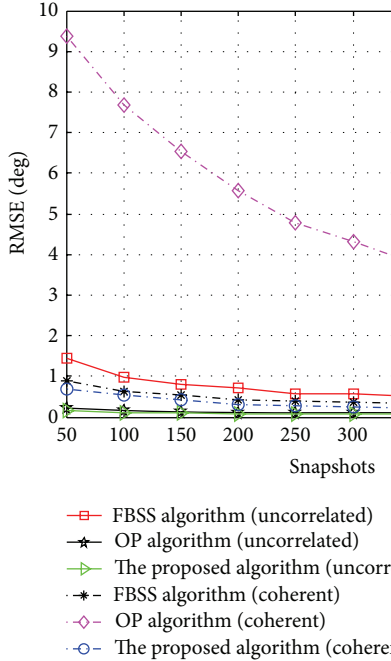


FIGURE 4: RMSE of the DOA estimates versus input snapshots for the uncorrelated and coherent signals.

utilizes the whole ULA to estimate the uncorrelated source signals, and then the interference of Gaussian noise and the contributions of uncorrelated source signals can be fully eliminated in a subsequent stage through the improved differencing processing. On the contrary, based on the reduced array, the FBSS obtains the DOAs of uncorrelated and coherent sources simultaneously. Besides, no power or information is lost for coherent source signals in the proposed method, which is the opposite in OP algorithm.

The third simulation considers the same scenario as the second one at different number of snapshots. When the SNR is 5 dB, the RMSE of the uncorrelated and coherent source signals against number of snapshots is shown in Figure 4. It can be seen from Figure 4 that the proposed method achieves higher estimation accuracy than FBSS and OP algorithms as the number of snapshots increases. The reason is that (11) (estimating the uncorrelated source signals) and (19) (estimating the coherent source signals) are closer to their true value as the number of snapshots increases. Furthermore, no matter how large the number of the snapshots is, the proposed algorithm always has higher estimation performance than FBSS and OP algorithms.

In addition, the NPS of the uncorrelated and coherent sources against number of snapshots is shown in Figure 5 when the SNR is 10 dB. From Figure 5, we can see that the performance of uncorrelated sources by the proposed algorithm is superior to the compared methods as the number of snapshots is varied from 50 to 250. That is, in small number of snapshots, the superiority of the proposed algorithm is more pronounced. This indicates that the proposed algorithm will be more useful when the low-computational cost and highly real-time data process are required. Meanwhile, Figure 5 also shows that the performance of coherent sources by

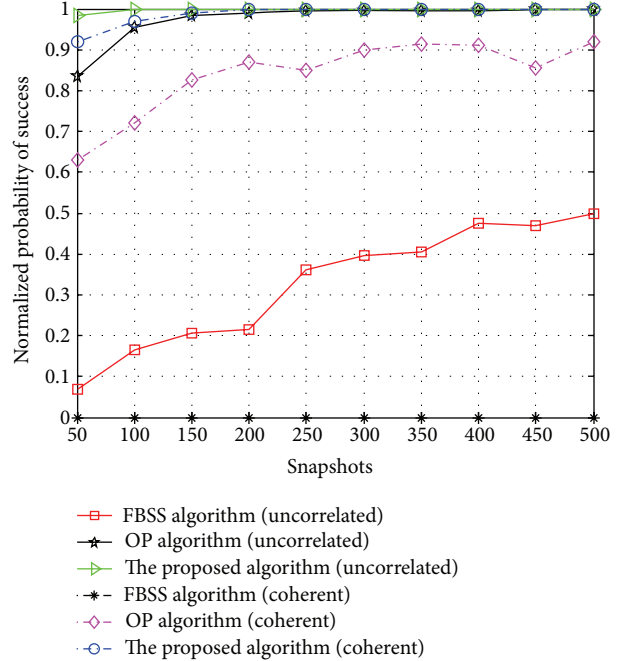


FIGURE 5: NPS of the DOA estimates versus input snapshots for the uncorrelated and coherent signals.

the proposed algorithm outperforms the OP algorithm when the number of snapshots changes. Moreover, the NPS of the proposed algorithm becomes stabilized as the number of snapshots is over 150, while the FBSS will fail in this scenario.

The last simulation studies not only the scenario where the uncorrelated, partially correlated, and coherent sources coexist, but also the situation in which the total number of incoming signals exceeds that of array sensors. The number of snapshots is 1000. Four uncorrelated sources from  $[-45^\circ, -10^\circ, 10^\circ, 25^\circ]$ , two partially correlated sources from  $[40^\circ, 60^\circ]$ , and a group of three coherent sources from  $[-45^\circ, -30^\circ, 11^\circ]$  are considered when  $N = 8$ . The fading coefficients of the coherent sources are  $[1, 0.95, 0.85]$ , and the correlation coefficient between the two partially correlated sources is selected to be  $\rho = 0.7$ . The DOAs of partially correlated sources are estimated by the method in Section 3.2, and the definition of a successful experiment of the partially correlated sources is consistent with that of the coherent sources. The performance curves of the DOAs versus input SNR are shown in Figures 6 and 7. Both figures indicate that the proposed algorithm can still achieve good estimation performance when the uncorrelated, partially correlated, and coherent sources coexist.

Similar to the above simulation, the SNR is set to be 5 dB, and the number of snapshots is varied from 300 to 800. The performance curves of the DOA estimates against snapshots are shown in Figures 8 and 9. Apparently, as shown in Figures 6 and 7, the same conclusions can be drawn. Figures 8 and 9 indicate that the performance of the DOA estimation by the proposed method will be improved as the number of snapshots increases. In addition, all the performance curves will become stabilized as the number of snapshots increases.

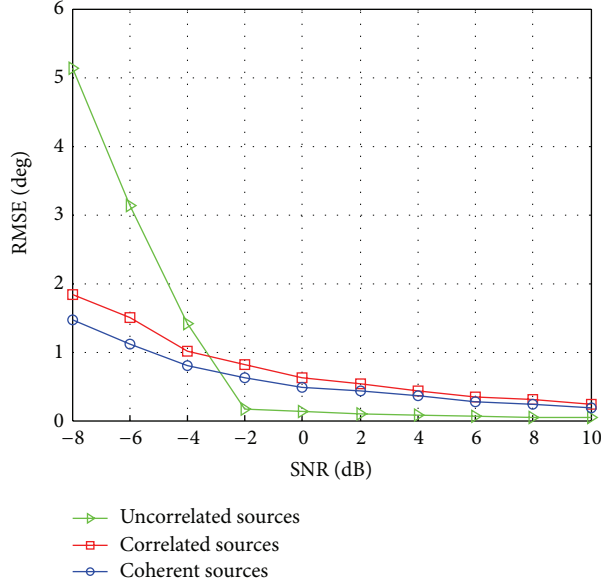


FIGURE 6: RMSE of the proposed method versus input SNR for the uncorrelated, correlated, and coherent signals.

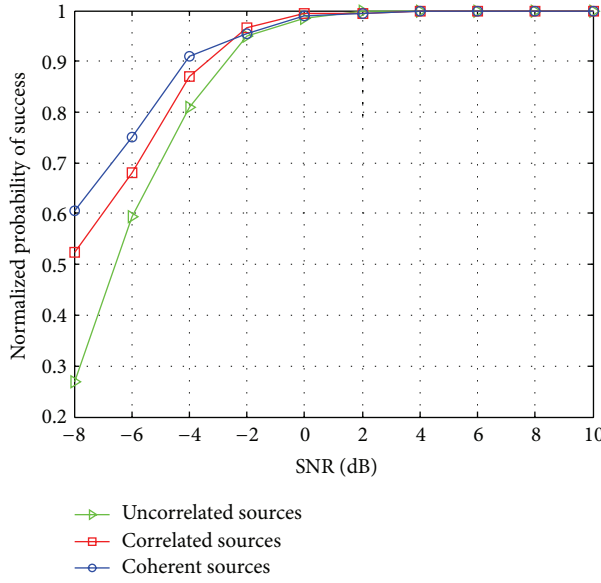


FIGURE 7: NPS of the proposed method versus input SNR for the uncorrelated, correlated, and coherent signals.

## 5. Conclusions

In this paper, a novel method for DOA estimation is proposed when both uncorrelated and coherent sources coexist. In the proposed method, the uncorrelated sources are estimated by using the moduli of eigenvalues, and then the coherent sources are resolved by the improved spatial differencing smoothing method. The proposed method can resolve greater number of sources than that of array sensors as well as improving estimation performance especially when the SNR is low and the number of snapshots is small. Simulation

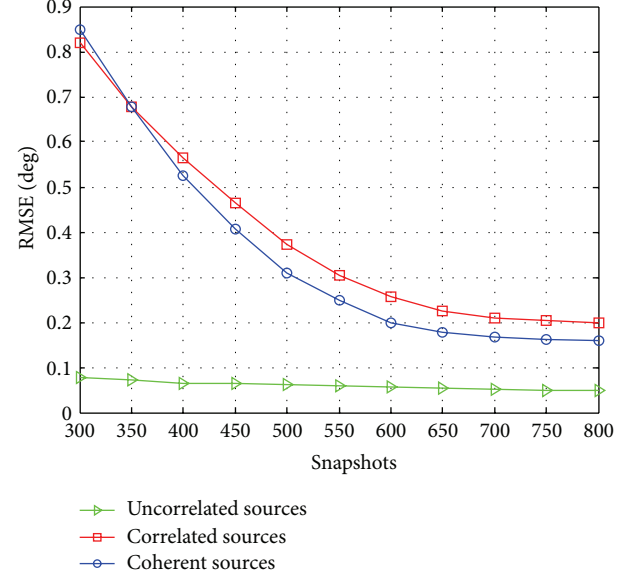


FIGURE 8: RMSE of the proposed method versus input snapshots for the uncorrelated, correlated, and coherent signals.

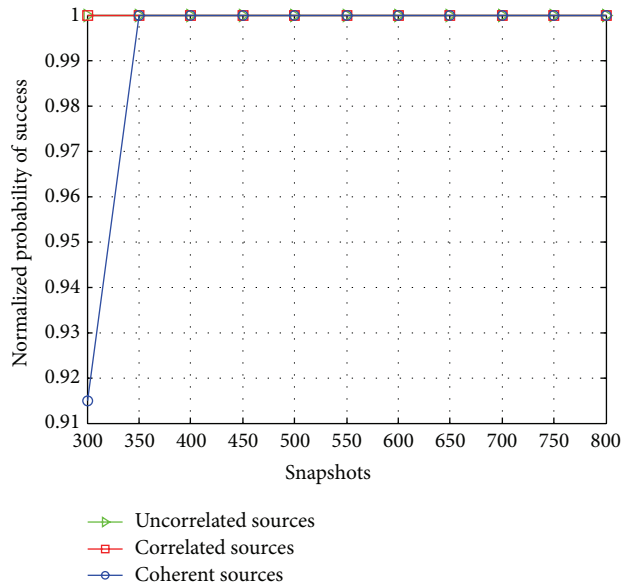


FIGURE 9: NPS of the proposed method versus input snapshots for the uncorrelated, correlated, and coherent signals.

results validate the effectiveness of the proposed method. Moreover, the presented method can also be extended to the scenario where uncorrelated, partially correlated, and coherent sources are mixed.

## Conflict of Interests

The authors declare that there is no conflict of interests regarding the publication of this paper.

## Acknowledgments

This work was supported partially by the National Natural Science Foundation of China (no. 61002010) and the project of the State Key Laboratory of Millimeter Waves (no. K201314).

## References

- [1] H. Krim and M. Viberg, "Two decades of array signal processing research: the parametric approach," *IEEE Signal Processing Magazine*, vol. 13, no. 4, pp. 67–94, 1996.
- [2] R. O. Schmidt, "Multiple emitter location and signal parameter estimation," *IEEE Transactions on Antennas and Propagation*, vol. 34, no. 3, pp. 276–280, 1986.
- [3] R. Roy and T. Kailath, "ESPRIT-estimation of signal parameters via rotational invariance techniques," *IEEE Transactions on Acoustics, Speech and Signal Processing*, vol. 37, no. 7, pp. 984–995, 1989.
- [4] B. Cai, Y. M. Li, and H. Y. Wang, "Forward/backward spatial reconstruction method for directions of arrival estimation of uncorrelated and coherent signals," *IET Microwaves, Antennas and Propagation*, vol. 6, no. 13, pp. 1498–1505, 2012.
- [5] S. U. Pillai and B. H. Kwon, "Forward/backward spatial smoothing techniques for coherent signal identification," *IEEE Transactions on Acoustics, Speech, and Signal Processing*, vol. 37, no. 1, pp. 8–15, 1989.
- [6] M. C. Vanderveen, C. B. Papadias, and A. Paulraj, "Joint angle and delay estimation (JADE) for multipath signals arriving at an antenna array," *IEEE Communications Letters*, vol. 1, no. 1, pp. 12–14, 1997.
- [7] Y. F. Zhang and Z. F. Ye, "Efficient method of DOA estimation for uncorrected and coherent signals," *IEEE Antennas and Wireless Propagation Letters*, vol. 7, pp. 799–802, 2008.
- [8] H. Chen, C. Hou, Q. Wang, L. Huang, and W. Yan, "Cumulants-based Toeplitz matrices reconstruction method for 2-D coherent DOA estimation," *IEEE Sensors Journal*, vol. 14, no. 8, pp. 2824–2832, 2014.
- [9] Z. Ye and Y. Zhang, "DOA estimation for non-Gaussian signals using fourth-order cumulants," *IET Microwaves, Antennas and Propagation*, vol. 3, no. 7, pp. 1069–1078, 2009.
- [10] F.-M. Han and X.-D. Zhang, "An ESPRIT-like algorithm for coherent DOA estimation," *IEEE Antennas and Wireless Propagation Letters*, vol. 4, no. 1, pp. 443–446, 2005.
- [11] X. Xu, Z. Ye, Y. Zhang, and C. Chang, "A deflation approach to direction of arrival estimation for symmetric uniform linear array," *IEEE Antennas and Wireless Propagation Letters*, vol. 5, no. 1, pp. 486–489, 2006.
- [12] Z.-M. Liu, D.-W. Feng, and Z.-T. Huang, "Direction-of-arrival estimation for coherent sources via sparse bayesian learning," *International Journal of Antennas and Propagation*, vol. 2014, Article ID 959386, 8 pages, 2014.
- [13] Z. Ye and X. Xu, "DOA estimation by exploiting the symmetric configuration of uniform linear array," *IEEE Transactions on Antennas and Propagation*, vol. 55, no. 12, pp. 3716–3720, 2007.
- [14] X. Xu, Z. Ye, and J. Peng, "Method of direction-of-arrival estimation for uncorrelated, partially correlated and coherent sources," *IET Microwaves, Antennas and Propagation*, vol. 1, no. 4, pp. 949–954, 2007.
- [15] Z. Ye, Y. Zhang, and C. Liu, "Direction-of-arrival estimation for uncorrelated and coherent signals with fewer sensors," *IET* *Microwaves, Antennas and Propagation*, vol. 3, no. 3, pp. 473–482, 2009.
- [16] L. Gan and X. Luo, "Direction-of-arrival estimation for uncorrelated and coherent signals in the presence of multipath propagation," *IET Microwaves, Antennas and Propagation*, vol. 7, no. 9, pp. 746–753, 2013.
- [17] E. M. Al-Ardi, R. M. Shubair, and M. E. Al-Mualla, "Computationally efficient high-resolution DOA estimation in multipath environment," *Electronics Letters*, vol. 40, no. 14, pp. 908–910, 2004.
- [18] G. Wang, J. Xin, C. Ge, N. Zheng, and A. Sano, "Direction estimation of uncorrelated and coherent narrowband signals with uniform linear array," in *Proceedings of the 1st International Symposium on Access Spaces (ISAS '11)*, pp. 101–104, Yokohama, Japan, June 2011.
- [19] C. Qi, Y. Wang, Y. Zhang, and Y. Han, "Spatial difference smoothing for DOA estimation of coherent signals," *IEEE Signal Processing Letters*, vol. 12, no. 11, pp. 800–802, 2005.
- [20] M. Wax and T. Kailath, "Detection of signals by information theoretic criteria," *IEEE Transactions on Acoustics, Speech, and Signal Processing*, vol. 33, no. 2, pp. 387–392, 1985.

## Research Article

# Compact Unequal Power Divider with Filtering Response

Wei-Qiang Pan,<sup>1</sup> Jin-Xu Xu,<sup>2</sup> Kai Xu Wang,<sup>2</sup> and Xiao Lan Zhao<sup>2</sup>

<sup>1</sup>Information Network Engineering Research Center, South China University of Technology, Guangzhou 510640, China

<sup>2</sup>School of Electronic and Information Engineering, South China University of Technology, Guangzhou 510640, China

Correspondence should be addressed to Jin-Xu Xu; [xjinxu@126.com](mailto:xjinxu@126.com)

Received 16 November 2014; Accepted 30 December 2014

Academic Editor: Nima Chamanara

Copyright © 2015 Wei-Qiang Pan et al. This is an open access article distributed under the Creative Commons Attribution License, which permits unrestricted use, distribution, and reproduction in any medium, provided the original work is properly cited.

We present a novel unequal power divider with bandpass responses. The proposed power divider consists of five resonators and a resistor. The power division ratio is controlled by altering the coupling strength among the resonators. The output ports have the characteristic impedance of  $50\ \Omega$  and impedance transformers in classical Wilkinson power dividers are not required in this design. Use of resonators enables the filtering function of the power divider. Two transmission zeros are generated near the passband edges, resulting in quasielliptic bandpass responses. For validation, a 2:1 filtering power divider is implemented. The fabricated circuit size is  $0.22\ \lambda_g \times 0.08\ \lambda_g$ , featuring compact size for unequal filtering power dividers, which is suitable for the feeding networks of antenna arrays.

## 1. Introduction

Power dividers are widely used in radio frequency (RF) front-ends, such as in power combining networks and antenna arrays [1, 2]. The power ratio of the conventional Wilkinson power divider is controlled by adjusting the characteristic impedance of the branch lines. Impedance transformers are required at the two output ports in unequal power divider designs [3]. Based on the schematic of the classical Wilkinson power divider shown in Figure 1, lots of power dividers have been designed in recent years, including the high power division ratio dividers [4], the arbitrary power division ratio ones [5], out-of-phase ones [6], dual-band ones [7, 8], and spurious-suppressed ones [9, 10].

Apart from power dividers, bandpass filters (BPFs) are also essential parts in many RF front-ends. The two kinds of passive components consume a large area. To reduce the size, they can be integrated [11–18]. In [11, 12], the quarter-wavelength transformers in Wilkinson power dividers are replaced by BPFs. This method can also be used to design unequal power dividers [13]. The filtering circuits can also be used to replace the impedance transformers at the output ports of unequal power dividers, resulting in dual functions [14]. However, the circuit size of the above two unequal

designs needs to be reduced. For miniaturization, the filtering and power splitting circuits can be highly integrated together [15–18]. However, this method has not been applied to unequal filtering power divider designs.

In this paper, a novel unequal power divider with filtering responses is proposed. The circuit consists of a half-wavelength resonator and four quarter-wavelength resonators as well as an isolation resistor. By adjusting the coupling strength among the resonators, unequal power division ratios can be obtained. All the ports have the impedance of  $50\ \Omega$  and the impedance transformers are not required at the output ports. The quasielliptic bandpass responses are obtained by using cross coupling. Based on the proposed idea, an example circuit is designed with the compact size of  $0.22\ \lambda_g \times 0.08\ \lambda_g$ , where  $\lambda_g$  is the guided wavelength at the operating frequency. Good power division and bandpass responses are observed in the experiment.

## 2. Analysis and Design of the Proposed Filtering Unequal Power Divider

Figure 2 shows the schematic diagram of the proposed filtering power divider with the port impedance of  $50\ \Omega$ . The

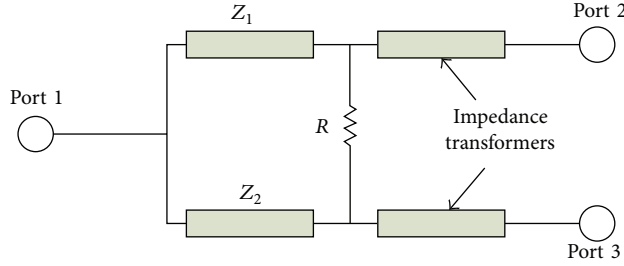


FIGURE 1: Schematic of the classical Wilkinson power divider.

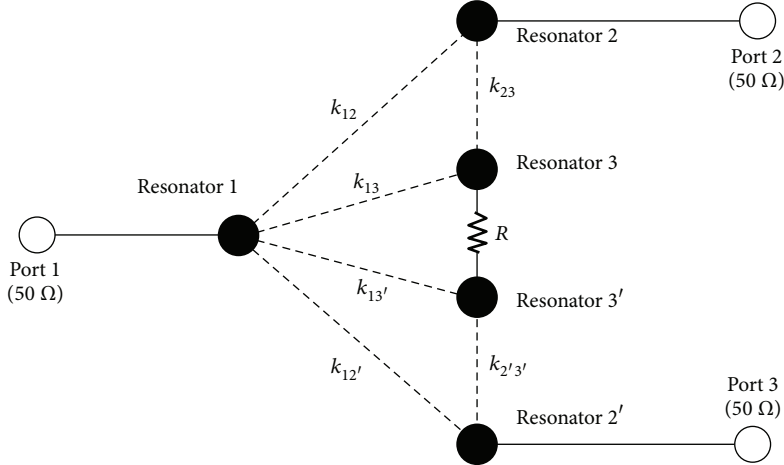


FIGURE 2: The schematic diagram of the proposed filtering power divider.

circuit consists of five resonators and a resistor. Ports 1, 2, and 3 are connected to resonators 1, 2, and 2'. Resonators 2 and 3, 2' and 3' are coupled to resonator 1. This is the same as the equal filtering power divider design in [17]. However, the coupling strengths are different in this design to obtain an unequal power ratio. If the coupling strength among resonator 1 and resonators 2 and 3 is different from that among resonator 1 and resonators 2' and 3', the power injected to resonator 1 will be unequally split. Thus, the unequal power division ratio can be realized by altering the coupling strength, which is different from classical unequal Wilkinson power dividers as shown in Figure 1. Moreover, the port impedance is  $50 \Omega$  and the impedance transformers at the output ports in Figure 1 are not required, resulting in compact size. In order to realize good matching and high isolation between ports 2 and 3, a resistor is added between resonators 3 and 3'.

The circuit can be analyzed by the even-odd-mode method. When even-mode excitation is applied at ports 2 and 3, the voltages at both sides of isolation resistor are equal to ensure that there is no current flowing through the isolation resistor. Thus, the resistor can be eliminated, resulting in the circuit shown in Figure 3(a). For odd-mode excitation, opposite polarity voltages are applied to ports 2 and 3. Then the overall structure can be divided into simple circuits as shown in Figures 3(b) and 3(c). However, due to the existence of the coupling in the circuit, it is difficult

to calculate the resistance. Herein, we use the simulation to choose the resistance for good matching and high isolation between ports 2 and 3. As shown in Figure 4, various kinds of resistance result in different matching status at ports 2 and 3 as well as different isolation effect between ports 2 and 3. Taking into account the port matching and isolation, the resistance is chosen as  $6.8 \text{ k}\Omega$ .

As for the filtering responses, resonators 1, 2, and 3 as well as resonators 1, 2', and 3' form two filtering networks and thus bandpass responses can be realized, which is similar to the design in [17]. Figure 5(a) shows the filtering network between port 1 and port 2 (or port 3). It consists of three resonators. The solid and dash lines denote the electrical and magnetic couplings, respectively. Figure 5(b) shows the bandpass response of the filtering network. Two transmission zeros are generated at both sides of the passband by crossing coupling, resulting in high selectivity.

Based on the above schematic, a filtering power divider is designed with the 2:1 power ratio. Figure 6 shows the microstrip configuration of the proposed circuit. Resonator 1 is a half-wavelength one and the others are quarter-wavelength ones. To realize the required unequal power ratio and obtain good filtering performance, the coupling strengths among the resonators are determined as follows:  $k_{12} = 0.08$ ,  $k_{13} = 0.31$ ,  $k_{23} = 0.1$ ,  $k_{12'} = 0.01$ ,  $k_{13'} = 0.2$ , and  $k_{2'3'} = 0.04$ . The coupling strengths among resonator 1 and resonators 2 and 3 are stronger than the corresponding ones among

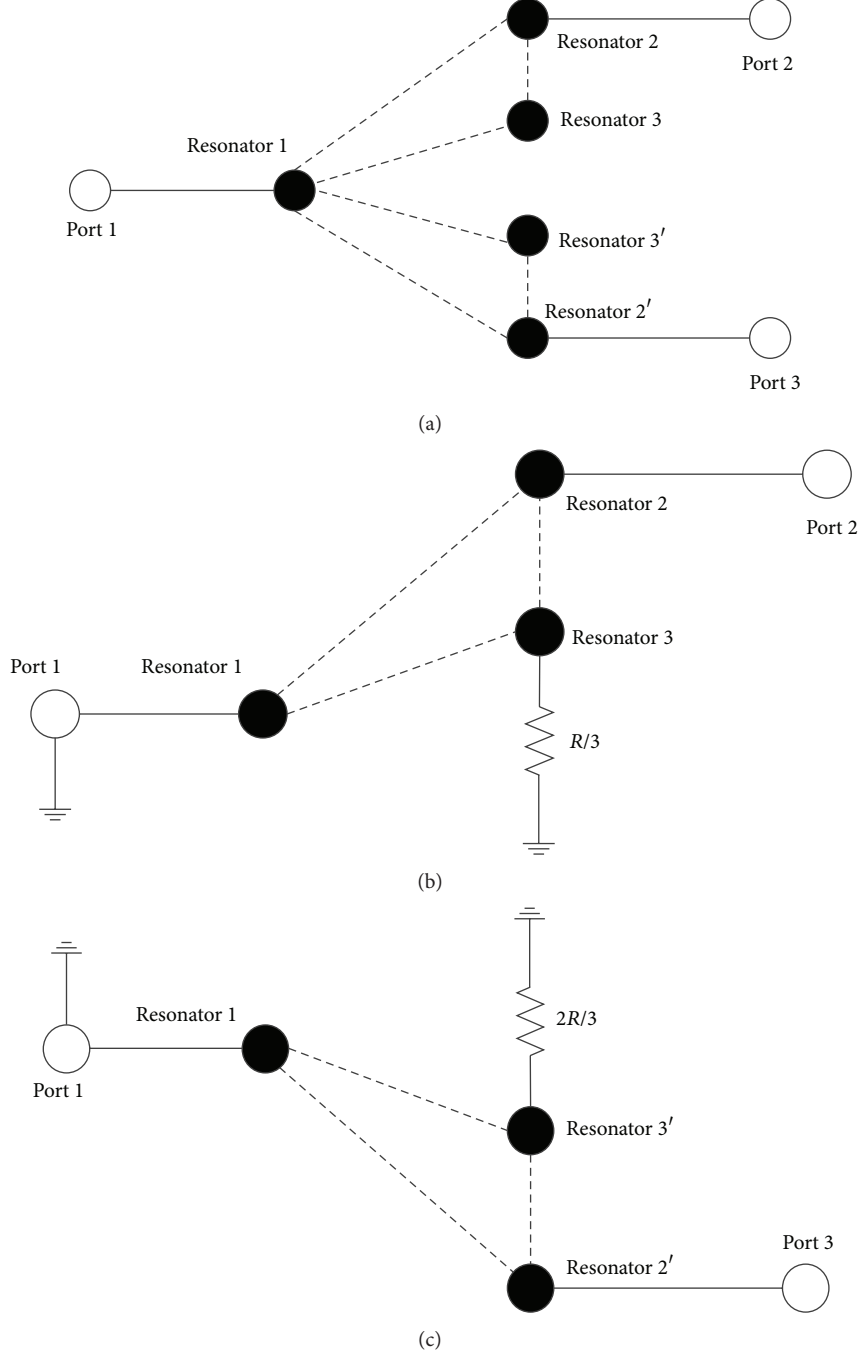


FIGURE 3: (a) The schematic diagram of the even-mode circuit; (b), (c) the schematic diagram of the odd-mode circuit.

resonators 1, 2', and 3'. Thus more power is coupled to port 2, resulting in the 2:1 power division ratio.

The proposed filtering unequal power divider can be designed as follows. Firstly, the desired passband frequency can be obtained by controlling the length of the resonators to be half or quarter guided wavelength. Secondly, the resonators are combined using the configuration in Figure 3 and the coupling strengths are tuned to realize the power ratio and bandpass responses. The third step is to adjust the resistance to obtain the good isolation and port matching.

### 3. Experiment

For demonstration, a 2:1 filtering power divider is implemented. The substrate used in this design has a relative dielectric constant of 3.38, a thickness of 0.81 mm, and a loss tangent of 0.0027. The dimensions are chosen as follows:  $W = 0.5$  mm,  $L_1 = 7$  mm,  $L_2 = 3.5$  mm,  $L_3 = 3.5$  mm,  $L_4 = 18.7$  mm,  $L_5 = 9$  mm,  $L_6 = 3.9$  mm,  $L_7 = 0.8$  mm,  $L_8 = 23.3$  mm,  $L_9 = 0.8$  mm,  $L_{10} = 8.2$  mm,  $L_{11} = 20.3$  mm,  $L_{12} = 3.3$  mm,  $L_{13} = 7.8$  mm,  $L_{14} = 0.7$  mm,  $L_{15} = 1.9$  mm,  $L_{16} = 12.9$  mm,  $L_{17} =$

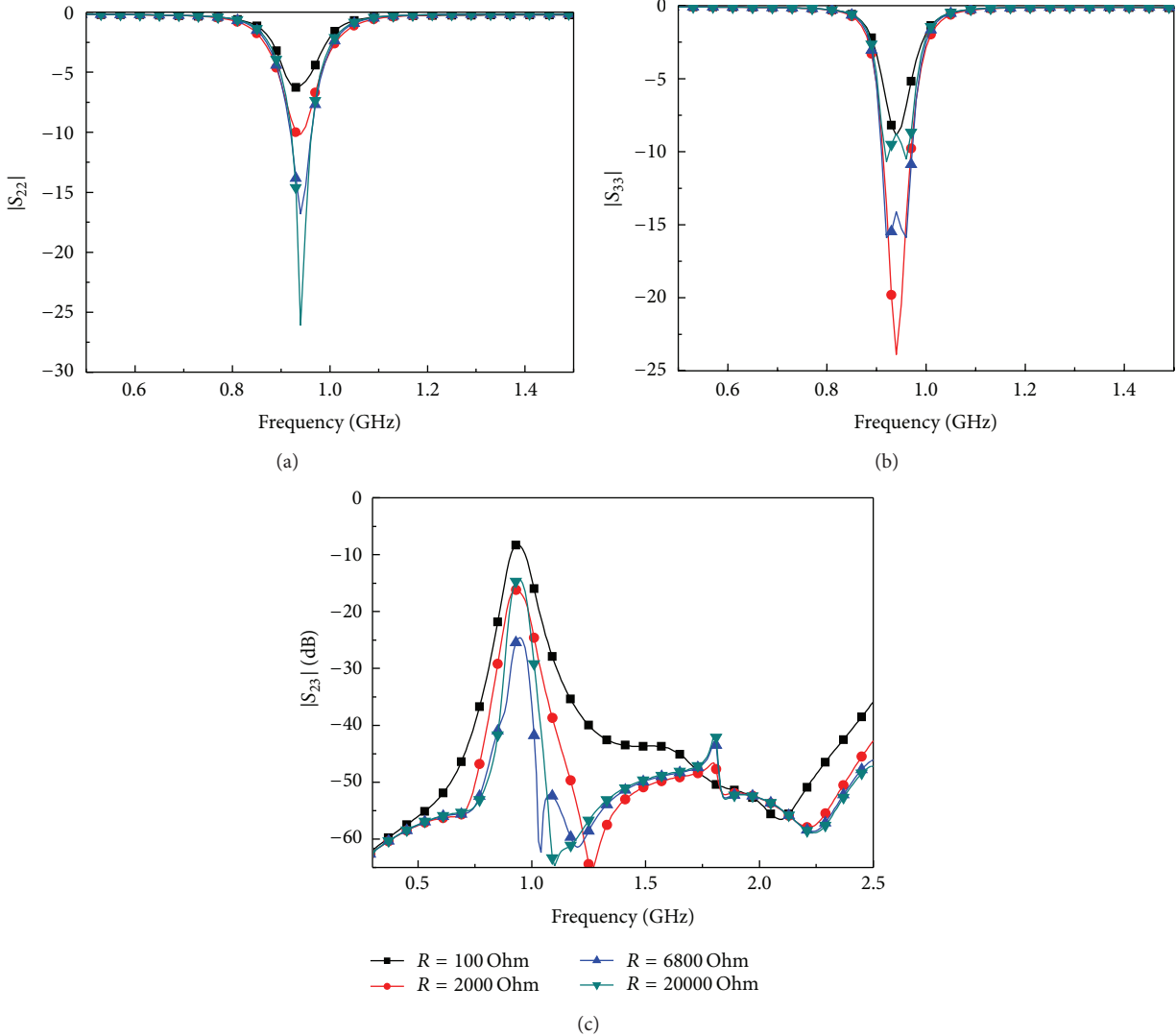


FIGURE 4: Various values of the isolation resistance for (a)  $S_{22}$ , (b)  $S_{33}$ , and (c)  $S_{23}$ .

1.7 mm,  $L_{18} = 20.9$  mm,  $L_{19} = 4.8$  mm,  $L_{20} = 1.8$  mm,  $L_{21} = 4$  mm,  $L_{22} = 25.3$  mm,  $L_{23} = 7.4$  mm,  $L_{24} = 2.7$  mm,  $L_{25} = 27.3$  mm,  $L_{26} = 4.9$  mm,  $g_1 = 0.15$  mm,  $g_2 = 0.15$  mm,  $g_3 = 0.3$  mm,  $g_4 = 0.25$  mm, and  $R = 6.8$  k $\Omega$ . The overall size of the fabricated filter is 44.1 mm  $\times$  17.2 mm (or  $0.22 \lambda_g \times 0.08 \lambda_g$ ). The photograph of the fabricated filter is shown in Figure 7.

The simulation is carried out using IE3D and the results are measured on the network analyzer Agilent E5071C. As shown in Figure 8, the measured center frequency  $f_0$  is 920 MHz, with the fractional bandwidth of 6.5%. The measured  $S_{21}$  and  $S_{31}$  are  $-2.76$  dB and  $-5.78$  dB, respectively. Since the ideal  $S_{21}$  and  $S_{31}$  are  $-1.7$  dB and  $-4.7$  dB for 2:1 unequal power divider, it indicates that the proposed design obtains 2:1 power ratio with the insertion loss of 1.1 dB and magnitude imbalance of less than 0.1 dB. It is noted that both the filtering and power division functions are integrated and the loss can be considered low. The passband return loss of  $S_{11}$ ,  $S_{22}$ , and  $S_{33}$  is greater than 20 dB. The isolation is higher than 17 dB from DC to  $2.6f_0$ . Two transmission zeros are

generated at 0.75 GHz and 1.2 GHz, resulting in quasielliptic bandpass responses. The comparison with other works is tabulated in Table 1. It is seen that the proposed circuit has a small size and a relative high isolation in a wide frequency range up to  $2f_0$ .

#### **4. Conclusion**

This paper has presented a compact unequal power divider with quasielliptic bandpass responses. A new method has been proposed to design the unequal power dividers by altering the coupling strength among the resonators. No impedance transformer is required at the two output ports. The design methodology and experimental results have been presented. Good performance has been obtained together with the compactness. The unequal filtering power division responses and compact circuit size make the proposed circuit useful for feeding networks of antenna arrays.

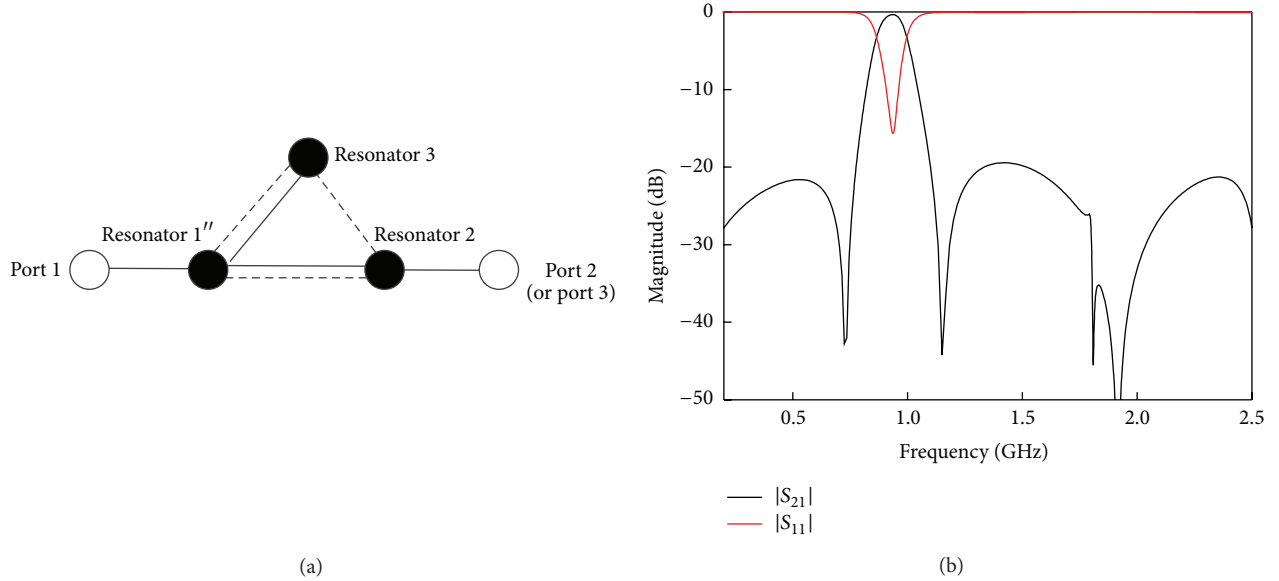


FIGURE 5: (a) The filter network between port 1 and port 2 (or port 3); (b) bandpass response of the filtering network.

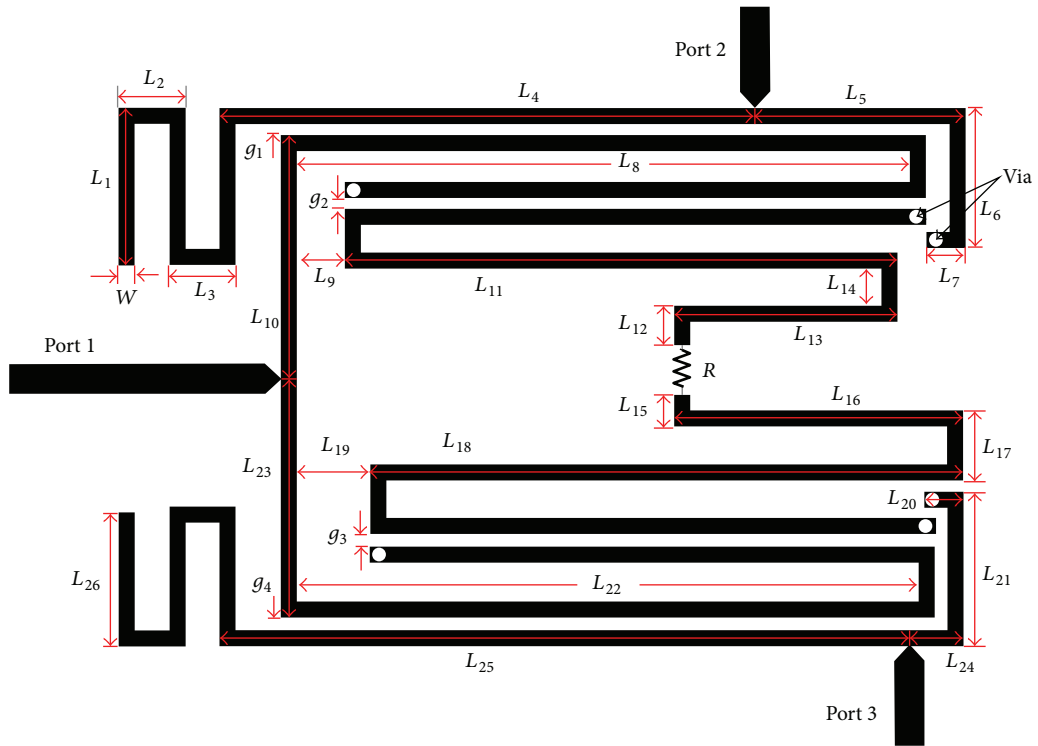


FIGURE 6: Configuration of the microstrip filtering unequal power divider.

TABLE 1: Comparison with previous work.

	$f_0$ (GHz)	In-band isolation (dB)	Isolation up to $2f_0$	Size ( $\lambda_g^2$ )	Bandpass response
[10]	2.65	>22	>5	0.009	No
[11]	2.4	>15	>5	0.174	Yes
[16]	2.05	>20	>10	0.125	Yes
[17]	0.92	>20	>20	0.021	Yes
This work	0.92	>17	>17	0.018	Yes

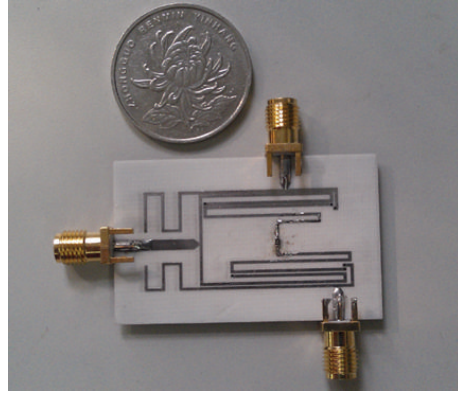


FIGURE 7: The photograph of the fabricated filter.

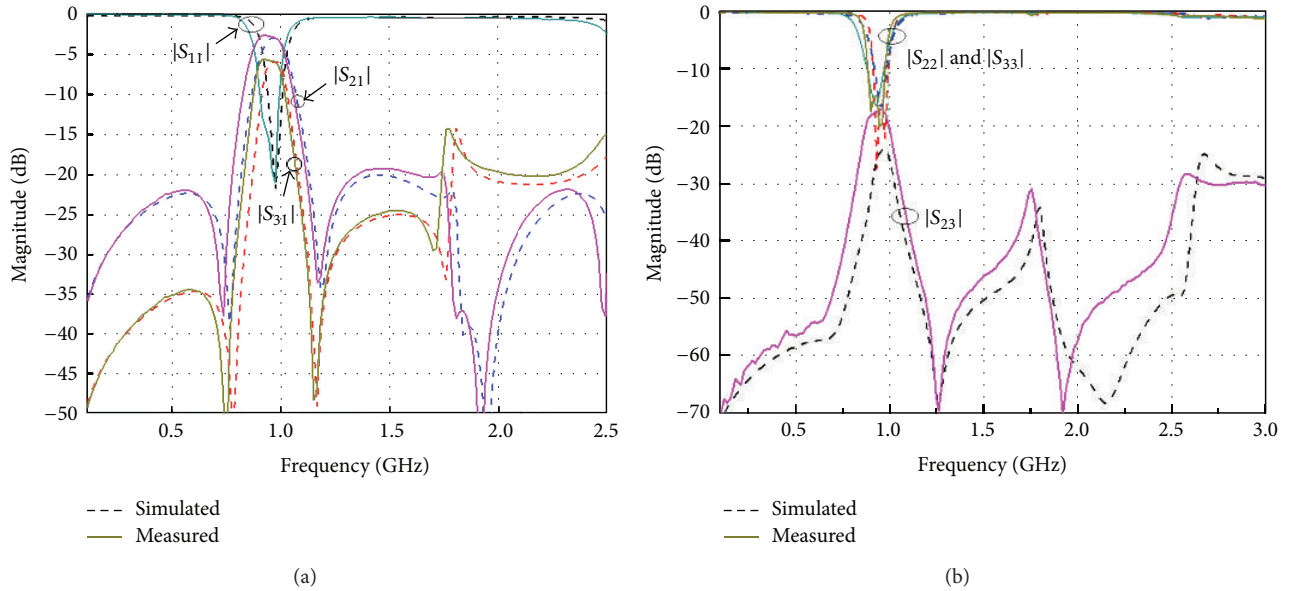


FIGURE 8: Simulated and measured results of the filtering power divider.

## Conflict of Interests

The authors declare that there is no conflict of interests regarding the publication of this paper.

## Acknowledgments

This work is supported by NSFC under Grant no. 61271060 and by Guangdong Natural Science Funds under Grant S2012010008742.

## References

- [1] F.-F. Fan, Z.-H. Yan, and W. Wang, "Wideband circularly polarized SIW antenna array that uses sequential rotation feeding," *International Journal of Antennas and Propagation*, vol. 2014, Article ID 534539, 8 pages, 2014.
- [2] H. Zhang, R. Chantalat, F. Torres, M. Thevenot, T. Monediere-and, and B. Jecko, "Low-profile array of wire patch antennas," *International Journal of Antennas and Propagation*, vol. 2009, Article ID 830931, 8 pages, 2009.
- [3] Y. Wu, Y. Liu, S. Li, and C. Yu, "Extremely unequal Wilkinson power divider with dual transmission lines," *Electronics Letters*, vol. 46, no. 1, pp. 90–91, 2010.
- [4] Z. Zhang, Y.-C. Jiao, S. Tu, S.-M. Ning, and S.-F. Cao, "A miniaturized broadband 4 : 1 unequal wilkinson power divider," *Journal of Electromagnetic Waves and Applications*, vol. 24, no. 4, pp. 505–511, 2010.
- [5] J.-L. Li and B.-Z. Wang, "Novel design of wilkinson power dividers with arbitrary power division ratios," *IEEE Transactions on Industrial Electronics*, vol. 58, no. 6, pp. 2541–2546, 2011.
- [6] Y. L. Lu, G.-L. Dai, and K. Li, "A novel unequal broadband out-of-phase power divider using DSPSLs," *ETRI Journal*, vol. 36, no. 1, pp. 116–123, 2014.
- [7] L. Xi and Y. Lin, "A novel design of dual-band Wilkinson power divider with simple structure and wide band-ratios characteristics," *Journal of Electromagnetic Waves and Applications*, vol. 28, no. 13, pp. 1635–1641, 2014.

- [8] D.-J. Eom and S. Kahng, "Fully printed dual-band power divider miniaturized by CRLH phase-shift lines," *ETRI Journal*, vol. 35, no. 1, pp. 150–153, 2013.
- [9] M. Hayati, S. Roshani, S. Roshani, and F. Shama, "A novel miniaturized Wilkinson power divider with  $n$  th harmonic suppression," *Journal of Electromagnetic Waves and Applications*, vol. 27, no. 6, pp. 726–735, 2013.
- [10] J. Wang, J. Ni, Y.-X. Guo, and D. Fang, "Miniaturized microstrip wilkinson power divider with harmonic suppression," *IEEE Microwave and Wireless Components Letters*, vol. 19, no. 7, pp. 440–442, 2009.
- [11] J.-Y. Shao, S.-C. Huang, and Y.-H. Pang, "Wilkinson power divider incorporating quasi-elliptic filters for improved out-of-band rejection," *Electronics Letters*, vol. 47, no. 23, pp. 1288–1289, 2011.
- [12] Y. C. Li, Q. Xue, and X. Y. Zhang, "Single-and dual-band power dividers integrated with bandpass filters," *IEEE Transactions on Microwave Theory and Techniques*, vol. 61, no. 1, pp. 69–76, 2013.
- [13] L. Gao and X. Y. Zhang, "Novel 2:1 Wilkinson power divider integrated with bandpass filter," *Microwave and Optical Technology Letters*, vol. 55, no. 3, pp. 646–648, 2013.
- [14] P.-H. Deng and L.-C. Dai, "Unequal wilkinson power dividers with favorable selectivity and high-isolation using coupled-line filter transformers," *IEEE Transactions on Microwave Theory and Techniques*, vol. 60, no. 6, pp. 1520–1529, 2012.
- [15] K. Song and Q. Xue, "Novel ultra-wideband (UWB) multi-layer slotline power divider with bandpass response," *IEEE Microwave and Wireless Components Letters*, vol. 20, no. 1, pp. 13–15, 2010.
- [16] S. S. Gao, S. Sun, and S. Xiao, "A novel wideband bandpass power divider with harmonic-suppressed ring resonator," *IEEE Microwave and Wireless Components Letters*, vol. 23, no. 3, pp. 119–121, 2013.
- [17] X. Y. Zhang, K.-X. Wang, and B.-J. Hu, "Compact filtering power divider with enhanced second-harmonic suppression," *IEEE Microwave and Wireless Components Letters*, vol. 23, no. 9, pp. 483–485, 2013.
- [18] W. Q. Pan, J. X. Xu, Q. F. Su, and X. L. Zhao, "Novel compact filtering power divider with harmonic suppression," *Progress in Electromagnetics Research C*, vol. 53, pp. 127–133, 2014.

## Research Article

# 2D Active Antenna Array Design for FD-MIMO System and Antenna Virtualization Techniques

**Ioannis Tzanidis,<sup>1</sup> Yang Li,<sup>1</sup> Gary Xu,<sup>1</sup> Ji-Yun Seol,<sup>2</sup> and JianZhong (Charlie) Zhang<sup>1</sup>**

<sup>1</sup>Wireless Communications Lab, Samsung R&D America, Richardson, TX 75082, USA

<sup>2</sup>Advanced Communications Lab, Communications Research Team, DMC R&D Center, Samsung Electronics Corp., 129 Samsung-ro, Yeongtong-gu, Suwon-si, Gyeonggi-do 443-742, Republic of Korea

Correspondence should be addressed to Ioannis Tzanidis; i.tzanidis@samsung.com

Received 12 February 2015; Revised 28 April 2015; Accepted 13 May 2015

Academic Editor: Xiu Yin Zhang

Copyright © 2015 Ioannis Tzanidis et al. This is an open access article distributed under the Creative Commons Attribution License, which permits unrestricted use, distribution, and reproduction in any medium, provided the original work is properly cited.

Full dimension MIMO (FD-MIMO) is one of the key technologies presently studied in the 3GPP for the next generation long-term evolution advanced (LTE-A) systems. By incorporating FD-MIMO into LTE/LTE-A systems, it is expected that system throughput will be drastically improved beyond what is possible in conventional LTE systems. This paper presents details on the 2D active antenna array design for FD-MIMO systems supporting 32 antenna elements. The FD-MIMO system allows for dynamic and adaptive precoding to be performed jointly across all antennas thus achieving more directional transmissions in the azimuth and elevation domains simultaneously, to a larger number of users. Finally, we discuss 2D antenna array port virtualization techniques for creating beams with wide coverage, necessary for broadcasting signals to all users within a sector, such as the CRS (Common Reference Signal).

## 1. Introduction

Recently, due to the expansion of new mobile smart devices and applications that require considerably larger amount of data compared to traditional voice calls, the wireless communication has experienced a significant increase of wireless data flow on a global scale [1]. Among such techniques are multiple-input multiple-output (MIMO), coordinated multipoint (CoMP) transmission/reception, and carrier aggregation (CA). CoMP relies on coordination between multiple transmission and reception points to enhance user equipment (UE) performance at cell edges but requires a very capable backhaul connection for intersite coordination. Carrier aggregation simultaneously utilizes multiple frequency bands to enhance peak data rate and a network's load balancing capability but requires the use of large frequency resources. Although each of these techniques represents a major step forward in improving system performance, further development of new technologies is required to meet the exponentially growing demand for wireless data traffic. In the meantime, the Third Generation Partnership Project (3GPP)

has pushed the standardization efforts on these emerging techniques, including FD-MIMO technology [2].

Full dimension MIMO (FD-MIMO) is one of the key technologies expected to boost the performance of LTE systems. One of the key technologies in FD-MIMO that leads to the impressive improvement on system throughput is to support up to 64 antenna ports placed in a 2D array. As compared to CoMP and CA, FD-MIMO is capable of enhancing system performance without requiring a very capable backhaul system or large frequency resources. Due to the large number of antenna elements it is a big challenge to accommodate high-order multiuser MIMO (MU-MIMO) transmission and reception without complicating the design and implementation of the devices in both base station and user (UE) sides to an impractical level. High-order MU-MIMO refers to the use of a large number of antennas at the base station to transmit or receive spatially multiplexed signals to or from a large number of terminals. Figure 1 depicts an overview of a FD-MIMO system. A 2D antenna array plane, deploying much more antenna elements than the traditional multiple antenna systems in wireless cellular

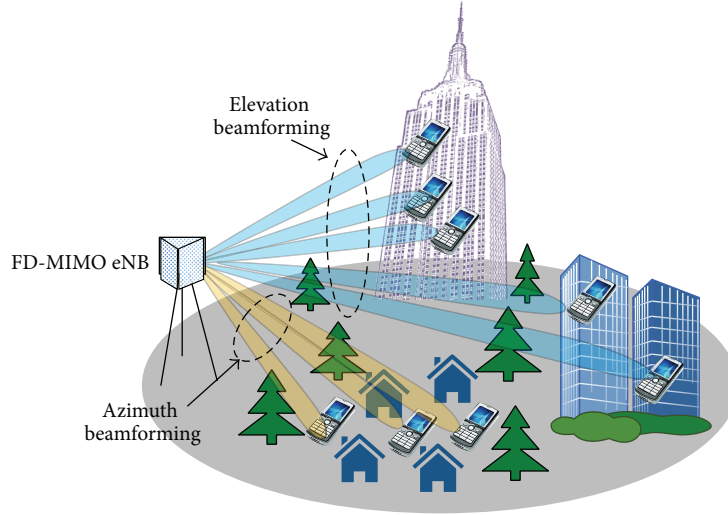


FIGURE 1: Conceptual diagram of FD-MIMO system realizing high-order MU-MIMO by utilizing 2D antenna array.

communications, is placed on the FD-MIMO base station. The antenna elements allow dynamic and adaptive precoding to be performed jointly across all antennas. As a result of such precoding, the base station achieves more directional transmissions in the azimuth and elevation domain simultaneously to a larger number of UEs.

The need for 3D beamforming demands a 3D Spatial Channel Model (SCM) where each signal path is assigned an angle in both azimuth and elevation domains. A key challenge for 3D SCM is to model the correlation of large scale parameters such as ASD (azimuth spread at departure), ASA (azimuth spread at arrival), ESD (elevation spread at departure), ESA (elevation spread at arrival), shadow fading, Rician  $K$ -factor, delay spread, and also the statistical distribution of elevation angles. In 3GPP a study item [2] will finalize the details of 3D SCM.

On the hardware implementation of FD-MIMO, a very important step is the design of a 2D active antenna array [3], that is, the choice of antenna array configuration, the number of horizontal and vertical elements, their polarization type (dual-linear, diagonal, etc.), and the element spacing (uniform, nonuniform, etc.). The key to this decision is a system level simulation, which is performed to analyze various antenna array configurations and compare their throughput with respect to a baseline design. The array configuration with the largest throughput is chosen. This is presented in Section 2. Section 3 presents the actual antenna element design, which entails the antenna element type, the antenna feed, and the antenna performance metrics such as the gain, beamwidth, bandwidth, polarization, and antenna isolation as dictated by the system simulations. The antenna array is then fabricated and measured in the anechoic chamber.

Another very important design step is antenna array port virtualization. 2D large antenna arrays are very suitable for forming narrow beams to multiple users simultaneously, but in a MIMO system there is also need for wide beams that transmit the same signal to all users in a sector at

the same time. Forming such wide beams could be resolved by transmitting from a single antenna element (since the element beamwidth is usually equal to the sector beamwidth); however, the transmitted power can be very low, resulting in limited coverage. In that regard it would be desirable to transmit from all 2D antenna array elements simultaneously and to be able to generate a beam with prescribed coverage. In Section 4 we compare various antenna array port virtualization techniques.

## 2. 2D Antenna Array Architectures

Choosing the most suitable 2D antenna array configuration is the most important step in realizing the gains of FD-MIMO technology. This refers to choosing the number of antennas in the horizontal (H) and vertical (V) dimension of the array, the polarization type (linear, dual-linear, alternating, colocated, etc.), and the element spacing in H and V dimensions. These parameters are impossible to determine without carrying out extensive numerical simulations in a system level. The deployment scenario (Urban Macro, Small Cell, etc.), the channel model, and the UE dropping (indoor, outdoor, vertical distribution, etc.) as well as scheduling algorithms are important simulation parameters that determine a suitable antenna array configuration. Figure 2 shows our simulation assumptions and comparison of four different antenna array configurations. All four configurations assume 32 antennas in an  $8H \times 4V$  configuration on the base station. In this example we study the effect of two different values of element spacing ( $0.5\lambda$  and  $2\lambda$ ) in the vertical dimension of the array (or elevation spacing, El. spacing) while the horizontal spacing (or azimuth spacing, Az. spacing) is fixed at  $0.5\lambda$ . For each of these two values of antenna spacing we consider two different polarization arrangements, a colocated dual-diagonal polarization (X-pol) antenna element arrangement and an alternating dual-diagonal polarization (Alt.-pol) arrangement as shown in Figure 2 at the bottom. In practice

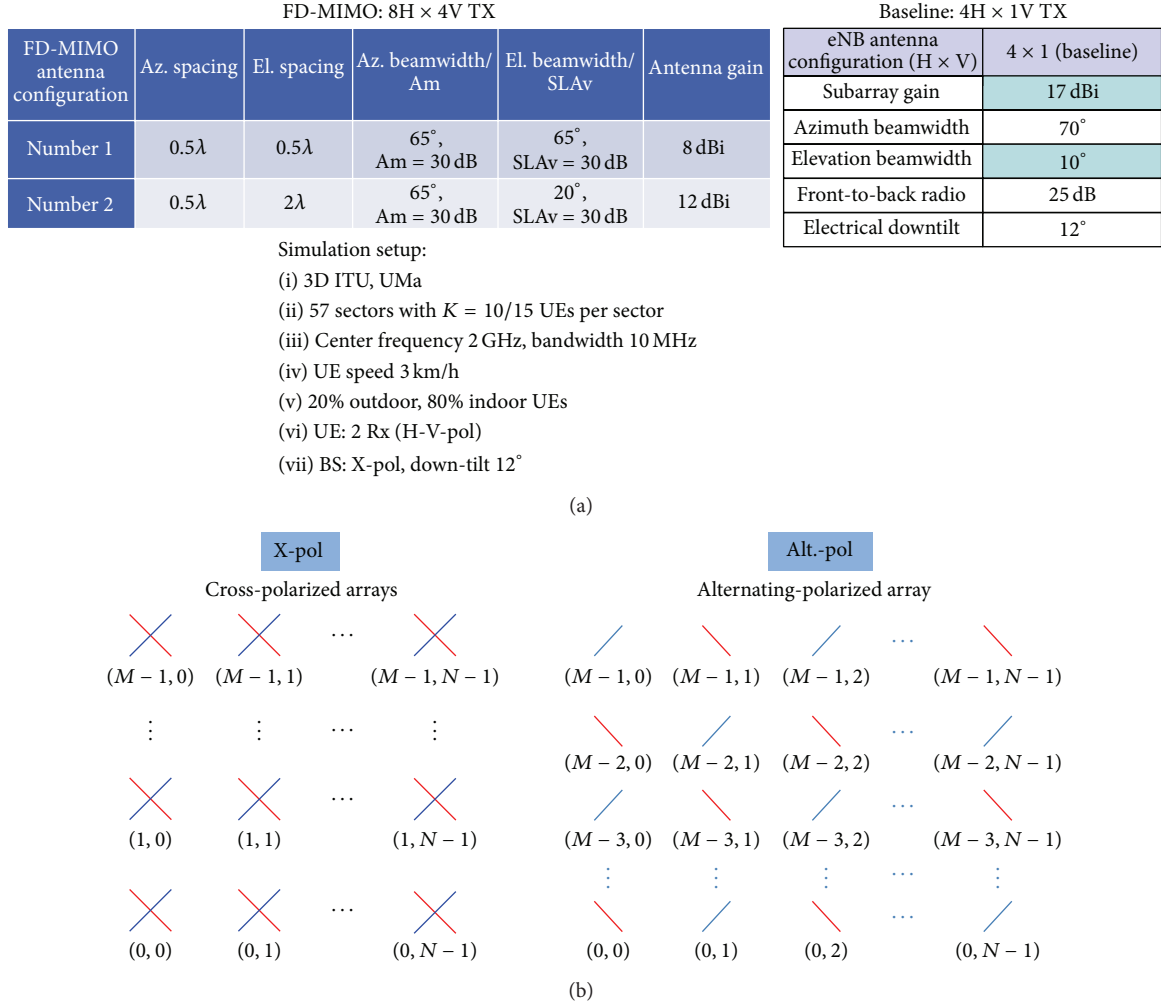


FIGURE 2: Comparison of four FD-MIMO antenna array architectures: two different antenna array configurations ( $0.5\lambda$  and  $2\lambda$  antenna element spacing in elevation) and two different antenna array polarization arrangements (a colocated cross-polarized array is referred to as X-pol, and an alternating-polarized array is referred to as Alt.-pol). Baseline configuration is shown on the top right of (a). Simulations assumptions are also given.

the X-pol antenna would be a dual-linearly polarized antenna element, while the Alt.-pol antenna would be a single linearly polarized antenna element. These antenna array configurations are compared against a baseline LTE eNB antenna array configuration shown in Figure 2 on the right.

The system level simulation results for the above four array architectures is shown in Table 1. The antenna array configuration that yields the largest throughput gains is that of  $2\lambda$  vertical spacing (El. spacing) and alternating polarization (Alt.-pol). This implementation is presented in the following section. Using our specific antenna parameters in conjunction with a 3D Spatial Channel Model (SCM) we report a promising average cell throughput gain (compared to the base line 4TX design) of approximately 4 times and cell edge throughput gain of 8.2x, (namely, 8.2 times higher throughput) compared to our baseline: a 4TX state-of-the-art 4G LTE system. Simulation results are shown in Table 1.

### 3. 2D Active Antenna Array Design and Performance

In order to realize the benefit of FD-MIMO, an efficient implementation of a 2D antenna array is a key requirement [4–6]. An actual functioning example of an FD-MIMO array configuration is shown in Figure 3. As dictated by the system level simulations, the array comprises 32 subarrays, which comprise our antenna elements in an  $8H \times 4V$  configuration. Each antenna element is actually a subarray configuration ( $1H \times 4V$ ) of four single patch antennas fed by a common feed port. The spacing between two adjacent subarrays is  $d_H = 0.5\lambda$  in the horizontal direction and  $d_V = 2\lambda$  in the vertical direction (between centers of adjacent subarrays). Each subarray is composed of four patch antenna elements fed with equal magnitude and phase by a single feed port. Thus, the FD-MIMO array has a total of 32 feed ports (corresponding to

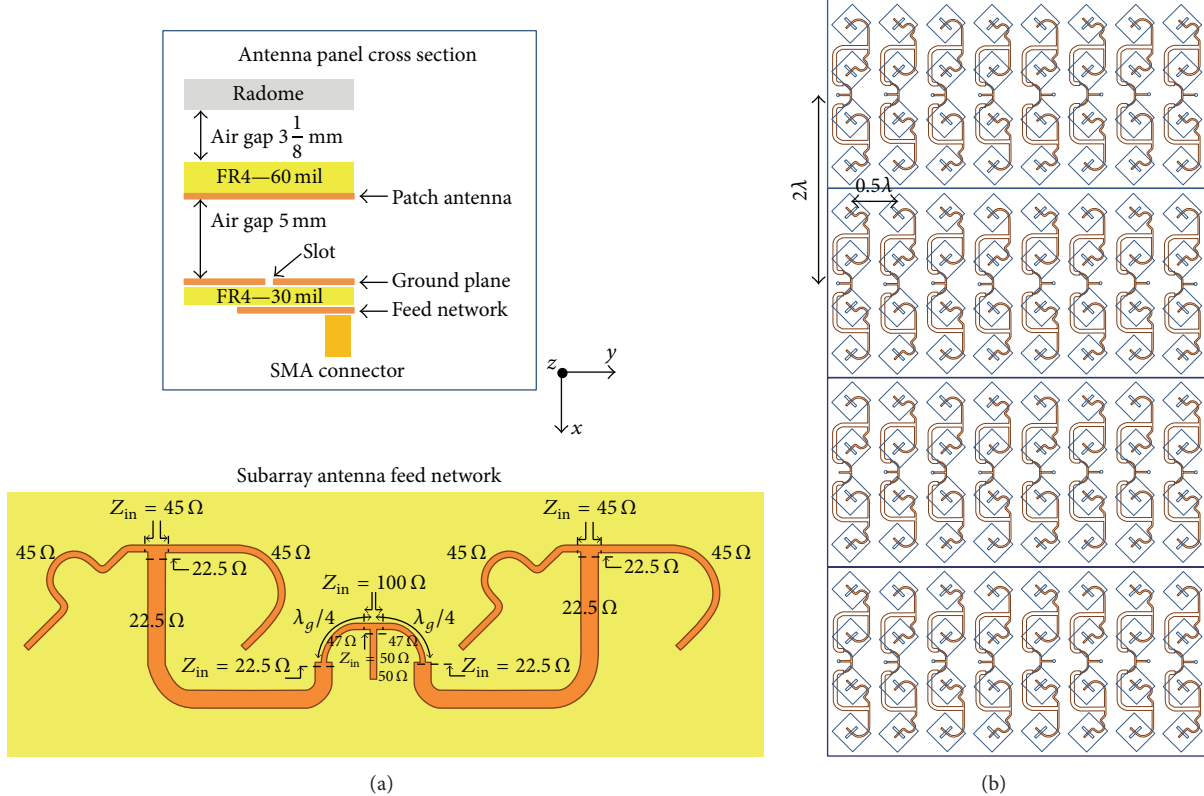


FIGURE 3: (a) Bottom view of one subarray feed network and detailed PCB stack-up, and (b) top-to-bottom view of FD-MIMO antenna array unit and feed network.

TABLE 1: System level simulation of antenna array architectures. Throughput gain compared to the baseline design of 4TX antennas.

Antenna array type	Throughput gain (over baseline 4TX)	
	Cell avg.	Cell edge
Config. 1 ( $0.5\lambda$ )		
X-pol	2.4x	4.15x
Alt.-pol	3.3x	5.5x
Config. 2 ( $2\lambda$ )		
X-pol	3.5x	5x
Alt.-pol	4x*	8.2x*

\* Our implementation.

32 channels) and a form factor of approximately 1 m in height by 50 cm in width.

One of the key features of this FD-MIMO array configuration is that the patch antenna elements are arranged in the  $\varphi = \pm 45^\circ$  directions which results in linear polarization on the two diagonal planes ( $\varphi = \pm 45^\circ$  with reference to the coordinate system shown in Figure 3). A close look at the antenna array unit on the right side of the Figure 3 reveals that the patch antenna subarrays are actually alternating orientation (hence, polarization) along the row and column dimension of the array. For instance, in the 4-element subarray at the top left corner of the array unit, patch antennas are rotated such that their polarization plane

coincides with the  $\varphi = -45^\circ$  plane, with respect to the rectangular coordinate system convention shown in Figure 3. Notice that, in the subarray immediately to the right, patch antennas are rotated  $90^\circ$  so that they are polarized on the  $\varphi = +45^\circ$  plane. This alternating scheme continues along both array dimensions. Due to this configuration, the  $+45^\circ$  and  $-45^\circ$  polarized subarrays have the same beamwidths in the elevation ( $\varphi = 0^\circ$ ) and azimuth ( $\varphi = 90^\circ$ ) planes and are affected more alike by the channel characteristics than would a  $0^\circ$  and  $90^\circ$  polarized array version. Notice also that the  $+45^\circ$  and  $-45^\circ$  subarrays are alternating along both horizontal and vertical directions as dictated by system level simulations. This technique increases the isolation (or decreases coupling) between adjacent subarrays since they are orthogonally polarized.

The patch elements of each subarray are fed through a corporate microstrip line feed network printed on the bottom layer of the feed board. Energy is coupled to the patches through rectangular slot cutouts on the ground plane, on the other side of the feed board. This feeding technique provides better bandwidth, higher isolation between adjacent patch elements, and also more flexibility in adjusting the air-gap between the antenna and feed board (see board stack-up detail in Figure 3) than the conventional probe feeding technique [7]. The air gap between the antenna board and the feed board (ground plane) is tuned so as to maximize the bandwidth and achieve the specified gain and beamwidth as

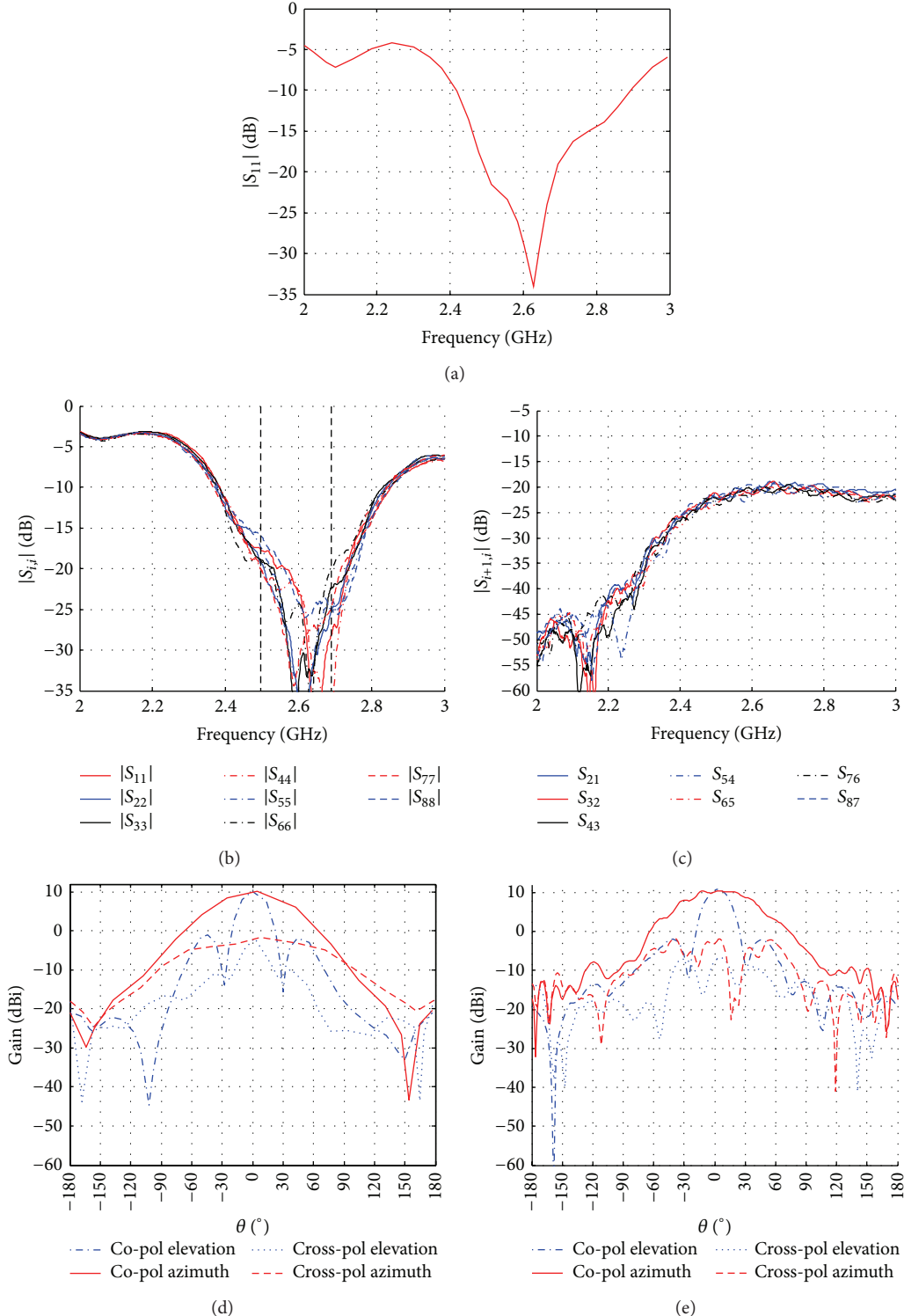


FIGURE 4: FD-MIMO antenna panel measurements. The panel has 8 alternating polarization subarrays. (a) Simulated reflection coefficient magnitude for a single subarray. (b) Measured reflection coefficient magnitude for 8 subarrays within one FD-MIMO antenna panel. (c) Measured coupling coefficient magnitudes between adjacent subarrays in one panel. (d) Simulated co-pol and cross-pol radiation patterns of one subarray on azimuth ( $\varphi = 90^\circ$ ) and elevation ( $\varphi = 0^\circ$ ) planes at 2.6 GHz. (e) Corresponding measured radiation patterns.

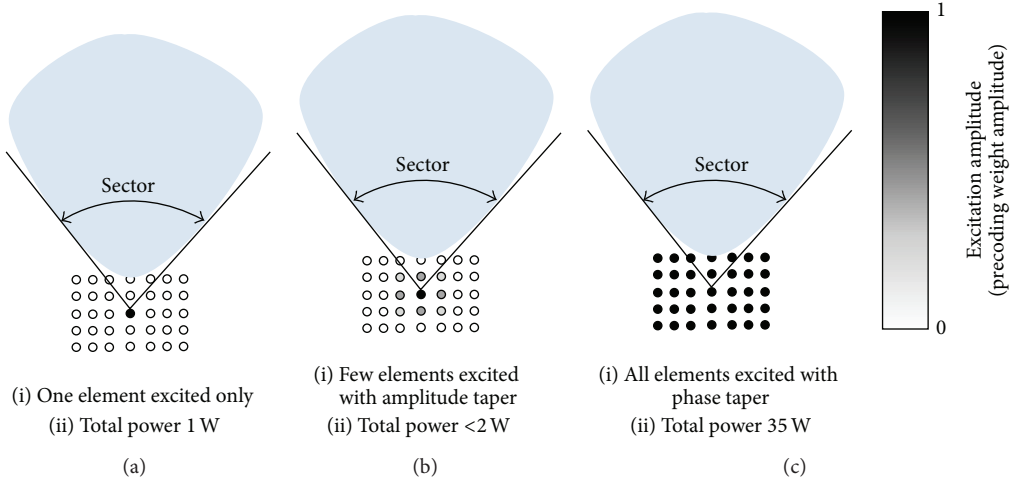


FIGURE 5: Methods to create wide beam patterns in 2D arrays.

dictated by the system level simulation assumptions shown in Figure 2.

For consistent radiation, it is important that all subarrays be phase matched, that is, the difference of electrical lengths from the feed ports to the patch antennas should not exceed more than  $1^\circ \sim 2^\circ$ . To ensure phase matching, all subarrays have the same feed network adjusted to fit both  $\pm 45^\circ$  rotated patch subarrays by merely mirroring the microstrip sections, as seen in Figure 3 (mirroring sections in our case does not change the electrical length). Further, within each 4-element patch subarray, all microstrip sections were phase matched to better than  $1.4^\circ$ , from the common feed port to each patch antenna.

The antenna is designed to support FD-MIMO in the LTE TDD band #41 (2.496–2.69 GHz) and can achieve a gain of about 10 dBi per subarray with beamwidths of  $25^\circ$  and  $65^\circ$  in the azimuth and elevation domains, respectively. The performance is close to the simulation assumptions of Figure 2. This gain value is the realized gain, which includes the loss in the subarray feed network which was separately measured to be 2.15 dB. Figure 4 shows simulation and measurement results for one panel of the array (8 subarrays) in an anechoic chamber environment. Each subarray has lower than 15 dB return loss ( $-15$  dB reflection coefficient) in the target band while the mutual coupling between adjacent subarrays is below  $-20$  dB. Mutual coupling in patch antenna arrays has been investigated in [8]. Low mutual coupling in conjunction with the high return loss yields very low cross-correlation between antenna ports (less than  $-35$  dB). Simulated and measured copolarized and cross-polarized radiation patterns for one subarray on the azimuth and elevation planes at 2.6 GHz are also shown in Figure 4. The subarray co-pol gain is measured at about 10 dBi at  $\theta = 0^\circ$  and the cross-pol gain is measured at about 10 dB below that. The beamwidths on the azimuth and elevation planes are about  $65^\circ$  and  $24^\circ$ , respectively.

#### 4. Antenna Array Port Virtualization

In FD-MIMO systems the use of channel estimation and multiuser precoding algorithms allows the formation of multiple narrow beams allocated to the various users. However, besides the user-specific data transmitted by the narrow beams, FD-MIMO base stations need to broadcast data intended for all users to receive simultaneously, such as control channel and CRS (Common Reference Signal). Such signals cannot be transmitted via a narrow beam but rather via a wide beam with beamwidth that covers the entire sector.

Two methods are generally adopted in practice for generating a wide beam: (1) transmit only from one antenna array element and (2) transmit from multiple elements each with a certain amplitude weighting taper (pattern synthesis) [9]. Both methods have disadvantages. The first method transmits very little power since only one element (out of typically a few decades of elements) is excited. Thus the range is limited and gain control (AGC) is needed on the user side. The second method suffers from a similar problem, since the method synthesizes a given beam pattern resulting in amplitude taper that heavily excites a few antenna elements at the center of the array while the majority of the elements are excited with very little power.

To generate wide beam with all antenna elements excited at full power is not a trivial task, because, in general, a fully excited antenna array generates a narrow beam pattern. Thus, in order to generate a wide beam with certain beamwidths in azimuth and elevation and all antenna elements excited at full power (amplitude equals to 1) a certain phase taper has to be applied. That phase taper has to be somewhat robust, to account for possible phase errors in the phase calibration process.

Figure 5 summarizes the two commonly used methods to generate a 2D wide beam that covers a specific sector angle. Although the sector is shown in 1D (azimuth cut), the reader should visualize a similar sector, yet maybe narrower,

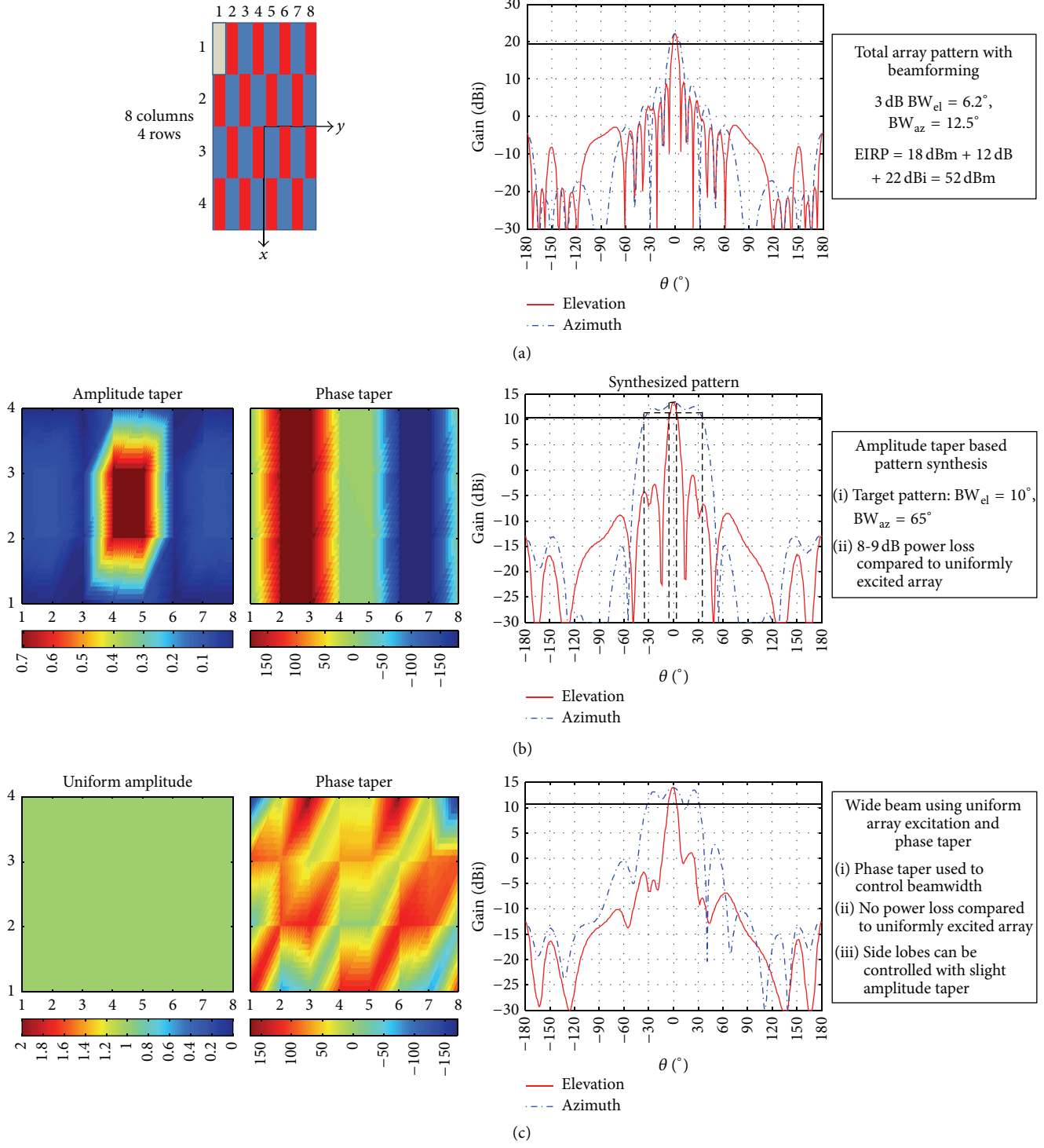


FIGURE 6: (a) Our implementation of a 2D FD-MIMO antenna array with the beamforming gain pattern. (b) A classic method to synthesize a wide beam pattern with specific beam widths in elevation and azimuth, using an aggressive amplitude taper, where the majority of antenna array elements are almost unexcited. (c) Method to generate a wide beam pattern using a phase taper and uniform amplitude taper.

in the second dimension (elevation). As seen in Figure 5 left, a wide beam can be generated by just exciting only one array element. If we assume that the array elements can transmit a maximum power of 1W, then the first method of exciting only one element (represented by black

color) results in only 1W of power being transmitted and hence in limited coverage and range. The second method (Figure 5 middle), employs pattern synthesis with amplitude taper to synthesize a wide beam. Again, although only one dimension is shown in Figure 1, the reader should visualize

a 2D pattern with azimuth and elevation beamwidths that cover a specific sector. The second method results in slightly higher transmitted power, since only the center element is fully excited (represented by black color), while a few elements to its left and right are only slightly excited (very low amplitude represented by grey color). Still, the majority of array elements are not excited (white color) resulting in low transmitted power and thus limited range.

The third method, illustrated in Figure 5 on the right, shows a technique where all array elements are excited fully with equal amplitudes but different phases. As a result, a desired 2D beam pattern can be generated with the total transmitted power being equal to the maximum available transmitted power of the PA of each antenna element. Thus we can expect the range to be maximized and the requirements on the dynamic range of the AGC to be relaxed.

As an example we apply these techniques to our antenna array shown in Figure 3. Figure 6(a) shows the gain beam pattern on the elevation and azimuth planes when all 32 antenna array elements are excited with the same phase. As seen, the resulting 3 dB beamwidth is about  $6.2^\circ$  in elevation domain and  $12.5^\circ$  in the azimuth domain. If the transmit power per antenna element is assumed to be 18 dBm, then the EIRP will be  $18 \text{ dBm} + 12 \text{ dB} (\text{PA gain}) + 22 \text{ dBi} (\text{array gain per polarization}) = 52 \text{ dBm}$  (per polarization).

In Figure 6(b) the amplitude taper method (Fourier Transform Method) is adopted to synthesize a wide beam with  $10^\circ$  beamwidth in elevation and  $65^\circ$  beamwidth in azimuth. As mentioned earlier, the amplitude taper technique leaves the majority of antenna elements not excited (see amplitude taper in Figure 6(b)), resulting in a heavy power loss of the order of 8 dB, as compared to the fully excited array. Thus the PA gain in that case will only be  $12 \text{ dB} - 8 \text{ dB} = 4 \text{ dB}$  and thus the EIRP will drop to  $18 \text{ dBm} + 4 \text{ dB} (\text{PA gain}) + 12 \text{ dBi} (\text{array gain per polarization}) = 34 \text{ dBm}$ . This can result in very limited range.

In Figure 6(c) we demonstrate the phase taper technique. This technique excites all antenna elements with full power, thus maintaining full PA gain while it shapes the pattern to the specified beamwidths by phase taper. The resulting beam pattern using the phase taper method is shown in Figure 6(c). The result of the phase taper is an EIRP of about 42 dBm.

One concern when dealing with phase weights is the sensitivity to phase errors. Phase errors occur from many sources such as temperature variation of active components, part-by-part variation in passive components, and nonuniform dielectric substrates. To account for these phase inconsistencies advanced calibration methods are employed which adjust the phase of each active chain at the baseband level such that all signals arrive at the antenna ports with the prescribed phase weights. Antenna calibrations are regular intervals during system operation. Despite calibration, FD-MIMO arrays with large number of active chains can never be perfectly phase calibrated. For small array ( $< 8$  antennas), calibration aligns channels to within a few degrees of error (about  $\pm 5^\circ$ ). If the phase error between channels is more than  $10^\circ$ , the calibration circuit might not be performing adequately. For arrays with many active chains calibration errors can be higher because of error propagation in calibration

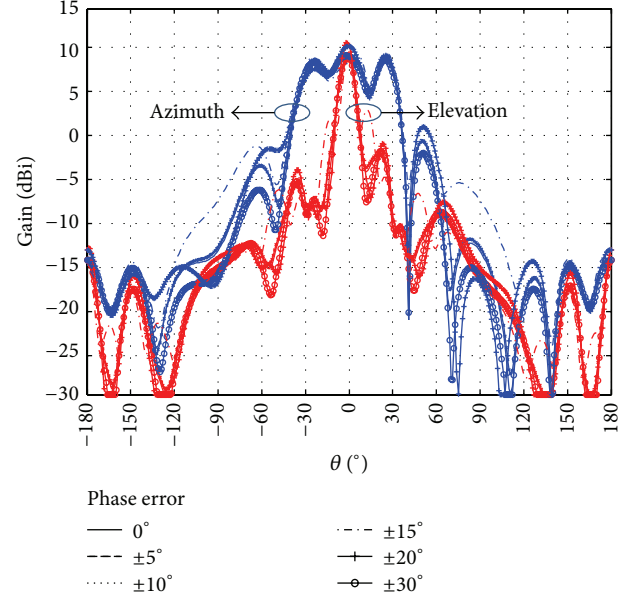


FIGURE 7: Robustness of phase taper method to phase errors.

methods [10]. Thus, a phase taper method for generating wide beam patterns has to be able to maintain its robustness despite small phase uncertainties.

Figure 7 shows the performance of the phase taper technique in presence of random phase errors of a maximum of  $\pm 5^\circ$  up to  $\pm 30^\circ$ . We would like to note that during our phase error analysis a phase error, for example, of  $\pm 15^\circ$  meant that the phase of some randomly selected elements was allowed to vary up to that amount. Still, most antenna elements were randomly assigned a phase error of less than  $\pm 15^\circ$ . As seen in Figure 7, the phase taper method is somewhat robust to phase errors. Phase errors primarily affect the gain ripple within the main lobe and also side lobe levels. We noticed that beyond  $\pm 30^\circ$  of maximum phase error beamwidth was affected more heavily. Because all antenna array elements are excited with uniform amplitude (see Figure 6(c)), random errors in the phase taper method can be balanced out in wide beamwidth cases and for arrays with many elements, and this is the reason why the phase taper method exhibits robustness to phase errors.

## 5. Conclusions

In this paper, we presented the design and performance of a FD-MIMO 2D active antenna array system. We carried out system level simulations to compare various antenna array configurations and understand their impact on the system performance (throughput gain). We found that  $2\lambda$  antenna spacing and alternating polarization scheme yields the highest throughput gains with a practically realizable form factor. Further, we designed and measured the antenna array that meets the assumptions of the system level simulation. Finally, we compared two methods for generating wide beam pattern in large 2D FD-MIMO arrays. Such wide beams are required for signals that are intended to be transmitted not separately

to each user but to a whole sector of specific azimuth and elevation dimensions. We found that the amplitude taper method can result in low transmitted power and thus in low range, whereas the phase taper method can maintain full transmit power and is robust to phase errors of up to  $\pm 30^\circ$ .

## Conflict of Interests

The authors declare that there is no conflict of interests regarding the publication of this paper.

## References

- [1] Cisco, *Cisco Visual Networking Index: Global Mobile Data Traffic Forecast Update, 2012–2017*, Cisco, 2013.
- [2] 3GPP TSG RAN Plenary #58, R1-122034, Study on 3D-channel model for Elevation Beamforming and FD-MIMO studies for LTE, Barcelona, Spain, 2012.
- [3] B. L. Ng, Y. Kim, J. Lee et al., “Fulfilling the promise of massive MIMO with 2D active antenna array,” in *Proceedings of the IEEE Globecom Workshops (GC Wkshps ’12)*, pp. 691–696, December 2012.
- [4] Y.-H. Nam, B. Ng, K. Sayana et al., “Full-dimension MIMO (FD-MIMO) for next generation cellular technology,” *IEEE Communications Magazine*, vol. 51, no. 6, pp. 172–179, 2013.
- [5] Y. Kim, H. Ji, J. Lee et al., “Full dimension mimo (FD-MIMO): the next evolution of MIMO in LTE systems,” *IEEE Wireless Communications*, vol. 21, no. 2, pp. 26–33, 2014.
- [6] S. Akoum and J. Acharya, “Full-dimensional MIMO for future cellular networks,” in *Proceedings of the IEEE Radio and Wireless Symposium (RWS ’14)*, pp. 1–3, Newport Beach, Calif, USA, January 2014.
- [7] M. Civerolo and D. Arakaki, “Aperture coupled patch antenna design methods,” in *Proceedings of the IEEE International Symposium on Antennas and Propagation (APSURSI ’11)*, pp. 876–879, July 2011.
- [8] D. R. Jackson, W. F. Richards, and A. Ali-Khan, “Series expansions for the mutual coupling in microstrip patch arrays,” *IEEE Transactions on Antennas and Propagation*, vol. 37, no. 3, pp. 269–274, 1989.
- [9] C. A. Balanis, *Antenna Theory: Analysis and Design*, Wiley Interscience, 3rd edition, 2005.
- [10] J. McCormack, T. Cooper, and R. Farrell, “Tower-top antenna array calibration scheme for next generation networks,” *EURASIP Journal on Wireless Communications and Networking*, vol. 2007, Article ID 41941, 2007.

## Research Article

# A CPW-Fed Quasi-PIFA Antenna Using Quasi-Lumped Resonators for Mobile Phones

**Majid Rafiee, Mohd Fadzil bin Ain, and Aftanasar Md. Shahar**

*School of Electrical and Electronics Engineering, Universiti Sains Malaysia, Engineering Campus Seberang Perai Selatan, 14300 Nibong Tebal, Penang, Malaysia*

Correspondence should be addressed to Majid Rafiee; rafiee6@gmail.com

Received 27 July 2014; Revised 2 November 2014; Accepted 3 November 2014

Academic Editor: Sai-Wai Wong

Copyright © 2015 Majid Rafiee et al. This is an open access article distributed under the Creative Commons Attribution License, which permits unrestricted use, distribution, and reproduction in any medium, provided the original work is properly cited.

A novel single CPW-fed Quasi-Planar Inverted-F Antenna (PIFA) using quasi-lumped elements is developed for mobile communication handheld terminals operating at 2.6 GHz. The antenna is composed of an inductor covered by a set of interdigital and parasitic capacitors. The proposed antenna achieves a measured bandwidth of 11% for return loss with the antenna gain of about 4 dBi. The antenna is designed in single layer (zero height) which is appropriate to be used in thin devices where a small room is considered for the antenna. The proposed antenna is suitable for use in Long Term Evolution band 7. The operating frequency of introduced antenna depends on the number of interdigital fingers and inductor length rather than the total resonator patch only, so that the operating frequency can be altered while the total patch size remains unchanged. The calculated operating frequency is confirmed by simulation and measurement. Also the dipole-like simulated radiation pattern is confirmed by measurement.

## 1. Introduction

Nowadays, wireless devices have a vital role of having almost constant connectivity worldwide. By decreasing the size of future wireless devices, there is a corresponding demand for similar size reduction in antenna elements, as well. However the performance of the antenna strongly depends on its size so that it becomes more complicated in contrast to the complexity which communication infrastructure is faced with [1]. The present-day challenge for antenna designers is to provide wide bandwidth, high efficiency while reducing the equipment size. Planar Inverted-F Antenna (PIFA) which resonates at quarter-wavelength is an ideal choice for mobile phones for its low profile and low inherent signal absorption ratio (SAR) compared to the patch antennas.

Numerous researches have been done on widening and CPW-fed techniques of not only monopole antennas [2, 3] but also PIFA antennas in terms of bandwidth enhancement [4], single/multiple resonant frequencies [5, 6], reconfigurability [7], tunability [8], and radiation pattern improvement [9]. PIFA is better choice for cellphones antennas where a limited space is considered for the antenna to be integrated.

The conventional internal PIFA antennas have a high profile of almost up to 10 mm on the top of ground plane in order to get wide bandwidth. However the PIFA's bandwidth strongly depends on the vertical distance between the resonating strip and ground plane while in the recent cell phones, thin profile is more attracted in the market. Although PIFA occupies much smaller space, its 3-dimensional structure where the patch is located above the system ground plane leads to occupying high profile and being more structurally challenging as compared to 2-dimensional planar antennas.

Like other kind of antennas, miniaturizing is an interesting challenge which many of researchers face. Many techniques are introduced to miniaturize the size of this kind of antenna such as using meander line or capacitive loading. A reconfigurable multiband planar antenna is presented in [10] which has 2D structure where a MEMS switch operates as a short-circuited in ON state which enables the antenna to resonate at quarter-wavelength. A planar printed PIFA antenna using a resonating strip is also introduced in [11]. In this paper an alternative single-feed structure of PIFA antenna using quasi-lumped elements in only a single layer is presented where it can satisfy the desired characteristics of

PIFA antennas while not only does it have 2D structure, but also the bandwidth is not sensitive to the antenna height.

The  $LC$  resonators are commonly used in dipole and multifrequency monopole antennas. However, [12] introduced a new approach in PIFA design by employing the  $LC$  resonator as a resonating strip. A network of interdigital and parasitic capacitors and an inductor to shape the main resonating element are presented in this paper. However the interdigital capacitors are widely used in filters. It is also used as a feeding structure for impedance matching in [13]. However, it has not, to our knowledge, been used neither as a main resonator in antenna nor in PIFA designs. It will be shown that by using this shape, the operating frequency does not depend on wavelength directly since it can be tuned by adjusting the numbers of interdigital capacitors, inductor length, and capacitors width while the total size of the patch is unchanged. Next section presents the antenna's structure which can be located on the back cover of cellphones.

## 2. Antenna Design

**2.1. Inductor's Inductance and Interdigital Capacitors' Capacitance.** A deep analysis on both radiating and balanced mode of PIFA antenna and its impedance variation is done by [14]. The  $10 \times 8$  mm resonator element contains *quasi-lumped elements* including an inductor covered by a set of interdigital capacitors and two parasitic capacitors on the same layer where the ground plane is located. The inductor  $L$  with the length of  $L_I$  is covered by two sets of multifinger interdigital capacitors with the length of  $L_c$  at the center of the resonator which are shown in Figure 1. The inductance can be increased by increasing the length of inductor line  $L_I$  (i.e., using the meander line). On the other hand, the number of fingers can control the capacitance of the interdigital capacitors. The inductance of the inductor and capacitance of the interdigital capacitors per unit length along  $H_q$  can be calculated using (1) [15] and (2) [16], respectively, as follows:

$$L = 200 \times 10^{-9} L_I \left[ \ln \left( \frac{2L_I}{W_I + t} \right) + \left( 0.50049 + \frac{W_I}{3L_I} \right) \right], \quad (1)$$

$$C_I = (\epsilon_r + 1) L_C [(N - 3) A_1 + A_2] \text{ (pF/unit length)}, \quad (2)$$

where  $t$  is metal thickness,  $\epsilon_r$  is the substrate permittivity,  $N$  is number of fingers, and  $A_1$  and  $A_2$  are the capacitance per unit length of the fingers and can be calculated by

$$A_1 = 4.409 \tanh \left[ 0.55 \left( \frac{h}{W_C} \right)^{0.45} \right] \times 10^{-6} \text{ (pF}/\mu\text{m}), \quad (3)$$

$$A_2 = 9.920 \tanh \left[ 0.52 \left( \frac{h}{W_C} \right)^{0.50} \right] \times 10^{-6} \text{ (pF}/\mu\text{m}).$$

The general expression for total series capacitance of an interdigital capacitor can also be expressed by [17]

$$C_I = 2\epsilon_0 \epsilon_{re} \frac{K(k)}{K(k')} (N - 1) L_C \text{ (F)} \\ = \frac{10^{-11}}{18\pi} \epsilon_{re} \frac{K(k)}{K(k')} (N - 1) L_C \times 10^{-4} \text{ (F)}, \quad (4)$$

$$C_I = \frac{\epsilon_{re} 10^{-3}}{18\pi} \frac{K(k)}{K(k')} (N - 1) L_C \text{ (pF)}, \quad (5)$$

where  $L_C$  is in microns and  $\epsilon_{re}$  is the effective dielectric constant of the microstrip line of width of  $W$  and can be achieved by

$$\epsilon_{re} = \frac{(\epsilon_r + 1)}{2} + \frac{(\epsilon_r - 1)}{2} \left[ 1 + \frac{10h}{W} \right]^{-0.5}. \quad (6)$$

Also the ratio of complete elliptic integral of first kind  $K(k)$  and its complement  $K(k')$  is given by

$$\frac{K(k)}{K(k')} = \frac{1}{\pi} \ln \left[ 2 \left( \frac{1 + \sqrt{k}}{1 - \sqrt{k}} \right) \right] \text{ for } 0.707 \leq k \leq 1, \quad (7a)$$

$$\frac{K(k)}{K(k')} = \frac{\pi}{\ln [2((1 + \sqrt{k'}) / (1 - \sqrt{k'}))] \quad (7b)} \\ \text{for } 0 \leq k \leq 0.707,$$

where

$$k = \tan^2 \left( \left( \frac{\pi}{4} \right) \left( \frac{W_C}{W_C + D_G} \right) \right); \quad k' = \sqrt{1 - k^2}. \quad (8)$$

In this paper,  $W_C = D_G$ , the ratio of elliptic integral is unity, so that (5) can be simplified to

$$C_I = \epsilon_0 \left( \frac{\epsilon_r + 1}{2} \right) [(N - \Delta) L_C], \quad (9)$$

where  $\Delta$  is the value of width correction factor (the edge effect of the first and last fingers) and can be approximated to 0.44, 0.65, and 0.5 for  $N = 1$ ,  $N = 2$ , and  $N \geq 3$ , respectively [16, 18].

**2.2. Parasitic Capacitor's Capacitance.** Figure 1 depicts two capacitors known as parasitic capacitors,  $C_{P_1}$  and  $C_{P_2}$ , respectively. The value of  $C_{P_1}$  and  $C_{P_2}$  can be determined using the three-dimensional finite difference method which was proposed by [19]. The capacitance of coplanar parasitic capacitors can be calculated using

$$C_{P_i} = \frac{(Q_{\text{total}} - X \cdot Q')}{V}; \quad i = 1, 2, \quad (10)$$

where  $Q_{\text{total}}$  is the total charge on the conductor,  $Q'$  is the charge per unit length on the connected microstrip transmission line,  $V$  is the potential difference between patch conductor and ground plane, and  $X$  is the distance between the back-transformed reference plane of discontinuity and the magnetic wall (transmission lines are considered to be surrounded by a shield of magnetic and electric walls).  $Q_{\text{total}}$  and  $Q'$  are needed to calculate  $C_{P_i}$  in (10).

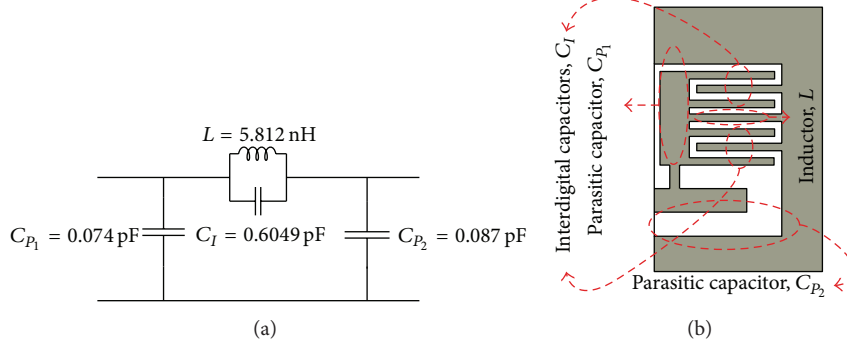


FIGURE 1: (a) Equivalent circuit and (b) inductor and parasitic/interdigital capacitors scheme.

2.2.1.  $Q'$ . The charge per unit on the connected transmission line can be obtained by

$$Q' = \epsilon_0 \epsilon_r \oint_C E_n \cdot ds, \quad (11)$$

where  $C$  is the delineation of integration section which surrounds the cross section at the plane of the magnetic wall and  $E_n$  is the electrical field distribution on  $n$  times repeated grid sections. The accuracy of these potentials appertain on the number of  $n$  so that having more iteration parts increases the accuracy. According to [19],  $n = 60$  is good enough to an accuracy better than 1% for calculating equivalent capacitance of an open-ended microstrip line. By applying the boundary conditions to Taylor's series expansion, the electrical potential  $\Phi$  in the immediate vicinity inside the  $x - z \geq 0$  plane of each point can be calculated by

$$\begin{aligned} \Phi = & \left( \frac{d\epsilon_1 + c\epsilon_2}{ab} + \frac{\epsilon_1}{d} + \frac{\epsilon_2}{C} + \frac{d\epsilon_1 + c\epsilon_2}{ef} \right)^{-1} \\ & \times \left( \frac{d\epsilon_1 + c\epsilon_2}{a(a+b)} \Phi_A + \frac{d\epsilon_1 + c\epsilon_2}{b(a+b)} \Phi_B + \frac{\epsilon_2}{c} \Phi_C \right. \\ & \left. + \frac{\epsilon_1}{d} \Phi_D + \frac{d\epsilon_1 + c\epsilon_2}{e(e+f)} \Phi_E + \frac{d\epsilon_1 + c\epsilon_2}{f(e+f)} \Phi_F \right), \end{aligned} \quad (12)$$

where  $a, b, c, d, e$ , and  $f$  are the distance of calculated potential points from the considered point which are shown in Figure 2. For instance (13) and (14) deliver the optimum value of electrical potential for two desired points at position  $P$  and  $Q$ , respectively, as follows:

$$\begin{aligned} \Phi_P = & \left( \frac{1}{a+b} \right) (bcdef\Phi_A + acdef\Phi_B) \\ & + \left( \frac{1}{c+d} \right) (abdef\Phi_C + abcef\Phi_D) \\ & + \left( \frac{1}{e+f} \right) (abcde\Phi_E + abcde\Phi_F), \end{aligned} \quad (13)$$

$$\begin{aligned} \Phi_Q = & \left( \frac{e+f}{2} \right) (bcdef\Phi_A + acdef\Phi_B) \\ & + \left( \frac{\epsilon_r(a+b)(e+f)}{2(\epsilon_r d + c)} \right) \left( \frac{abdef}{\epsilon_r} \Phi_C + abcef\Phi_D \right) \\ & + \left( \frac{a+b}{2} \right) (abcd\Phi_E + abcde\Phi_F) \\ & - (a+b)(c+d)(e+f). \end{aligned} \quad (14)$$

The electrical field at each grid section can be achieved by

$$\vec{E} = -\vec{\nabla}\Phi. \quad (15)$$

The electrical potential can be calculated using Laplace's equation as a linear combination of finite difference expression of neighboring grid points at each grid point inside the shield [19]. Using "relaxation method," (16) will be achieved as follows:

$$\Phi_{\text{new}} = \Phi_{\text{old}} - K \cdot R, \quad (16)$$

where  $K$  is the relaxation constant and assigns the speed of convergence. Naghed and Wolff [19] state the optimal value of 1.8 for this solution.

2.2.2.  $Q_{\text{total}}$ . The total charge on the conductor can be calculated using the electrical field distribution as follows:

$$Q_{\text{total}} = \epsilon_0 \epsilon_r \iint_A \vec{E} \cdot \vec{n} dx dz. \quad (17)$$

Let us assume that the distances to the back and lateral electric walls ( $X/2$  and  $Z/2$ ) and also to the magnetic wall and to the upper surface ( $Y/2$ ) are all equal to  $h$ . The potentials are presumed to be  $\Phi_1 = \Phi_2 = 1 \text{ V}$  and zero on the ground plane ( $\Phi_0 = 0$ ). Hence the equivalent capacitances  $C_{P_1}$  and  $C_{P_2}$  can be achieved as follows:

$$\begin{aligned} C_{P_1} &= (Q_{1,\text{total}} - X_1 \cdot Q'_1), \\ C_{P_2} &= (Q_{2,\text{total}} - X_2 \cdot Q'_2). \end{aligned} \quad (18)$$

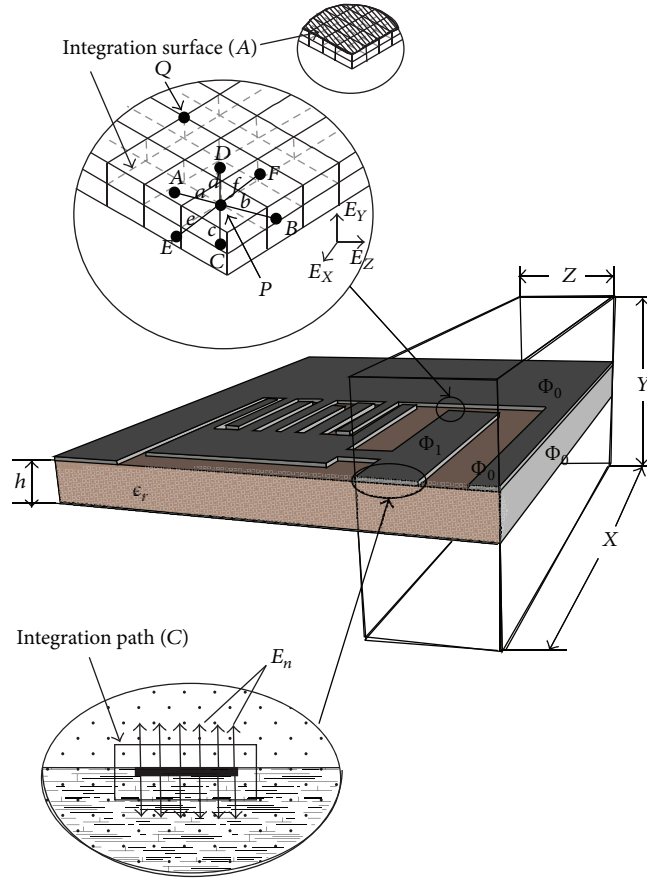


FIGURE 2: Calculation of total charge and charge per unit length for the first parasitic capacitor.

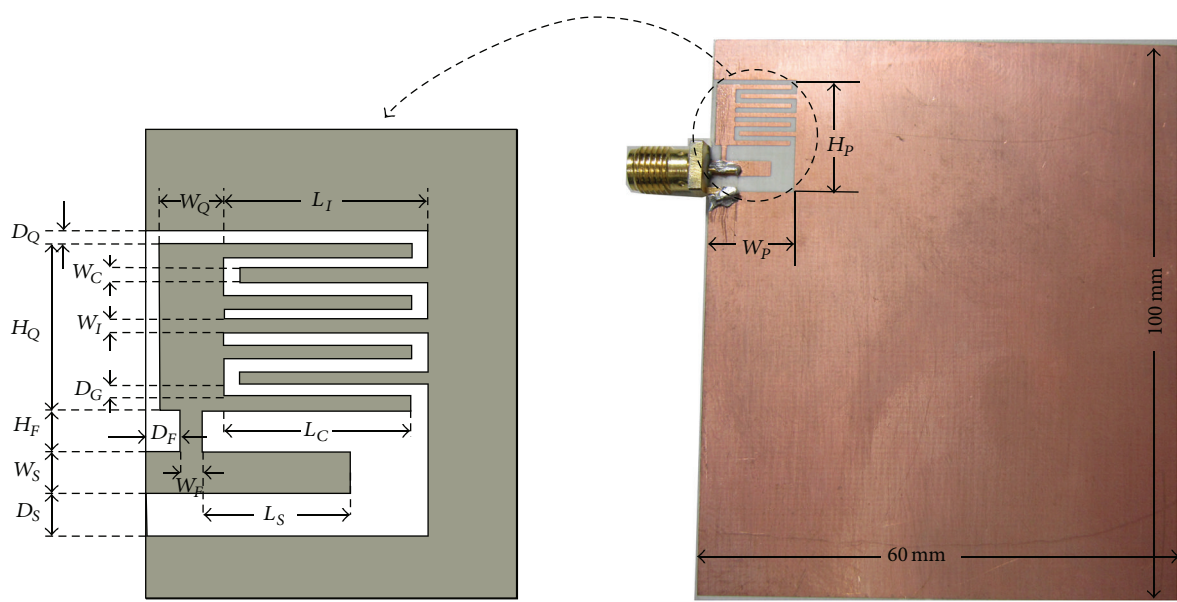


FIGURE 3: The geometry of the printed CPW-feeding structure of PIFA using quasi-lumped *LC* resonators.

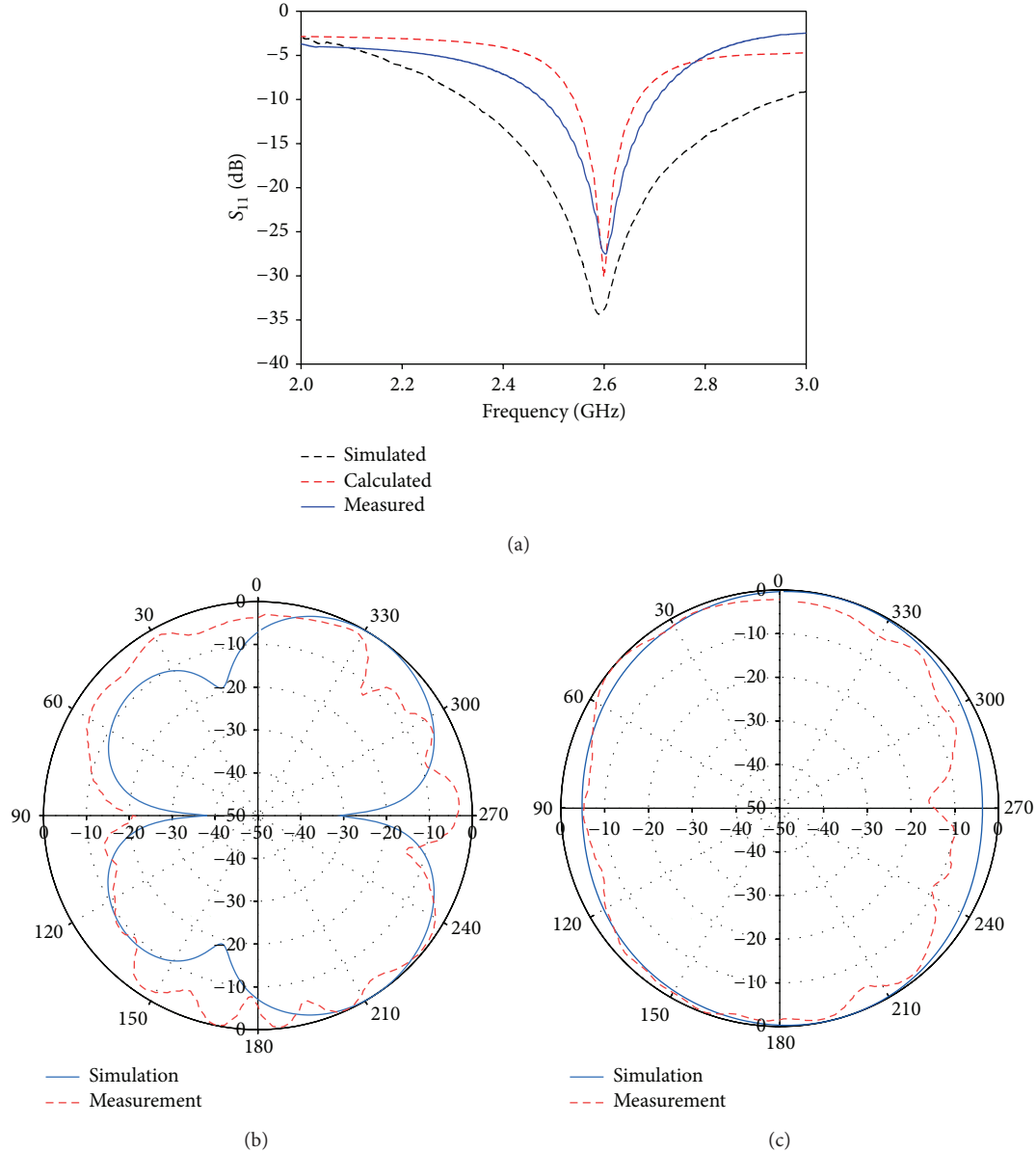


FIGURE 4: (a) Simulated, calculated, and measured return loss and radiation pattern for (b) E-Plane and (c) H-Plane.

The calculated values (which are shown in Figure 1(a)) of  $L$ ,  $C_I$ ,  $C_{P_1}$  ( $W/h \approx 2.45$ ) and  $C_{P_2}$  ( $W/h \approx 3.08$ ) are 5.812 nH, 0.6049 pF, 0.074 pF, and 0.087 pF, respectively. Finally, the resonant frequency can be achieved by

$$f = \frac{1}{2\pi\sqrt{L\left(\left(C_{P_1}C_{P_2}/(C_{P_1} + C_{P_2})\right) + C_I\right)}} \quad (19)$$

### 3. Results

Figure 3 exhibits the printed antenna's prototype on a Duriod R4003c substrate with  $100 \times 60 \times 0.813$  mm dimensions and  $\epsilon_r = 3.38$ . The antenna has been measured and successfully verified at the Penang Skills Development Centre (PSDC). The simulated and measured results are shown in Figure 4.

In accordance with the measured results for the 6 dB return loss specifications in Figure 4(a), it implies that the antenna operates at LTE band 7 with 83% of radiation efficiency. In addition, the simulated Smith chart and current distribution are illustrated in Figures 5(a) and 5(b), respectively.

Equation (19) can explain a distinct advantage of the proposed antenna which depends on the wavelength indirectly. This means that the resonant frequency can be tuned by number, width, and length of fingers while the total patch size remains unchanged. The term *indirectly* is used since still the resonance of antenna depends on the wavelength since by varying the overall dimensions of the patch either in  $H_Q$  or  $W_Q$ , the resonant frequency will be shifted. However, as it can be observed, the antenna specifications can be controlled by tuning the capacitance and inductance by adjusting the value of controlling parameters.

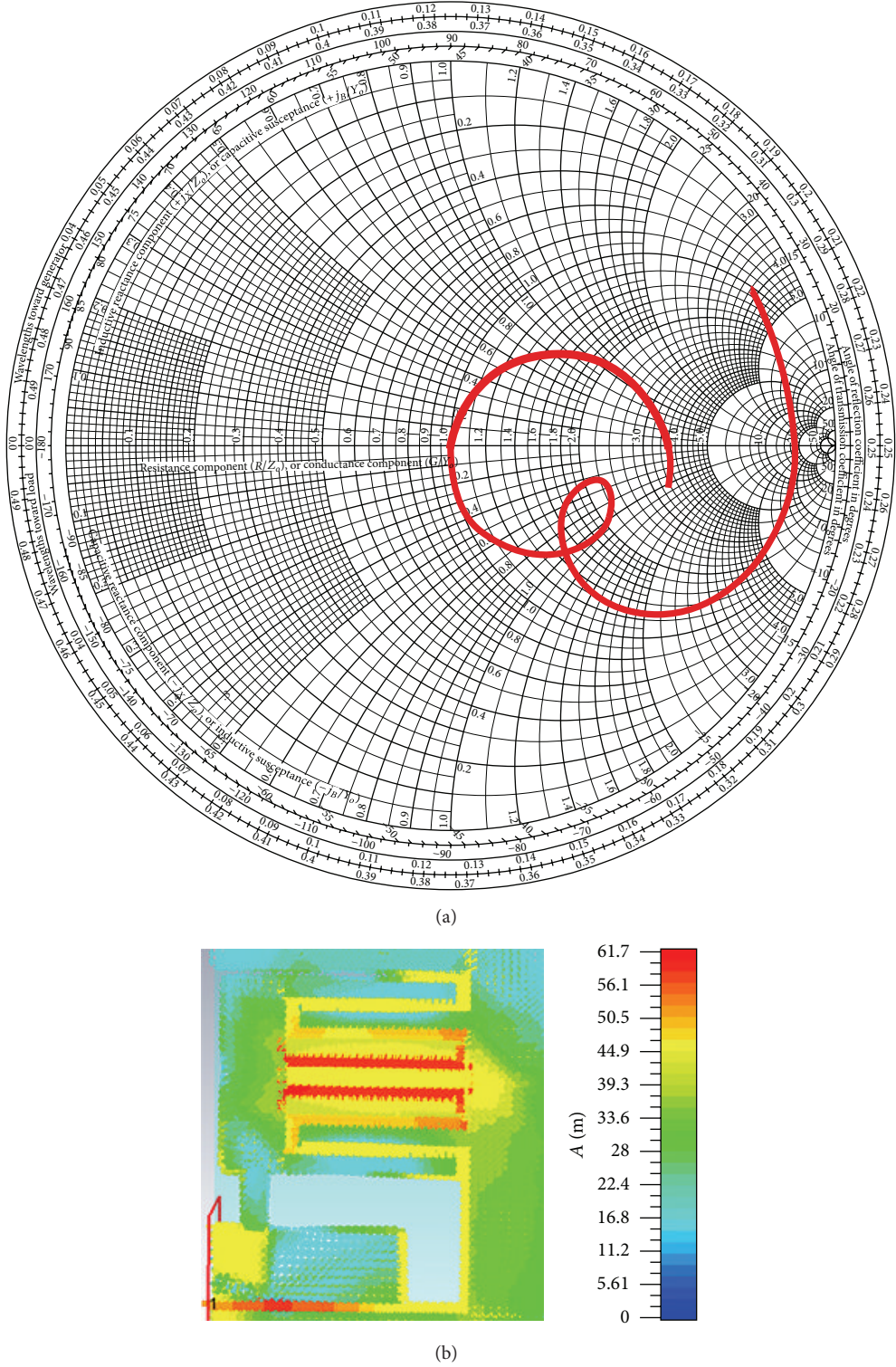


FIGURE 5: (a) Simulated Smith chart and (b) current distribution.

The first parasitic capacitor is controlled by  $L_S$  and  $W_S$ . The second parasitic capacitor also can be adjusted using  $W_Q$  and  $H_Q$ . The inductor length ( $L_I$ ), interdigital capacitors width ( $W_C$ ), and total number of interdigital capacitors fingers play a critical role in determining not only operating

frequency, but also the bandwidth of this kind of antenna. The value of these parameters is quite sensitive since not only do they have direct effect on antenna operating frequency, but also the input impedance can be matched by using the right value for them. In present study, the  $W_S$  is arrogated to cover

TABLE 1: Parameters.

Parameter	Size (mm)	Parameter	Size (mm)
$H_P$	15	$W_S$	1.989
$H_Q$	8	$L_I$	7.835
$H_F$	2	$L_C$	7.22
$W_P$	10.835	$L_S$	5.735
$W_Q$	2.5	$D_F$	1.4
$W_F$	0.7	$D_G$	0.615
$W_C$	0.615	$D_S$	0.615
$W_I$	0.615	$D_Q$	2

LTE band 7. For sure, other geometry parameters affect the impedance matching, as well. All the optimized parameters are summarized in Table 1 to achieve the optimum value.

Furthermore the measured and simulated radiation patterns at center frequency are plotted in Figures 4(b) and 4(c). Dipole-like patterns are observed, which illustrate no outstanding difference compared to regular internal mobile antennas and are almost the same to those seen in them. The slight distinctions can be imputed to the feeding cable influences on the antenna radiation patterns.

## 4. Conclusion

A quasi-PIFA antenna is designed to operate at LTE band 7 (2.6 GHz). The quasi-lumped patch which includes two parasitic capacitors, an inductor, and a network of interdigital capacitor is short-circuited to the ground at the end. The antenna operating frequency can be tuned not only by patch size, but also by the number of fingers ( $N$ ), length ( $L_I$ ), and width ( $W_C$ ) of inductor and interdigital capacitors, respectively. The proposed antenna is fabricated in a 2D single layer while the conventional PIFA antennas usually are fabricated in 3D. This makes the fabrication process much easier and more precise. In addition, many components must be integrated above the ground plane and below the main resonator in conventional 3D PIFA which affect the antenna performance. The proposed antenna in this paper occupies much smaller volume compared to other kinds of PIFA antenna and is better choice for integration in small applications where the space is quite valuable. Also the strong dependency of PIFA on very sensitive parameter of conventional 3D-PIFA, its height, is eliminated using this approach. Although LTE band 7 is chosen as a sample frequency to show the antenna performance, it can be tuned to other desired frequencies by small variation in the affecting parameters which were discussed in this paper. The antenna has been examined in the laboratory which shows good agreement regarding simulation and measurement results.

## Conflict of Interests

The authors declare that there is no conflict of interests regarding the publication of this paper.

## Acknowledgment

The authors wish to thank Universiti Sains Malaysia for funding this project under USM Fellowship scheme and grant numbers 1001/PELECT/814202 USM RUT.

## References

- [1] D. A. Sanchez-Hernandez, *Multiband Integrated Antennas for 4G Terminals*, Artech House, 2008.
- [2] M. R. Aghda, M. R. Kamarudin, and H. U. Iddi, "M-shape surrounded with ring patch wideband monopole printed antenna," *Microwave and Optical Technology Letters*, vol. 54, no. 2, pp. 482–486, 2012.
- [3] M. Rafiee, M. F. Ain, and M. S. Aftanasar, "A novel UWB octagonal semi-ring antenna with CPW-wing-shaped ground plane," *Progress In Electromagnetics Research Letters*, vol. 41, pp. 113–123, 2013.
- [4] H. T. Chattha, M. K. Ishfaq, Y. Saleem, Y. Huang, and S. J. Boyes, "Band-notched ultrawide band planar inverted-F antenna," *International Journal of Antennas and Propagation*, vol. 2012, Article ID 513829, 6 pages, 2012.
- [5] M. Koubeissi, M. Mouhamadou, C. Decroze, D. Carsenat, and T. Monédier, "Triband compact antenna for multistandard terminals and user's hand effect," *International Journal of Antennas and Propagation*, vol. 2009, Article ID 491262, 7 pages, 2009.
- [6] K. R. Boyle and P. J. Massey, "Nine-band antenna system for mobile phones," *Electronics Letters*, vol. 42, no. 5, pp. 265–266, 2006.
- [7] P. Panaïa, C. Luxey, G. Jacquemod, R. Staraj, L. Petit, and L. Dussopt, "Multistandard reconfigurable PIFA antenna," *Microwave and Optical Technology Letters*, vol. 48, no. 10, pp. 1975–1977, 2006.
- [8] L. Mo and C. Qin, "Tunable compact UHF RFID metal tag based on cpw open stub feed PIFA antenna," *International Journal of Antennas and Propagation*, vol. 2012, Article ID 167658, 8 pages, 2012.
- [9] E. Bonek, P. Nowak, and J. Fuhl, "Improved internal antenna for hand-held terminals," *Electronics Letters*, vol. 30, no. 22, pp. 1816–1818, 1994.
- [10] A. C. K. Mak, R. R. Rowell, R. D. Murch, and C.-L. Mak, "Reconfigurable multiband antenna designs for wireless communication devices," *IEEE Transactions on Antennas and Propagation*, vol. 55, no. 7, pp. 1919–1928, 2007.
- [11] C.-H. Chang and K.-L. Wong, "Printed  $\lambda/8$ -PIFA for pentaband WWAN operation in the mobile phone," *IEEE Transactions on Antennas and Propagation*, vol. 57, no. 5, pp. 1373–1381, 2009.
- [12] G. K. H. Lui and R. D. Murch, "Compact dual-frequency PIFA designs using LC resonators," *IEEE Transactions on Antennas and Propagation*, vol. 49, no. 7, pp. 1016–1019, 2001.
- [13] J.-X. Liu and W.-Y. Yin, "A compact interdigital capacitor-inserted multiband antenna for wireless communication applications," *IEEE Antennas and Wireless Propagation Letters*, vol. 9, pp. 922–925, 2010.
- [14] K. R. Boyle and L. P. Lighthart, "Radiating and balanced mode analysis of PIFA antennas," *IEEE Transactions on Antennas and Propagation*, vol. 54, no. 1, pp. 231–237, 2006.
- [15] B. C. Wadell, *Transmission Line Design Handbook*, Artech House, Norwood, Mass, USA, 1991.

- [16] G. D. Alley, "Interdigital capacitors and their application to lumped-element microwave integrated circuits," *IEEE Transactions on Microwave Theory and Techniques*, vol. 18, 1970.
- [17] I. J. Bahl, *Lumped Elements for RF and Microwave Circuits*, Artech House, 2003.
- [18] J.-S. G. Hong and M. J. Lancaster, *Microstrip Filters for RF/Microwave Applications*, John Wiley & Sons, 2004.
- [19] M. Naghed and I. Wolff, "Equivalent capacitances of coplanar waveguide discontinuities and interdigitated capacitors using a three-dimensional finite difference method," *IEEE Transactions on Microwave Theory and Techniques*, vol. 38, no. 12, pp. 1808–1815, 1990.

## Research Article

# High Selectivity Dual-Band Bandpass Filter with Tunable Lower Passband

Wei-Qiang Pan, Xiao-Lan Zhao, Yao Zhang, and Jin-Xu Xu

School of Electronic and Information Engineering, South China University of Technology, Guangzhou 510641, China

Correspondence should be addressed to Xiao-Lan Zhao; eexlzhao@126.com

Received 31 December 2014; Accepted 28 February 2015

Academic Editor: Dimitrios Sounas

Copyright © 2015 Wei-Qiang Pan et al. This is an open access article distributed under the Creative Commons Attribution License, which permits unrestricted use, distribution, and reproduction in any medium, provided the original work is properly cited.

This paper presents a novel method to design dual-band bandpass filters with tunable lower passband and fixed upper passband. It utilizes a trimode resonator with three controllable resonant modes. Discriminating coupling is used to suppress the unwanted mode to avoid the interference. Varactors are utilized to realize tunable responses. The bandwidth of the two bands can be controlled individually. Transmission zeros are generated near the passband edges, resulting in high selectivity. For demonstration, a tunable bandpass filter is implemented. Good agreement between the prediction and measurement validates the proposed method.

## 1. Introduction

The bandpass filters which are used to reject the unwanted signals have been widely investigated [1]. Meanwhile, to meet the requirement of the multiband operations, various methods have been proposed to design multiband bandpass filters [2–5]. Recently, electronically tunable bandpass filters have drawn much attention due to their capacity to deal with various operating frequencies in a system. Varactors are loaded at the ends of the resonators to adjust the operating frequencies [6]. Besides the frequency, the bandwidth of a tunable filter also should be taken into consideration [7–9]. In [7], suitable coupling region is selected to keep the bandwidth constant. Besides tunable single-band bandpass filters, tunable dual-band bandpass filters also have been widely researched [10–16]. In [11, 12], varactors are equipped at the center of stub-loaded open-ended resonator, resulting in a fixed lower passband and a tunable upper passband. To realize frequency tuning at both passbands, varactors are loaded not only at the center stub but also at the end of main transmission line [13]. For further convenient adjustment, two sets of resonators are employed [14–16]. By controlling different voltages, both of the two bands can be tuned.

However, most of the above references focus on designing dual-band filters with tunable upper passband, and few literatures address bandpass filters with a tunable lower

passband and a fixed upper passband. The potential problem associated with this type of tunable filters is that the harmonic of the lower passband may overlap with the fixed upper passband.

To avoid this problem, we propose a novel method of using trimode resonators to design the tunable dual-band bandpass filter. The second mode (middle frequency) and third mode (highest frequency) of the trimode resonator are utilized to form the lower and upper passbands, respectively. The first mode (lowest frequency) is suppressed by discriminating coupling to eliminate the interference with the passband so that the selectivity can be enhanced. The second mode can be tuned by the varactors without affecting third mode, resulting in a tunable lower passband and fixed upper passband. Meanwhile, transmission zeros are synchronously changed with the passband, ensuring high skirt selectivity.

## 2. Design Theory

Figure 1(a) shows the proposed stub-loaded trimode resonator. It consists of a main transmission line and three open stubs. The characteristic admittance and the electronic length of each stub are shown. It is symmetric in structure; thus, even- and odd-mode method can be used to characterize it and its odd- and even-mode equivalent circuits are shown as in Figures 1(b) and 1(c). Since Figures 1(b) and 1(c) are still

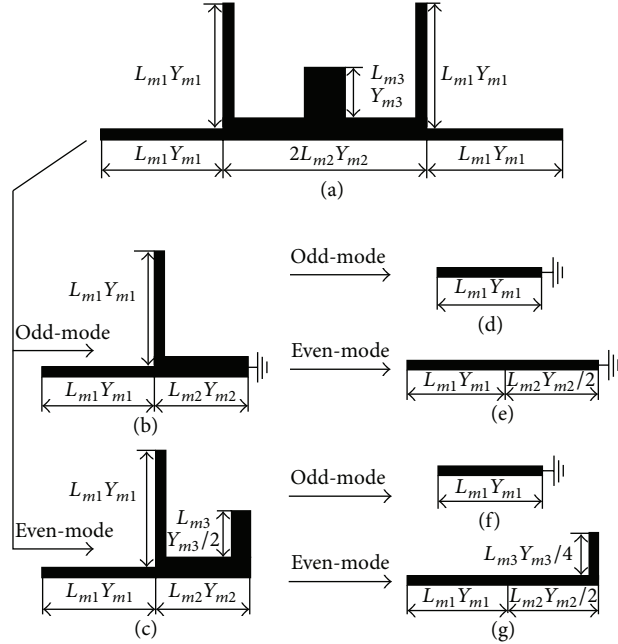


FIGURE 1: (a) The proposed stub-loaded trimode resonator; (b) odd-mode circuit of (a); (c) even-mode circuit of (a); (d) odd-mode circuit of (b); (e) even-mode circuit of (b); (f) odd-mode circuit of (c); (g) even-mode circuit of (c).

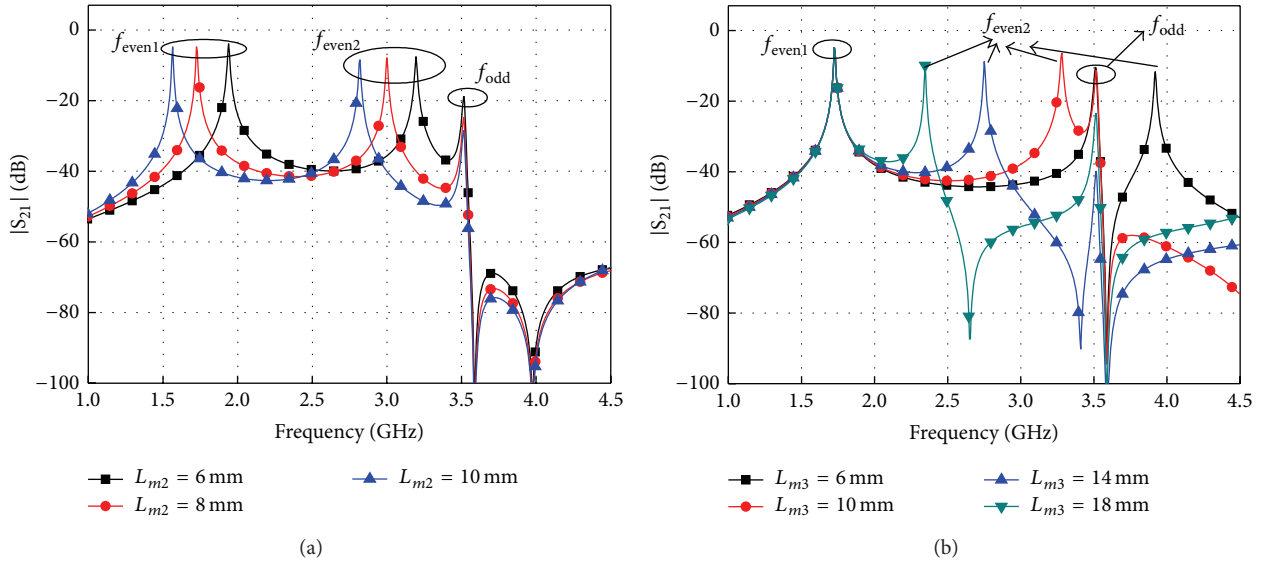


FIGURE 2: Simulated  $|S_{21}|$  against (a)  $L_{m2}$ ; (b)  $L_{m3}$ .

symmetric, even- and odd-mode method can be further used to analyze them. The corresponding equivalent circuits are shown as Figures 1(d)–1(g). Under the special condition of  $Y_{m3} = 2Y_{m2} = 4Y_{m1}$ , the resonant frequencies of Figures 1(d), 1(e), 1(f), and 1(g) can be deduced as follows [2]:

$$f_{odd1} = \frac{c}{4L_{m1}\sqrt{\epsilon_{eff}}},$$

$$f_{even1} = \frac{c}{4(L_{m1} + L_{m2})\sqrt{\epsilon_{eff}}},$$

$$f_{odd2} = \frac{c}{4L_{m1}\sqrt{\epsilon_{eff}}},$$

$$f_{even2} = \frac{c}{2(L_{m1} + L_{m2} + L_{m3})\sqrt{\epsilon_{eff}}},$$

(1)

where  $c$  is the light speed in free space and  $\epsilon_{eff}$  denotes the effective dielectric constant of the substrate. Comparing the four frequencies,  $f_{odd1}$  and  $f_{odd2}$  are the same, and we

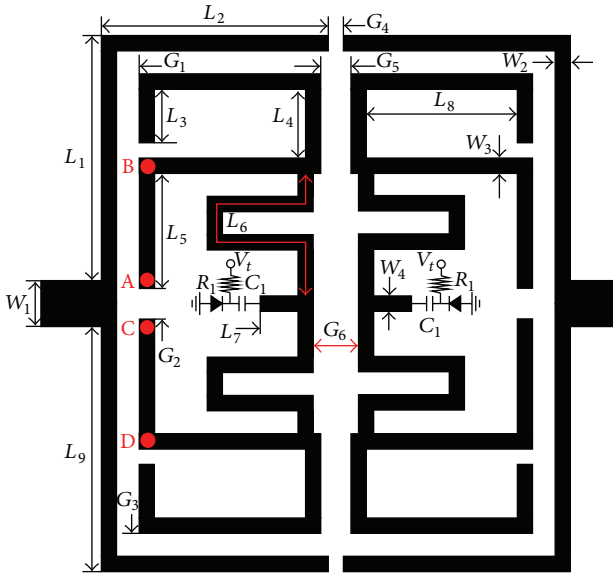


FIGURE 3: Structure of the proposed tunable dual-band filter.

use  $f_{\text{odd}}$  to denote them. Meanwhile, we can obtain  $f_{\text{odd}} > f_{\text{even}2}$ , while the relationship of  $f_{\text{even}2}$  and  $f_{\text{odd}}$  could not be determined since it is related to  $L_{m3}$ . Small  $L_{m3}$  results in  $f_{\text{even}2} > f_{\text{odd}}$  while large  $L_{m3}$  results in  $f_{\text{even}2} < f_{\text{odd}}$ . Moreover, it can be observed that  $L_{m3}$  only affects  $f_{\text{even}2}$  without affecting  $f_{\text{even}1}$  and  $f_{\text{odd}}$ .  $L_{m2}$  affects both  $f_{\text{even}2}$  and  $f_{\text{even}1}$  without affecting  $f_{\text{odd}}$ . Thus, the trimode can be controlled individually. To demonstrate this, some simulations are carried out by using ADS. In the simulations, the parameters are chosen as follows:  $L_{m1} = 13.3$  mm,  $L_{m2} = 8$  mm,  $L_{m3} = 6$  mm,  $Y_{m1} = Y_{m2} = Y_{m3} = 0.01$  S, and  $\epsilon_r = 3.38$ . When one parameter is swept, the other parameters are fixed. The simulated results are shown in Figure 2. It can be observed that when  $L_{m2}$  is changed,  $f_{\text{even}1}$  and  $f_{\text{even}2}$  are also changed while  $f_{\text{odd}}$  is fixed. When  $L_{m3}$  is changed, only  $f_{\text{even}2}$  is changed and the other two modes are fixed. Thus, we can design a dual-band filter with tunable lower passband which is formed by  $f_{\text{even}2}$  (the second mode) and fixed upper passband formed by  $f_{\text{odd}}$  (the highest mode) and suppressed  $f_{\text{even}1}$  (the lowest mode).

Figure 3 shows the structure of the proposed dual-band filter with tunable lower passband. It utilizes a second order stub-loaded trimode resonator and the stubs are folded to reduce the size. The varactors are loaded at the center stubs. The capacitor  $C_1$  (2 pF) is used to block the DC signals. The  $R_1$  with the high resistance of 47 k $\Omega$  can prevent the RF signals and is used as DC feed. The feed lines are coupled with the resonators. There is an important issue that should be noticed: the feed line should be mirror symmetrical with respect to the port and the center of the resonator. With such a structure, the mode of  $f_{\text{even}1}$  can be suppressed and the tunable lower passband and fixed upper passband can be realized.

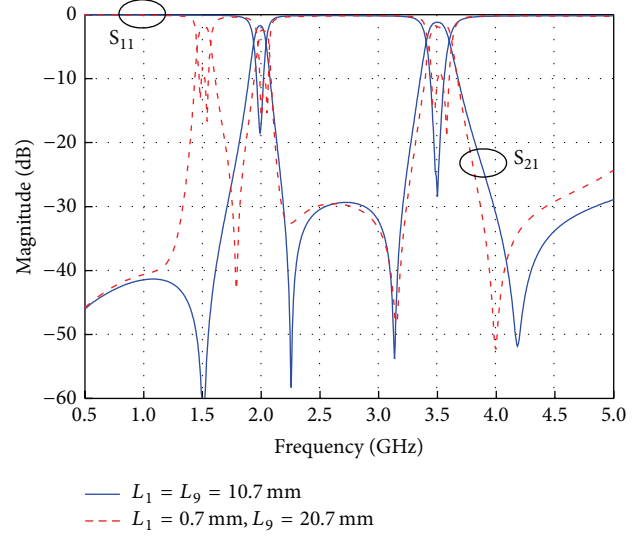
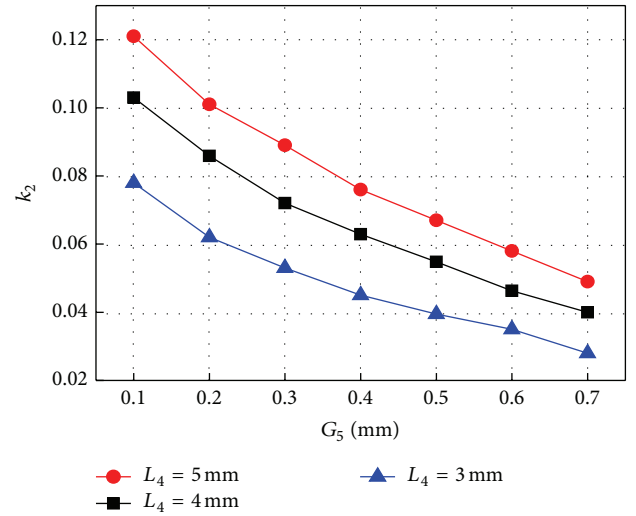


FIGURE 4: Simulated results under the condition of symmetric and asymmetric port position.

FIGURE 5:  $k_2$  against  $G_5$  and  $L_4$ .

The mechanism of  $f_{\text{even}1}$  suppression is addressed as follows. For a parallel coupled microstrip line with a length of  $d$ , the electric coupling can be approximated as [17]

$$k_e = p \times \frac{\int_{-d/2}^{d/2} V_1(x) V_2(x) dx}{\sqrt{\int_{-d/2}^{d/2} |V_1(x)|^2 dx \times \int_{-d/2}^{d/2} |V_2(x)|^2 dx}}, \quad (2)$$

where  $V_1(x)$  and  $V_2(x)$  are voltage-wave functions on the two lines and  $p$  represents a constant. When the voltage-wave function is odd on one line and even on the other, the integrand in the numerator is an odd function and it yields a zero value upon integration, which implies that the electric coupling coefficient is zero. Similarly, the magnetic coupling coefficient is also zero. Thus, no energy can pass at this frequency, resulting in mode suppression.

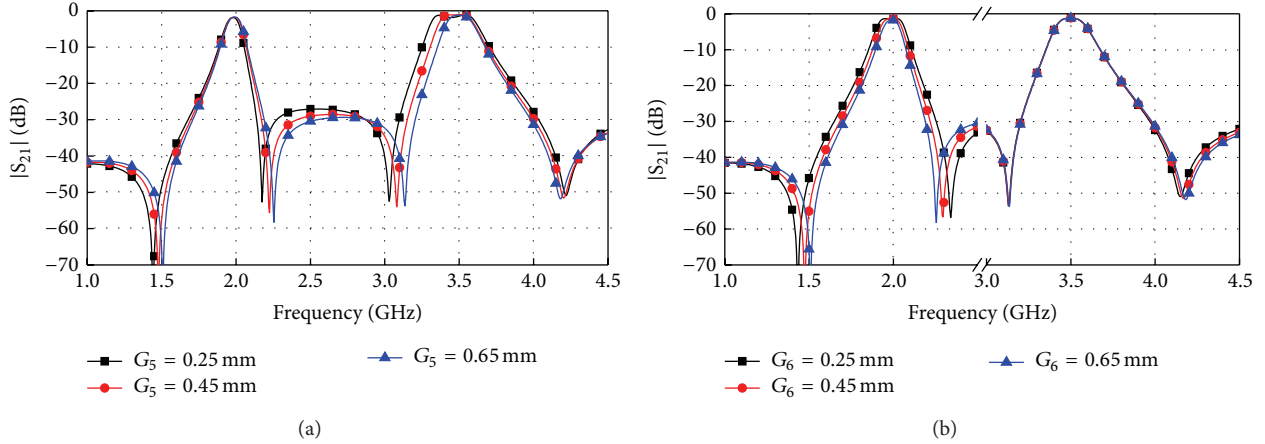


FIGURE 6: Simulated  $|S_{21}|$  against (a)  $G_5$ ; (b)  $G_6$  (the varactors are deleted and replaced by capacitors with value of 3 pF).

According to the analysis,  $f_{\text{even}1}$  is determined by  $L_{m1}$  and  $L_{m2}$ . In Figure 3, if the mode is not suppressed, it corresponds to a passband which is affected by  $2(L_5 + L_6 + L_8) + W_4$ . It is a half-wavelength resonator and the voltage distribution at the two open ends (AB and CD) with regard to the feed point is odd symmetrical. However, the voltage distribution at the two sides of feed line with regard to the feed point is even symmetrical. Thus, according to (2), the mode of  $f_{\text{even}1}$  is suppressed without affecting  $f_{\text{even}2}$  and  $f_{\text{odd}}$ . In the suppression mechanism, the key point is the mirror symmetry of the resonator and the feed line with regard to the feed point. To demonstrate this, simulations are carried out under the condition of the port at and not at the center of the feed line. To observe the modes, the varactors are replaced by capacitors. Figure 4 shows the simulated results. It can be observed that when the port is not located at the center of the feed line there will be three passbands, corresponding to the mode:  $f_{\text{even}1}$ ,  $f_{\text{even}2}$  and  $f_{\text{odd}}$ . If the port is located at the center of the feed line, the first passband will be suppressed and the other two bands are kept unchanged. Moreover, the selectivity of the lower passband is improved. Using such a feed method, the  $f_{\text{even}1}$  can be suppressed without any extra circuit.

To design a tunable dual-band bandpass filter, we can first design a dual-band filter with fixed centre frequencies of  $f_1$  and  $f_2$ . The frequencies and bandwidths can be individually controlled as follows. For the operating frequencies, it can be controlled individually. We can first obtain  $f_2$  by tuning the length of  $L_5 + L_8$ , which is nearly quarter-wavelength at  $f_2$ . Then,  $L_6$  and  $L_7$  are used to control  $f_1$  without affecting  $f_2$ . For the bandwidth, it is determined by the external quality factor ( $Q_e$ ) and coupling coefficient ( $k$ ). For the  $Q_e$ , it is determined by the coupling lengths and gaps, for example,  $L_1$ ,  $L_2$ ,  $G_1$ , and  $G_2$ . Small gaps ( $G_1$  and  $G_2$ ) and large lengths ( $L_1$  and  $L_2$ ) result in small  $Q_e$  and large bandwidths at both passbands. For  $k$ , it is determined by the coupling strength between the two resonators, for example,  $G_5$  and  $G_6$ . Since  $L_6$  has little effect on  $f_2$ ,  $G_6$  can be used to control  $k$  at  $f_1$  with little effect on  $f_2$ . To determine the initial value of these parameters, we can use simulation software to extract  $k_2$ .

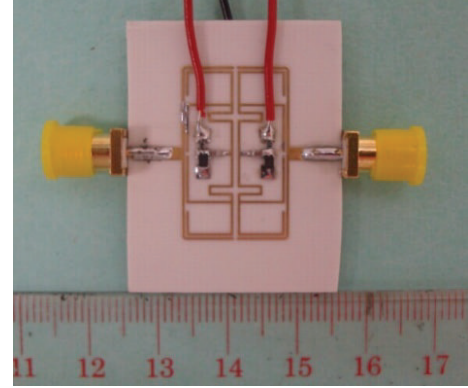
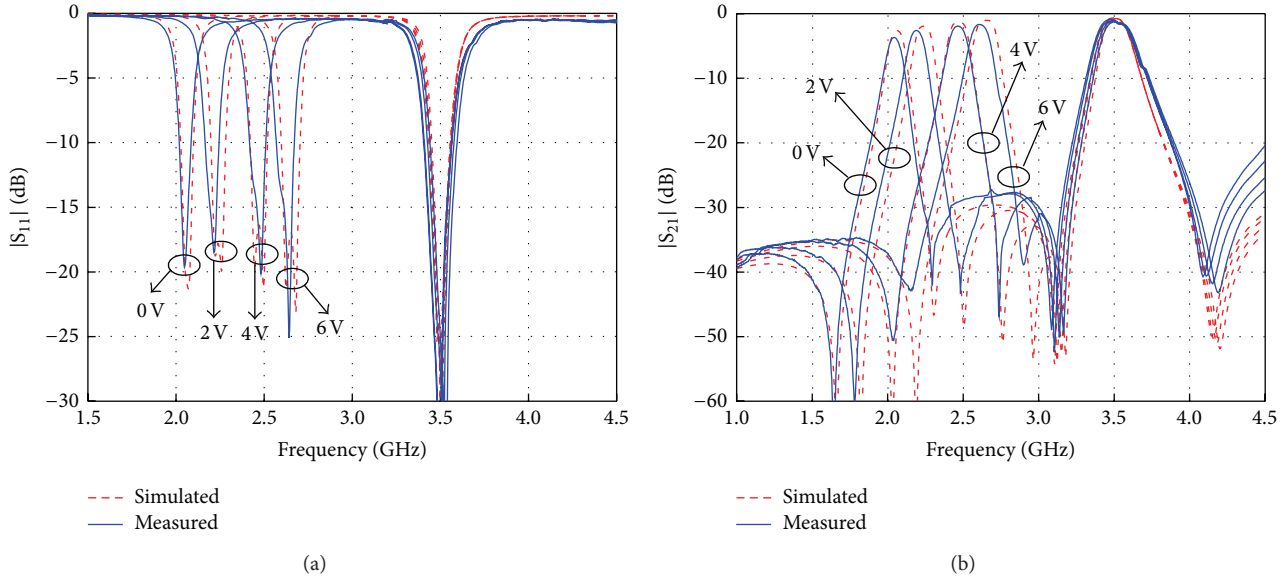


FIGURE 7: Photograph of the fabricated circuit.

The second passband is fixed with 3 dB bandwidth of 6% and 0.5 dB ripple. Thus, the required  $k_2$  is 0.06. Figure 5 shows the extracted  $k_2$  against  $G_5$  and  $L_4$ . Using this figure, the  $G_5$  and  $L_4$  can be determined as 0.2 and 3 mm. Similarly, the initial value of  $G_6$  can be determined as 0.3 mm. Figure 6 shows the simulated results against  $G_5$  and  $G_6$ . It can be observed that when  $G_5$  increases, the bandwidth of upper passband decreases and the bandwidth of the lower passband decreases. When  $G_6$  is changed, only the bandwidth of lower passband changes and the upper passband is fixed. These results indicate that the bandwidth of the two bands can be controlled individually. After the nontunable filter is well-designed, varactors are loaded at the end of  $L_7$  to realize tunable responses. Then, fine tuning is used to obtain the optimal performance.

### 3. Experiment

To demonstrate the proposed idea, a circuit is implemented on the substrate with a relative dielectric constant of 3.38, loss tangent of 0.0027, and thickness of 0.81 mm. The varactors employed in this design are 1sv277 from Toshiba. The capacitors are from Murata and we use the Murata model

FIGURE 8: Simulated and measured results (a)  $S_{11}$  and (b)  $S_{21}$ .

in simulation. The final values are selected as follows (all in mm):  $L_1 = 10.7$ ,  $L_2 = 6.9$ ,  $L_3 = 2.5$ ,  $L_4 = 4$ ,  $L_5 = 6.5$ ,  $L_6 = 11.4$ ,  $L_7 = 1.9$ ,  $L_8 = 5.7$ ,  $L_9 = 10.7$ ,  $W_1 = 1.86$ ,  $W_2 = W_3 = W_4 = 0.4$ ,  $G_1 = 0.2$ ,  $G_2 = 1$ ,  $G_3 = 0.2$ ,  $G_4 = 0.3$ ,  $G_5 = 0.65$ , and  $G_6 = 0.65$ . And  $R_1 = 47 \text{ k}\Omega$ ;  $C_1 = 2 \text{ pF}$ . The overall size of the filter is  $14.9 \text{ mm} \times 24 \text{ mm}$  or  $0.16\lambda_g \times 0.27\lambda_g$ , where  $\lambda_g$  represents the guided wavelength at 2.04 GHz, which is the lowest frequency of the tunable passband. The photograph of the fabricated filter is shown in Figure 7.

The simulation and measurement are accomplished by IE3D, ADS, and 8753ES network analyzer, respectively. Figure 8 shows the simulated and measured results. The upper passband is fixed at 3.5 GHz with 3 dB bandwidth of 200 MHz or 5.7%, which covers the WiMAX system. The measured minimum insertion loss is 1.5 dB and the return loss is better than 30 dB. Two transmission zeros with the frequencies of 3.15 and 4.25 GHz are generated at both sides of the passband. For the lower passband, with the voltage increasing from 0 to 6 V, the operating frequency changes from 2.04 to 2.62 GHz with 3 dB bandwidth changing from 90 to 135 MHz. The return losses are better than 15 dB in each state. The insertion losses change from 3.7 dB to 1.7 dB, which is a little higher than the nontunable bandpass filter. It is mainly due to the loss of the varactors. Meanwhile, the two transmission zeros located at the two sides of the lower passbands synchronously change with the passband, ensuring high selectivity. Among the four transmission zeros, the first one is generated by the source-load coupling; the second and last ones are generated by the stub with length of  $L_{m3}$  and  $L_{m1}$ . The third one is introduced by the feed line and  $L_1 + L_2$  is quarter-wavelength at the frequency of the third transmission zero.

## 4. Conclusion

This paper has presented a novel method for designing dual-band bandpass filters with a tunable lower passband and fixed upper passband. Both theory and experiments have been provided, showing that the filter exhibits good performance. Transmission zeros are generated near the passbands, resulting in high selectivity.

## Conflict of Interests

The authors declare that there is no conflict of interests regarding the publication of this paper.

## Acknowledgments

This work is supported by the NSFC under Grant 61271209 and the Fundamental Research Funds for the Central Universities under Grant 2013ZM0106.

## References

- [1] Y.-L. Lu, S. Wang, T. Gu, P. Cao, and K. Li, "A miniaturize bandpass filter with harmonic suppression using meandered quarter-wavelength resonators," *International Journal of Antennas and Propagation*, vol. 2014, Article ID 916927, 6 pages, 2014.
- [2] L. Gao and X. Y. Zhang, "High-selectivity dual-band bandpass filter using a quad-mode resonator with source-load coupling," *IEEE Microwave and Wireless Components Letters*, vol. 23, no. 9, pp. 474–476, 2013.
- [3] F.-C. Chen, Q.-X. Chu, and Z.-H. Tu, "Tri-band bandpass filter using stub-loaded resonators," *Electronics Letters*, vol. 44, no. 12, pp. 747–749, 2008.

- [4] Y. Liu, W. B. Dou, and Y. J. Zhao, "A tri-band bandpass filter realized using tri-mode T-shape branches," *Progress in Electromagnetics Research*, vol. 105, pp. 425–444, 2010.
- [5] H. Chen, "High isolation tri-band BPF using tri-mode resonator," *Microwave and Optical Technology Letters*, vol. 55, no. 6, pp. 1367–1370, 2013.
- [6] C. Ge and X.-W. Zhu, "High-selective tunable bandpass filter with two-path mixed coupling," *IEEE Microwave and Wireless Components Letters*, vol. 24, no. 7, pp. 451–453, 2014.
- [7] X.-G. Huang, Q.-Y. Feng, Q.-Y. Xiang, and D.-H. Jia, "Constant absolute bandwidth tunable filter using varactor-loaded open-loop resonators," *Microwave and Optical Technology Letters*, vol. 56, no. 5, pp. 1178–1181, 2014.
- [8] Y.-Y. Wang, F. Wei, B. Liu, H. Xu, and X.-W. Shi, "A tunable bandpass filter with constant absolute bandwidth based on one ring resonator," *Journal of Electromagnetic Waves and Applications*, vol. 26, no. 11-12, pp. 1587–1593, 2012.
- [9] B. Liu, F. Wei, H. Zhang, X. Shi, and H. Lin, "A tunable bandpass filter with switchable bandwidth," *Journal of Electromagnetic Waves and Applications*, vol. 25, no. 2-3, pp. 223–232, 2011.
- [10] L. Gao, X. Y. Zhang, B.-J. Hu, and Q. Xue, "Novel multi-stub loaded resonators and their applications to various bandpass filters," *IEEE Transactions on Microwave Theory and Techniques*, vol. 62, no. 5, pp. 1162–1172, 2014.
- [11] X. Y. Zhang and Q. Xue, "Novel centrally loaded resonators and their applications to bandpass filters," *IEEE Transactions on Microwave Theory and Techniques*, vol. 56, no. 4, pp. 913–921, 2008.
- [12] L. Zhang, X.-H. Wang, Z.-D. Wang, Y.-F. Bai, and X.-W. Shi, "Compact electronically tunable microstrip dual-band filter using stub-loaded SIRs," *Journal of Electromagnetic Waves and Applications*, vol. 28, no. 1, pp. 39–48, 2014.
- [13] X. Huang, L. Zhu, Q. Feng, Q. Xiang, and D. Jia, "Tunable bandpass filter with independently controllable dual passbands," *IEEE Transactions on Microwave Theory and Techniques*, vol. 61, no. 9, pp. 3200–3208, 2013.
- [14] G. Chaudhary, Y. Jeong, and J. Lim, "Dual-band bandpass filter with independently tunable center frequencies and bandwidths," *IEEE Transactions on Microwave Theory and Techniques*, vol. 61, no. 1, pp. 107–116, 2013.
- [15] X. Y. Zhang, L. Gao, Y. Cao, X.-L. Zhao, and Y. Ding, "Independently-tuned dual-band filter using varactor-loaded resonators," *Progress In Electromagnetics Research C*, vol. 42, pp. 55–66, 2013.
- [16] B. You, L. Chen, Y. Liang, and X. Wen, "A high-selectivity tunable dual-band bandpass filter using stub-loaded stepped-impedance resonators," *IEEE Microwave and Wireless Components Letters*, vol. 24, no. 11, pp. 736–738, 2014.
- [17] X. Y. Zhang and Q. Xue, "Harmonic-suppressed bandpass filter based on discriminating coupling," *IEEE Microwave and Wireless Components Letters*, vol. 19, no. 11, pp. 695–697, 2009.

## Research Article

# Map-Based Channel Model for Urban Macrocell Propagation Scenarios

**Jose F. Monserrat, Saúl Inca, Jordi Calabuig, and David Martín-Sacristán**

*iTEAM Research Institute, Universitat Politècnica de València, C/Camino de Vera S/N, Edificio 8G, 46022 Valencia, Spain*

Correspondence should be addressed to Jose F. Monserrat; [jomondel@iteam.upv.es](mailto:jomondel@iteam.upv.es)

Received 3 November 2014; Accepted 17 April 2015

Academic Editor: Cheng Jin

Copyright © 2015 Jose F. Monserrat et al. This is an open access article distributed under the Creative Commons Attribution License, which permits unrestricted use, distribution, and reproduction in any medium, provided the original work is properly cited.

The evolution of LTE towards 5G has started and different research projects and institutions are in the process of verifying new technology components through simulations. Coordination between groups is strongly recommended and, in this sense, a common definition of test cases and simulation models is needed. The scope of this paper is to present a realistic channel model for urban macrocell scenarios. This model is map-based and takes into account the layout of buildings situated in the area under study. A detailed description of the model is given together with a comparison with other widely used channel models. The benchmark includes a measurement campaign in which the proposed model is shown to be much closer to the actual behavior of a cellular system. Particular attention is given to the outdoor component of the model, since it is here where the proposed approach is showing main difference with other previous models.

## 1. Introduction

The research community is currently developing the fifth generation of mobile communication systems (5G). From early 2012, ITU-R set up a research programme to address “IMT for 2020 and beyond.” In this framework, detailed investigations of the key elements of 5G are on track from several stakeholders in the 5G community. Of special relevance is the contribution from the European Union METIS project [1]. Several technology components have been proposed, all of them being verified through extensive simulations. In this regard, it is important to highlight the need to use realistic (no synthetic) scenarios. Past experience with other study works performed in 3GPP has shown the need for a proper characterization of realistic effects. Some conclusions reached with synthetic simulations have turned out to be incorrect once the proposed techniques were applied to the field. In this sense, METIS definition of the 5G concept is driven by a set of twelve realistic test cases [2] and the same approach towards realistic channel models can be seen in the 3GPP simulation activities.

In the evaluation of the 5G technology component candidates, channel models are of paramount importance to

guarantee an accurate modeling of the propagation conditions. The ITU-R defined in [3] a channel model that can be parameterized to cover a different set of test environments, ranging from indoor to rural cases. The main features of this model are quite similar to the Extended Spatial Channel Model (SCME) defined by the WINNER project [4] and also described by the 3GPP [5]. Given the complexity of the small scale model, ITU-R also specified in [3] an alternative method based on the usage of a correlation matrix, derived as the Kronecker product of the polarization covariance matrix and the correlation matrices calculated at the base stations and at the user equipment, which is also suggested by 3GPP for the conformance specification of user equipment [6].

All these widely used models lack the incorporation of a 3D characterization of the scenario layout, which is a must for the future evaluation of cellular systems [7]. New map-based models considering the location of streets and buildings must be developed in order to take the elevation dimension and the resulting changes in radio propagation into account.

Recently, 3GPP issued a 3D channel model that mainly focuses on the extensions of the small scale modeling [8]. Concerning path loss characterization, the proposed model is very similar but includes calculation of distances in 3D

and also an extension for the outdoor-to-indoor propagation modeling. This 3D model is nowadays being used in the evolution of LTE, most specially in the analysis of dense deployments.

Another alternative to make an adequate characterization of propagation effects is the use of ray tracing [9]. Ray tracing approximates the propagation launching a set of discrete rays to different directions and their propagation is traced by computing the interactions of rays (like reflection, diffraction, or dispersion), with the surrounding objects alongside the propagation in the environment. Although ray tracing is very accurate it needs a complete knowledge of the environment and its computational burden is unmanageable for large deployment scenarios.

In large and complex deployment scenarios, new alternatives for 3D modeling should be studied keeping in mind the tradeoff between realism and implementation complexity. This paper proposes a propagation modeling alternative for urban macrocell scenarios that, being much simpler than ray tracing, still allows for a proper characterization of real environments. As compared with ray tracing, the proposed model is equivalent to a single-ray approach, provided that the total loss is computed as a summation of three terms representing free space loss, the diffraction loss from rooftop to the street, and the reduction due to multiple screen diffraction past rows of buildings. Section 2 presents the model, including small and large scale effects. Section 3 compares this model with 3GPP and ITU-R widely used alternatives and, finally, Section 4 concludes the paper.

## 2. The Proposed Model

This scenario refers to the situation in which the base station is situated over a building rooftop and has dominant visibility of users. For the urban macrocell scenario, most part of the signal reaches users via diffraction and main propagation path is over buildings [10]. This propagation scenario is similar to the scenario assumed by ETSI in [11] and the same approaches apply. This model is divided into two parts, the small scale and the large scale characterization.

Channel models usually use two different sets of channel parameters. The first one is related to the large scale parameters, such as shadow fading and path loss. The second one concerns small scale parameters, including Angle of Arrival (AoA) and Angle of Departure (AoD) or delay of the rays.

In order to generate channel samples between one transmitter and one receiver, mobility and exact location of both ends must be known. Based on this information all large scale parameters are generated, followed by the small scale parameters.

**2.1. Small Scale Parameters.** Concerning small scale parameters characterization, we propose the use of ITU-R M.2135 UMa model [3], although three issues must be clarified. Firstly, it is worth noting that ITU-R M.2135 UMa is a 2D model not a 3D model as could be desirable. However, it has proven valid for conventional MIMO structures. Secondly, regarding the validity of such model for dynamic simulations in which the position of users changes over time, we propose,

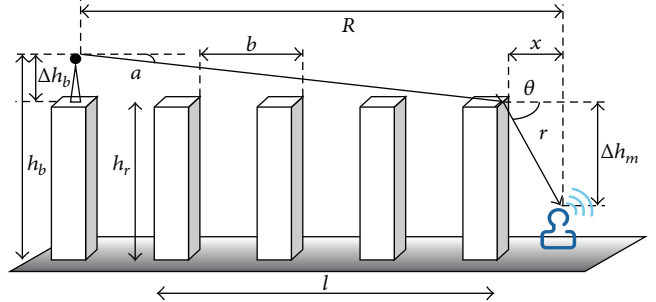


FIGURE 1: Geometry of the large scale model.

assuming that the conditions for rays and cluster generation remain static along a certain correlation length, 50 meters for the urban macrocell propagation scenario. After this distance, new cluster and rays must be generated according to the new geometry. Finally, in [3] these models are particularized for LoS or NLoS conditions. For synthetic simulations these conditions are randomly selected. However, for realistic test cases sight condition will be reevaluated for each correlation length based on the actual position of transmitter and receiver.

**2.2. Large Scale Modeling.** The total transmission loss in decibels is expressed as the sum of free space loss, the diffraction loss from rooftop to the street, and the reduction due to multiple screen diffraction past rows of buildings; that is,

$$L(R) = \begin{cases} L_{fs} + L_{rts} + L_{msd} & \text{if } L_{rts} + L_{msd} > 0 \\ L_{fs} & \text{if } L_{rts} + L_{msd} \leq 0. \end{cases} \quad (1)$$

Figure 1 illustrates the used geometry and the set of variables that modify the model response.

Given a mobile-to-base separation  $R$ , the free space loss between them is given by

$$L_{fs} = -10 \cdot \log_{10} \left( \frac{\lambda}{4\pi R} \right)^2. \quad (2)$$

The diffraction from the rooftop down to the street level gives the excess loss to the mobile station [12]:

$$L_{rts} = -20 \cdot \log_{10} \left[ \frac{1}{2} - \frac{1}{\pi} \arctan \left( \operatorname{sign}(\theta) \sqrt{\frac{\pi^3}{4\lambda} r (1 - \cos \theta)} \right) \right], \quad (3)$$

where, according to Figure 1,

$$\theta = \tan^{-1} \left( \frac{|\Delta h_m|}{x} \right) \quad (4)$$

$$r = \sqrt{(\Delta h_m)^2 + x^2},$$

being  $\Delta h_m$  the difference between the last building height and the mobile antenna height and  $x$  the horizontal distance between the mobile and the diffracting edges.

The multiple screen diffraction loss from the base antennas due to propagation past rows of buildings depends on the base antennas height relative to the building heights and on the incidence angle [13]. A criterion for grazing incidence is the settled field distance,  $d_s$ :

$$d_s = \frac{\lambda R^2}{\Delta h_b^2}, \quad (5)$$

where  $\Delta h_b$  is the base station antenna height,  $h_b$ , relative to average rooftop  $h_r$ . Then for the calculation of  $L_{msd}$ ,  $d_s$  is compared to the length of the path covered by buildings  $l$ .

If  $l > d_s$ ,

$$L_{msd} = L_{bsh} + k_a + k_d \log_{10} \left( \frac{R}{1000} \right) + k_f \log_{10} (f) - 9 \log_{10} (b), \quad (6)$$

where

$$L_{bsh} = \begin{cases} -18 \log_{10} (1 + \Delta h_b) & \text{for } h_b > h_r \\ 0 & \text{for } h_b \leq h_r \end{cases} \quad (7)$$

is a loss term that depends on the base station height:

$$k_a = \begin{cases} 54 & \text{for } h_b > h_r \\ 54 - 0.8 \Delta h_b & \text{for } h_b \leq h_r, R \geq 500 \\ 54 - 1.6 \Delta h_b \frac{R}{1000} & \text{for } h_b \leq h_r, R < 500, \end{cases} \quad (8)$$

$$k_d = \begin{cases} 18 & \text{for } h_b > h_r \\ 18 - 15 \frac{\Delta h_b}{h_r} & \text{for } h_b \leq h_r, \end{cases}$$

and  $k_f = 0.7(f/925 - 1)$  for medium sized cities and suburban centers with medium tree density whereas  $k_f = 15(f/925 - 1)$  is for metropolitan centers. Note that frequency is expressed in MHz in these equations.

On the other hand if  $l \leq d_s$ , a further distinction has to be made according to the relative heights of the base station and the rooftops:

$$L_{msd} = -10 \cdot \log_{10} (Q_M^2), \quad (9)$$

where

$$Q_M = \begin{cases} 2.35 \left( \frac{\Delta h_b}{R} \sqrt{\frac{b}{\lambda}} \right)^{0.9} & \text{for } h_b > h_r \\ \frac{b}{R} & \text{for } h_b \approx h_r \\ \frac{b}{2\pi R} \sqrt{\frac{\lambda}{\rho}} \left( \frac{1}{\theta} - \frac{1}{2\pi + \theta} \right) & \text{for } h_b < h_r, \end{cases} \quad (10)$$

$$\theta = \tan^{-1} \left( \frac{\Delta h_b}{b} \right),$$

$$\rho = \sqrt{\Delta h_b^2 + b^2}.$$



FIGURE 2: Map of the site in Valencia, including the location and azimuth of the cell under study.

In this model, minimum coupling loss is set to 70 dB.

Concerning outdoor-to-indoor characterization, we propose the same approach as in the WINNER+ project [14]. Note also that a complete Matlab implementation of the model can be found at the METIS webpage [15].

### 3. Comparison with Other Models

The comparison between the three alternatives considered in this paper, that is, the IMT-A model, the 3GPP model with 3D extension, and the proposed model, referred to as map-based model, was made using real measurement. These measurements were carried out in the urban area of Valencia, Spain. The transmit antenna was a real UMTS base station located in the city operating at 2100 MHz. The base station was located above rooftop at 37 m. The equipment used for the measurements was a drive-test terminal equipped with the software Nemo-Outdoor. Receive Signal Code Power (RSCP) measurements were taken on a uniform grid of outdoor static positions. Measured points were spaced 10 meters, half the typical correlation distance in an urban scenario, storing 60 samples during 30 consecutive seconds (data was captured every 0.5 seconds). This measurement time was 1000 times the coherence time of a Rayleigh-Fading Channel corresponding to a low mobility or pedestrian user moving at 3 km/h, so that the average of the samples could be considered independent of the fast fading.

With these resulting levels of RSCP, we obtained the approximate values of the path loss at each point taking into account the transmit power of the base station, the gain of the mobile terminal, and the gain of the base station antenna for each point by calculating the approximate values for azimuth and elevation and the exact antenna pattern.

Figure 2 shows the area where measurements were taken. It includes an irregular pattern of buildings with different heights, sidewalks, parking lots, and also a garden area. We chose this location because of its heterogeneity, far away from the classical regular Manhattan grid assumed in other scenarios.

Once the area under study has been identified, a proper clutter height must be created. This is simply a matrix in which each cell identifies the exact height of the corresponding coordinate with respect to the ground. Figure 3 shows an example of such a clutter height with 10 m resolution.

The clutter height is used in the model proposed in this paper to create the propagation profile between transmitter

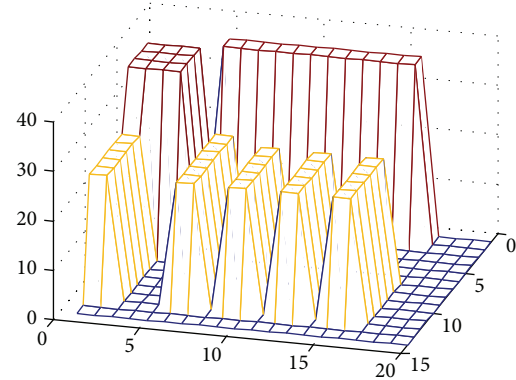


FIGURE 3: Map model used for the channel prediction.

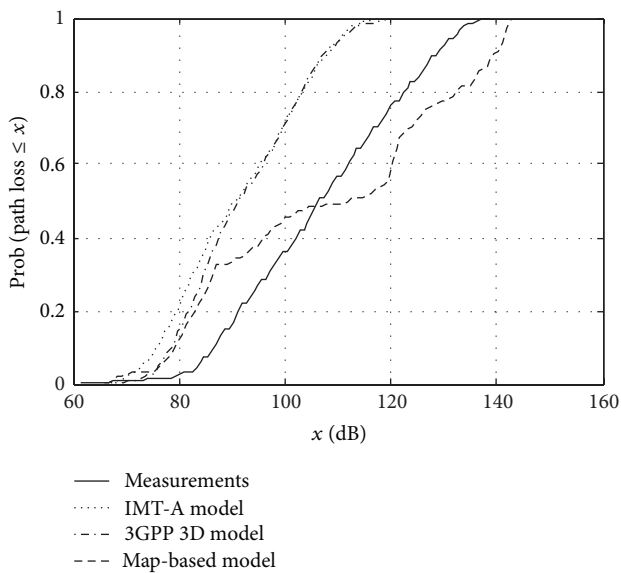


FIGURE 4: CDF of the path loss values in the area under study.

and receiver and calculate the exact values of the variables represented in Figure 1. However, in order to improve the level of realism of the other two models compared in this section, this map was also used in the IMT-A and 3GPP models. Unlike their current stochastic approach for determining LoS/NLoS conditions, we propose to derive the LoS or NLoS conditions directly from the visibility of transmitter and receivers using this 3D modeling of the area under study.

Figure 4 shows the Cumulative Distribution Function (CDF) of the path loss predictions provided by the three models compared in this paper and the actual path loss in the area. We can see the high similarity between the IMT-A and the 3GPP 3D models. They slightly differ in the lowest values of path loss, that is, with LoS, but are similar for high path losses.

Concerning the map-based model, it is worth mentioning that this is very similar to the 3GPP 3D and IMT-A model in case of LoS, that is, for the lowest range of path loss values, but differs considerably for higher values. In fact, in the median the map-based model predicts a path loss 20.5 dB

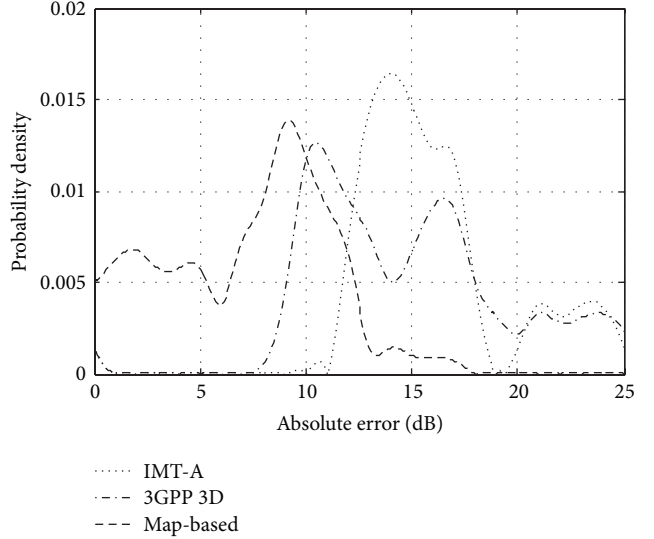


FIGURE 5: Probability distribution of the absolute error in the path loss estimation.

greater than the IMT-A and 3GPP 3D models. However, when comparing with the real measurements, the distance in the median of the map-based model and the real measurements is only 4.7 dB, being this difference 15.84 dB when comparing the other two models with the actual data. With LoS, all of them are optimistic with respect to the actual behavior of the propagation probably due to the presence of trees.

Figure 5 shows the probability distribution of the absolute error of the predictions for the three models under study. Again, the map-based model features lower error as compared with the other two models. In fact, the error of the map-based model as compared with the real measurements is always lower than 18 dB, being the average of only 7.21 dB. The IMT-A model is the one showing a higher prediction error, being the average absolute error of 15.85 dB. Moreover, the minimum error is around 10 dB. Finally, the 3GPP 3D model is between the other two, although the average absolute error is also very high, of 14.75 dB.

#### 4. Conclusion

In this paper, an outdoor model for urban macrocell propagation scenarios has been described. This model is map-based and uses clutter height data to perform path loss predictions. A comparison of this model and the IMT-A and 3GPP models based on real measurements shows that significant improvements can be achieved when considering the layout of buildings while keeping the simplicity in the calculations. Moreover, measurements show that the proposed model presents an average absolute error of 7.21 dB, whereas 3GPP and IMT-A models show an error of 14.75 and 15.85 dB, respectively.

#### Conflict of Interests

The authors declare that there is no conflict of interests regarding the publication of this paper.

## Acknowledgments

This work was performed in the framework of the FP7 project ICT-317669 METIS, which is partly funded by the European Union. The authors would like to acknowledge the contributions of their colleagues in METIS, although the views expressed are those of the authors and do not necessarily represent the project.

## References

- [1] METIS, "Mobile and wireless communications Enablers for the Twenty-twenty Information Society," EU 7th Framework Programme Project, <http://www.metis2020.com>.
- [2] A. Osseiran, F. Boccardi, V. Braun et al., "Scenarios for 5G mobile and wireless communications: the vision of the METIS project," *IEEE Communications Magazine*, vol. 52, no. 5, pp. 26–35, 2014.
- [3] ITU, "Guidelines for evaluation of radio interface technologies for IMT-Advanced," ITU-R M.2135, ITU Publications, 2008.
- [4] D. S. Baum, J. Hansen, and J. Salo, "An interim channel model for beyond-3G systems: extending the 3GPP spatial channel model (SCM)," in *Proceedings of the 61st IEEE Vehicular Technology Conference (VTC '05)*, vol. 5, pp. 3132–3136, IEEE, Stockholm, Sweden, May-June 2005.
- [5] Spatial Channel Model for MIMO Simulations, 3GPP TR 25.996, 2009.
- [6] User Equipment (UE) conformance specification Radio transmission and reception. Part 1: Conformance Testing, 3GPP TS 36.521-1, 2014.
- [7] 3GPP, "Scenarios for 3D-channel modeling," 3GPP TSG-RAN WG1 #72 R1-130567, 3GPP, 2013.
- [8] 3D-channel model for LTE, 3GPP TR 36.873, 2014.
- [9] C. Zhou and J. Waynert, "The equivalence of the ray tracing and modal methods for modeling radio propagation in lossy rectangular tunnels," *IEEE Antennas and Wireless Propagation Letters*, vol. 13, pp. 615–618, 2014.
- [10] L. Rubio, J. F. Monserrat, A. P. Garc&ia, and J. Reig, "Temporal dispersion characterization of over-building propagation applied to iso-frequency repeaters," *IEEE Antennas and Wireless Propagation Letters*, vol. 8, pp. 509–512, 2009.
- [11] UMTS: Selection Procedures for the Choice of Radio Transmission Technologies of the UMTS, UMTS 30.03 TR 101 112 v3.2.0, 1998.
- [12] J. Medbo and F. Harrysson, "Channel modeling for the stationary UE scenario," in *Proceedings of the 7th European Conference on Antennas and Propagation (EuCAP '13)*, pp. 2811–2815, April 2013.
- [13] Propagation data and prediction methods for the planning of short-range outdoor radiocommunication systems and radio local area networks in the frequency range 300 MHz to 100 GHz, ITU-R, P.1411, 1999.
- [14] P. Heino, *D5.3: WINNER+ Final Channel Models*, WINNER, 2010.
- [15] Software implementation (Matlab) of PS3 and PS4, <https://www.metis2020.com/documents/simulations/>.

## Research Article

# Dual Zeroth-Order Resonant USB Dongle Antennas for 4G MIMO Wireless Communications

**Yan Shi, Lu Zhang, and Chang-Hong Liang**

*School of Electronic Engineering, Xidian University, Xi'an, Shaanxi 710071, China*

Correspondence should be addressed to Yan Shi; shiyan@mail.xidian.edu.cn

Received 28 October 2014; Revised 24 March 2015; Accepted 24 March 2015

Academic Editor: Nima Chamanara

Copyright © 2015 Yan Shi et al. This is an open access article distributed under the Creative Commons Attribution License, which permits unrestricted use, distribution, and reproduction in any medium, provided the original work is properly cited.

A multiband multiple-input multiple-output (MIMO) antenna system consisting of two antenna elements has been proposed for 4G USB dongle application. The designed MIMO antenna system with a compact volume of  $25\text{ mm} \times 30\text{ mm} \times 3.5\text{ mm}$  operates in two zeroth-order resonance (ZOR) modes to cover the LTE band 13 (746–787 MHz), GSM850/900 (824–960 MHz), and LTE band 7 (2500–2690 MHz) simultaneously. A pair of L-shaped parasitic strips and an etching slot on the ground are employed to achieve good isolation between two elements. Measurement results show that proposed MIMO antenna system has total efficiency over 40% across the operation band and isolation less than  $-8\text{ dB}$  at the lower band and  $-16\text{ dB}$  at the upper band, respectively.

## 1. Introduction

To fulfill the requirement of 4G wireless communication, long-term evolution (LTE) has been proposed as a new standard to provide more flexible choice of frequency band and faster data transfer rate. Several LTE frequency bands have been introduced for better communication. Considering some new LTE frequency bands lower than ordinary 2G range, such as the LTE band 12 (698–746 MHz) and the LTE band 13 (747–787 MHz), the design of compact antenna for 4G USB dongle faces many huge challenges including larger electrical size of the antenna and stronger mutual coupling between different antennas.

Antenna based on composite right- and left-hand transmission line (CRLH-TL) theory has been developed as a promising technique due to its small size and better performance. Distinguished from the conventional structures, the zeroth-order resonance (ZOR) occurs in the CRLH-TL structure so that no phase variation exists along the structure at one particular frequency [1]. Therefore, antenna with this characteristic, namely, ZOR antenna, can achieve good performance without requiring the half-wavelength size. Moreover, antenna with the ZOR structure can obtain wider operation band [2].

As a core technology of LTE system, the MIMO technology has been of increasing interest because of its high

utilization of frequency spectrum and high channel capacity, to name a few. However, a major difficulty in implementing MIMO technology is to reduce strong mutual coupling between compactly packed antennas and achieve good performance at the same time. To simultaneously overcome the locating and isolation problems within a small space inside the USB dongle, various techniques have been proposed. Built-in decoupling and matching networks [3, 4] are one of common methods to reduce mutual coupling between antennas. Another technique is to employ a parasitic unit to generate additional mutual coupling to counteract the original one [5–8]. What is more, an etching slot on the ground is an effective method to reduce the surface wave coupling [9, 10]. Up to now, there have been lots of studies on designing miniaturized MIMO antennas on USB dongle platform [11–13]. In the MIMO antenna system of [12], two chip antennas for dual-band wireless LAN use are closely spaced. In [13], MIMO antenna system consisting of two symmetrical meander radiators has been developed to operate from 704 MHz to 746 MHz.

In this paper, a multiband MIMO antenna with a compact size of  $25\text{ mm} \times 12\text{ mm} \times 3.5\text{ mm}$  for 4G USB dongle has been proposed. The MIMO antenna system consists of two symmetrically antenna elements located at the top edge of the substrate to cover the LTE band 13 (746–787 MHz),

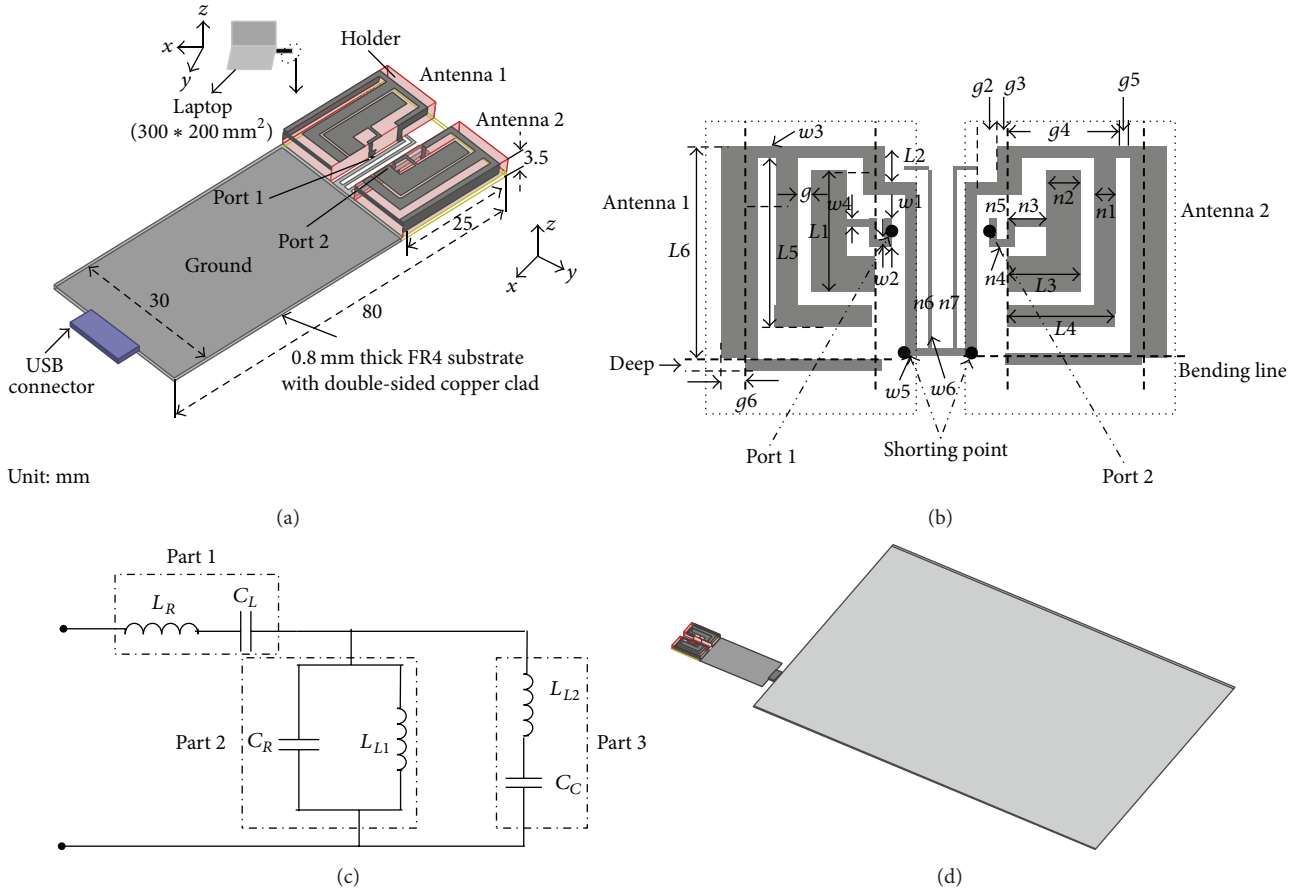


FIGURE 1: Geometry of the proposed multiband MIMO antenna system: (a) 3D view of the proposed MIMO antenna, (b) MIMO antenna and decoupling structure, (c) equivalent circuit of the unit antenna of the MIMO system, and (d) simulation model for the MIMO antenna system connected by the laptop.

GSM850/900 (824–960 MHz), and LTE 7 (2500–2600 MHz), simultaneously. A dual ZOR-based antenna is designed as the antenna element of the proposed MIMO system and thus a very wide operating frequency bandwidth is obtained. In addition, a pair of L-shaped parasitic strips and an etching slot on the ground are utilized to achieve good isolation. The measured results show that the isolation between two antennas is less than  $-8$  dB over the lower band and  $-16$  dB across the upper band, respectively. Total efficiency of antenna over 40% and omnidirectional radiation patterns are obtained across the operation bands.

## 2. Antenna Design

The MIMO system with a compact size of  $25 \text{ mm} \times 30 \text{ mm} \times 3.5 \text{ mm}$  is located at the top edge of the substrate. The FR4 substrate with  $\epsilon_r = 4.4$  is installed on the double-sided copper with a size of  $30 \text{ mm} \times 55 \text{ mm}$ . The system consists of two identical, symmetrical antenna elements which operate in the dual ZOR modes. The antenna is printed on a hollow plastic holder with a relative permittivity of  $\epsilon_r = 3.5$  and a wall thickness of 1.4 mm. A pair of L-shaped strips between two antenna elements and an etching slot on the ground

TABLE 1: Geometric parameters for the proposed MIMO antenna (unit: millimeters).

$g$	Deep	$w_4$	$w_1$	$w_2$	$w_3$	$w_5$	$w_6$	$n_1$
0.1	1	0.5	1.5	0.5	1	0.3	0.5	3
$n_2$	$n_3$	$n_4$	$n_5$	$n_6$	$n_7$	$L_1$	$L_2$	$L_3$
3.7	3	2.5	1	1.2	1	16.7	6	6.7
$L_4$	$L_5$	$L_6$	$g_2$	$g_3$	$g_4$	$g_5$	$g_6$	
9.8	17.8	23	2	1.5	11	1	2.5	

are introduced to obtain good isolation. Figures 1(a) and 1(b) show the geometry of the proposed MIMO antenna system, Figure 1(c) illustrates the equivalent circuit of the corresponding antenna element, and Figure 1(d) shows the simulation model for the MIMO antenna system connected by the laptop with the dimension of  $300 \text{ mm} \times 210 \text{ mm}$ . Detailed dimensions of the MIMO system are given in Table 1.

It can be seen from Figure 1 that the antenna element in the MIMO system can be divided into three parts: Part 1 comprises a monopole fed by a wound fine strip, a coupling strip, and the fine seam between them. This part can be equivalent

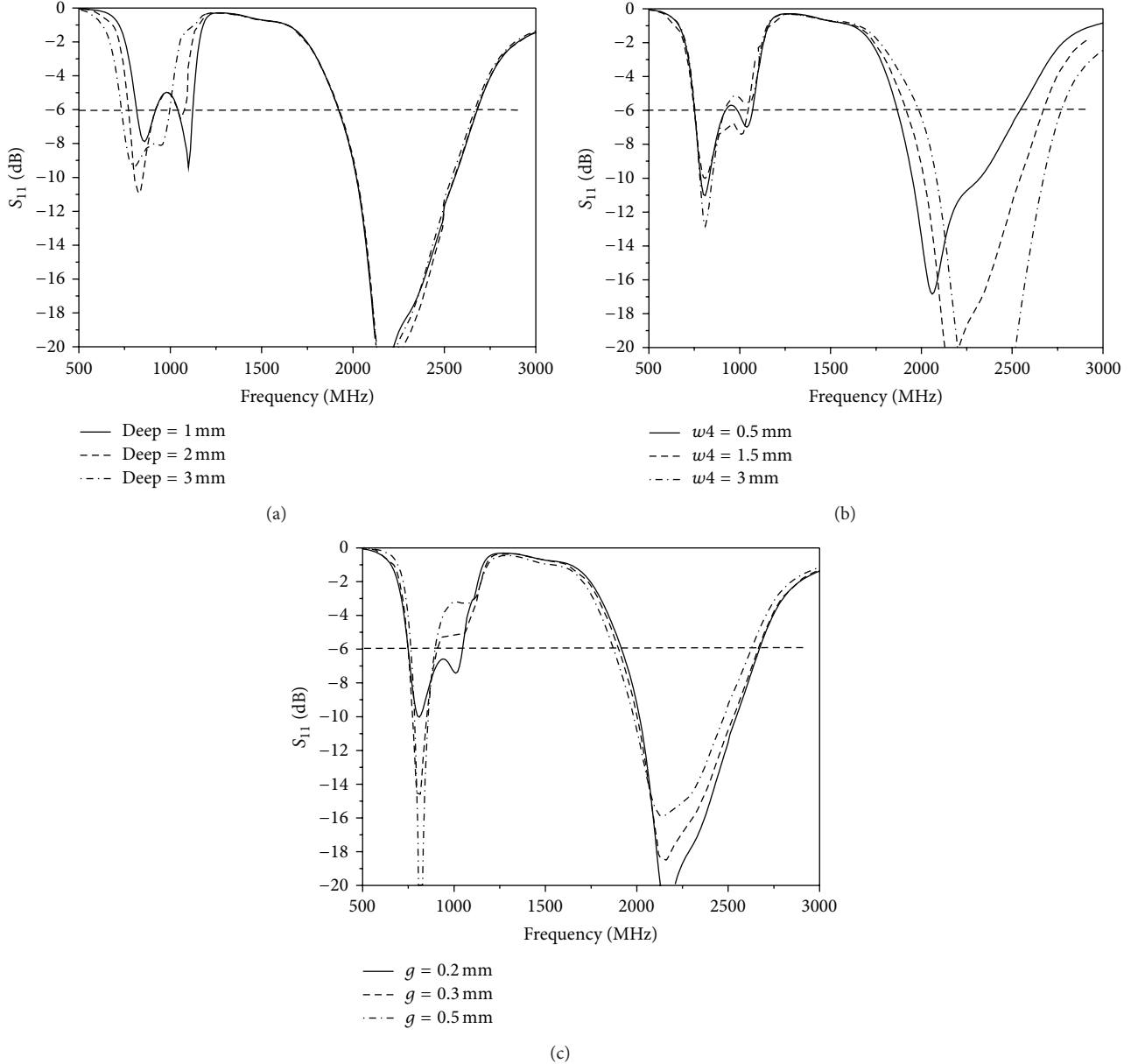


FIGURE 2: Variation of the return loss of the unit element of the proposed MIMO antenna with the increase of geometry parameters: (a) deep, (b)  $w_4$ , and (c)  $g$ .

to the series left-hand capacitance ( $C_L$ ) mainly produced by the coupling seam and right-hand inductance ( $L_R$ ) generated by the rest. Part 2 corresponding to the grounded strip can be equivalent to the shunt left-hand inductance ( $L_{L1}$ ) coming from the strip itself and right-hand capacitance ( $C_R$ ) mainly coming from the interaction between the strip and other portions. Furthermore, Part 3 refers to the open circuit strip which is in parallel with Part 2 and can be equivalent to series left-hand inductance ( $L_{L2}$ ) and the ground capacitance ( $C_C$ ). According to the CRLH-TL theory [1], the first ZOR mode is produced by Part 1 and Part 3, which operates efficiently at lower frequency band. Simultaneously, Part 1 and Part 2 generate the other ZOR mode to cover

the higher frequency band. The two ZOR modes interact with each other to obtain a wider operation band (746–960 MHz and 2500–2690 MHz). As shown in Figure 1(a), the USB dongle is inserted into a laptop for practical applications. Figure 2 shows the effect of three geometry parameters on the simulated return loss of the antenna element. It can be seen that parameters  $deep$  and  $w_4$  have a main effect on the lower band and the upper band, respectively, while parameter  $g$  influences the performance of the antenna across the whole operating frequency band. Figure 3 gives reflection coefficient and input impedance of the unit element of the proposed MIMO antenna. It can be seen from Figure 3(a) that the proposed unit element can operate at LTE band 13,

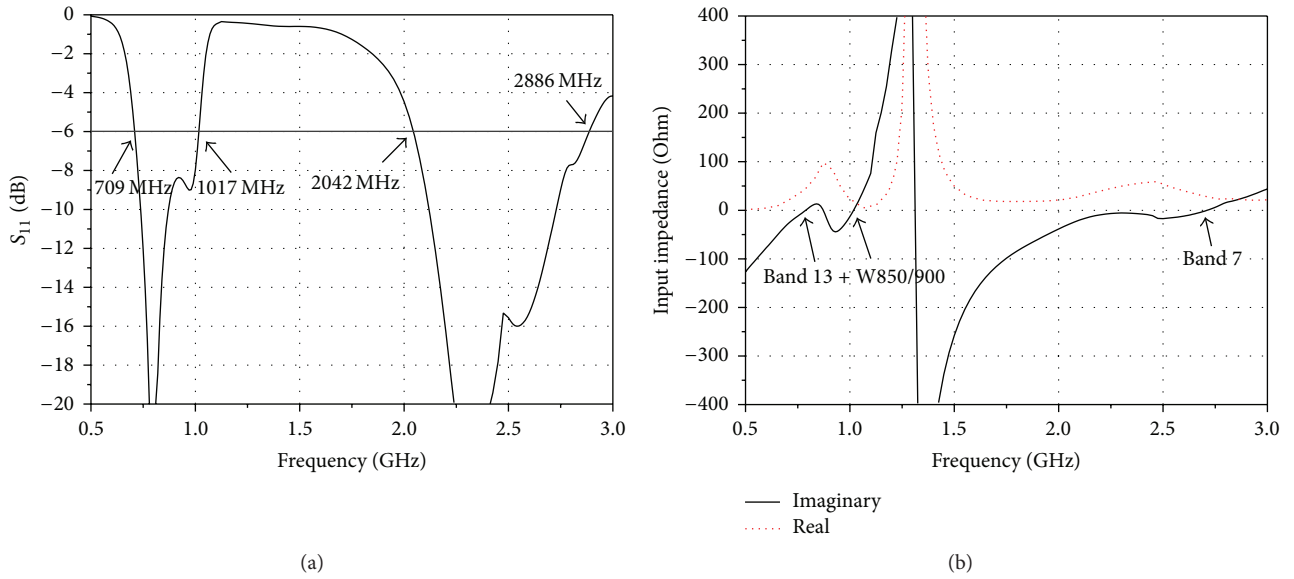


FIGURE 3: Performance of the unit element of the proposed MIMO antenna: (a) S parameter; (b) input impedance.

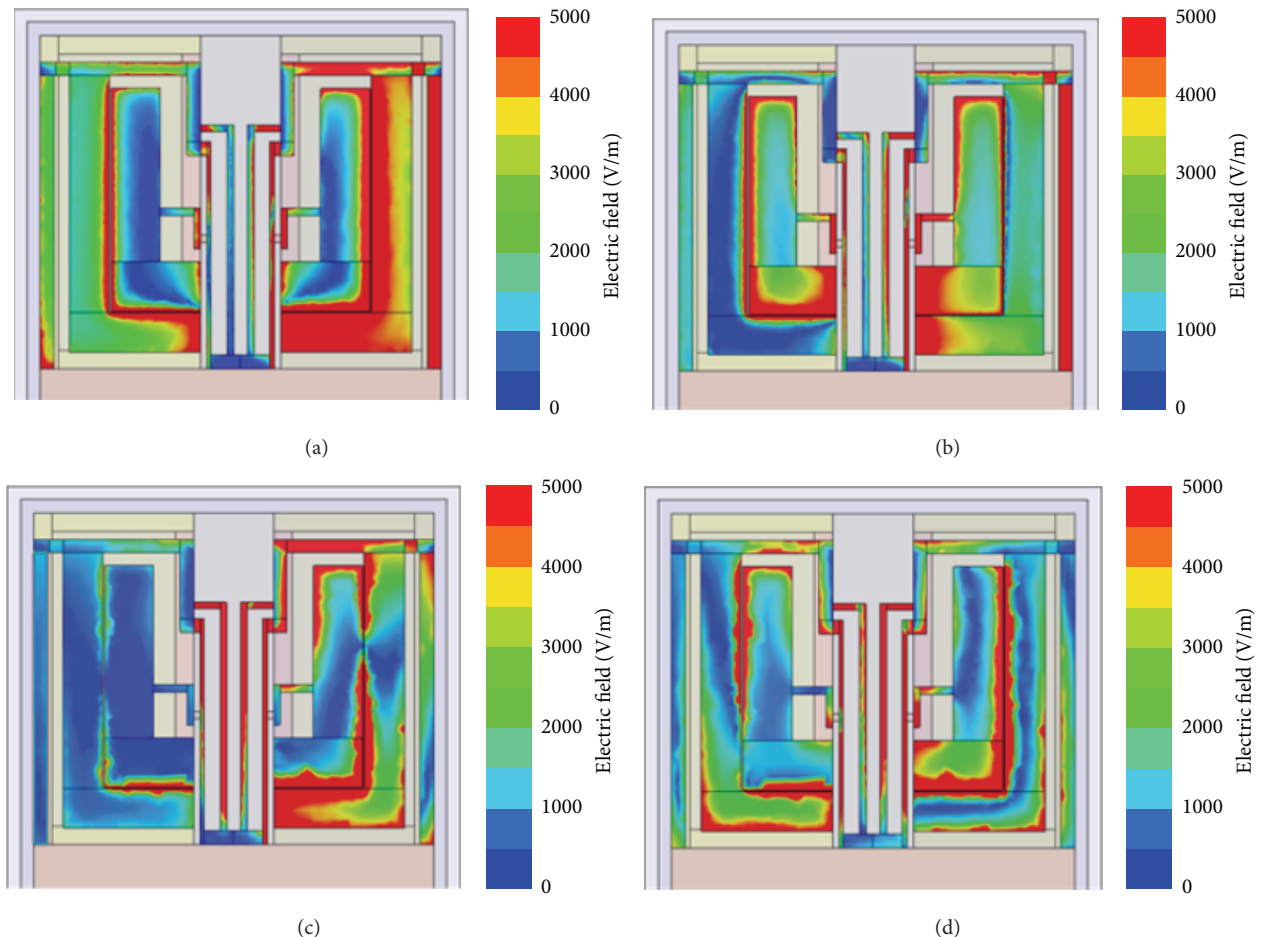


FIGURE 4: Simulated surface electric field distributions of proposed antenna: (a) 790 MHz, (b) 960 MHz, (c) 2500 MHz, and (d) 2690 MHz.

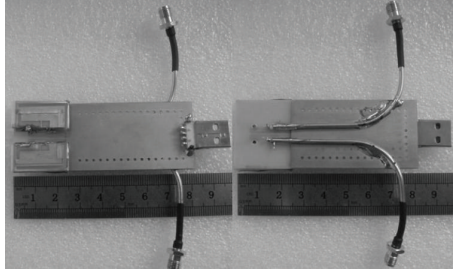


FIGURE 5: Photograph of the fabricated multiband MIMO antenna.

GSM850/900, and LTE band 7, simultaneously. According to Figure 3(b), we can see that there are two left-hand modes peaks occurring at low frequency band and high frequency band, respectively [1]. The left-hand mode at low frequency corresponds to the unbalanced CRLH transmission line, while the left-hand mode at high frequency corresponds to the balanced case [14].

The method of an etching slot is implemented in the MIMO antenna system, as shown in Figure 1(b). The ground between two antenna elements is etched to produce two thin strips which connect the feeding ports and the main ground. The structure is inherently a band-stop filter, which exhibits stop band over its low frequency band. Specifically, two shorting strips can be equivalent to two paralleled inductances and the seam between them can be referred to a capacitance [15]. Furthermore, a pair of L-shaped strips is located between two antenna elements to generate an additional coupling in the LTE band 7 to counteract the original one. The isolation of MIMO system across operating frequency band can be largely improved by using these two methods.

Figure 4 shows the simulated surface electric field distributions at four representative frequency points of 790 MHz, 960 MHz, 2500 MHz, and 2690 MHz, respectively, when antenna 2 is excited with antenna 1 terminated to  $50\Omega$ . It can be seen from Figure 3 that Part 1 and Part 3 are excited as the first ZOR mode at lower band, while Part 1 and Part 2 are excited as the second ZOR mode at higher band. The dual ZOR modes verify the above discussions. In addition, a pair of L-shaped strips located between the two paralleled shorting lines generates an additional mutual coupling at the LTE band 7, according to Figure 4(c).

### 3. Results and Discussions

The proposed multiband MIMO antenna system is fabricated and studied. Photographs of a manufactured prototype are shown in Figure 5. Figure 6 shows the measured S parameters of the MIMO antenna system when the USB dongle is attached to a laptop computer. Due to the dual ZOR modes, the operating bandwidth can simultaneously cover band 13 (746–787 MHz), GSM850/900 (824–960 MHz), and LTE band 7 (2500–2690 MHz), a very wide operation bandwidth. Moreover, according to  $S_{12}$  result in Figure 6, the measured isolation between two antenna elements is less than  $-8\text{ dB}$

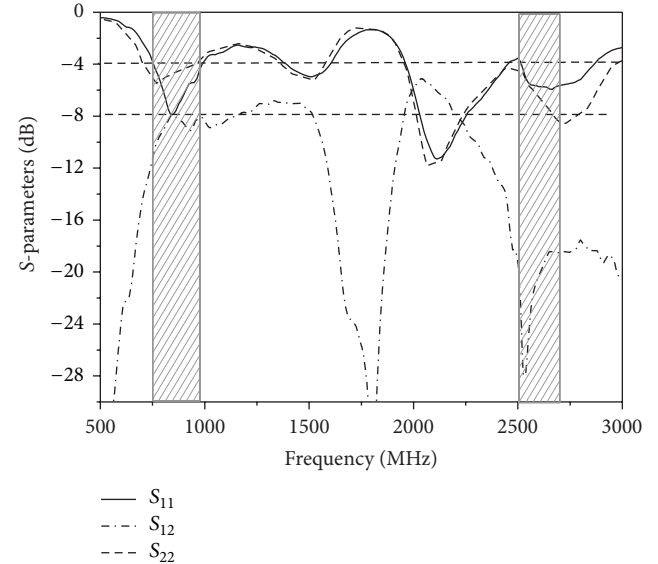


FIGURE 6: Measured S-parameters of the fabricated MIMO antenna.

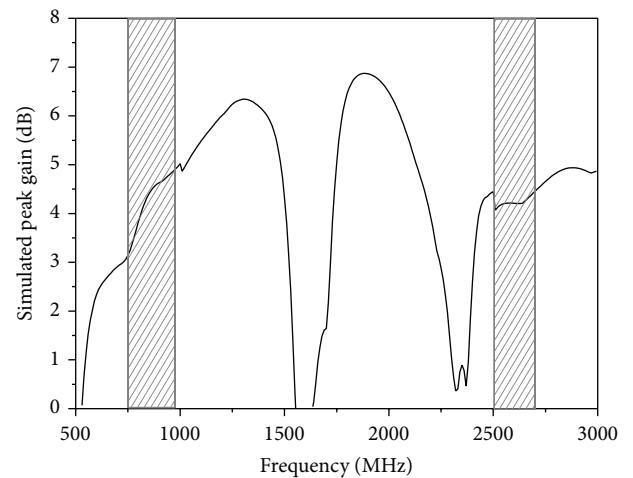


FIGURE 7: Simulated peak gain of the fabricated MIMO antenna.

TABLE 2: Measured total efficiency of antenna 1 and antenna 2.

Frequency (MHz)	768	843	920	2500	2700
Efficiency of antenna 1 (%)	33	41	44	38	52
Efficiency of antenna 2 (%)	21	40	43	41	63

over the lower band and  $-16\text{ dB}$  across the upper band, respectively.

Table 2 shows the measured total efficiency of two antenna elements with unmeasured port terminated in  $50\Omega$  load. The total efficiency of antenna 1 is approximately over 40% across the service band while antenna 2 is a little low at the LTE band 13 (746–787 MHz). This is because of the disturbance of the feed cables and the plastic carriers. Figure 7 shows the simulated peak gain of the fabricated MIMO

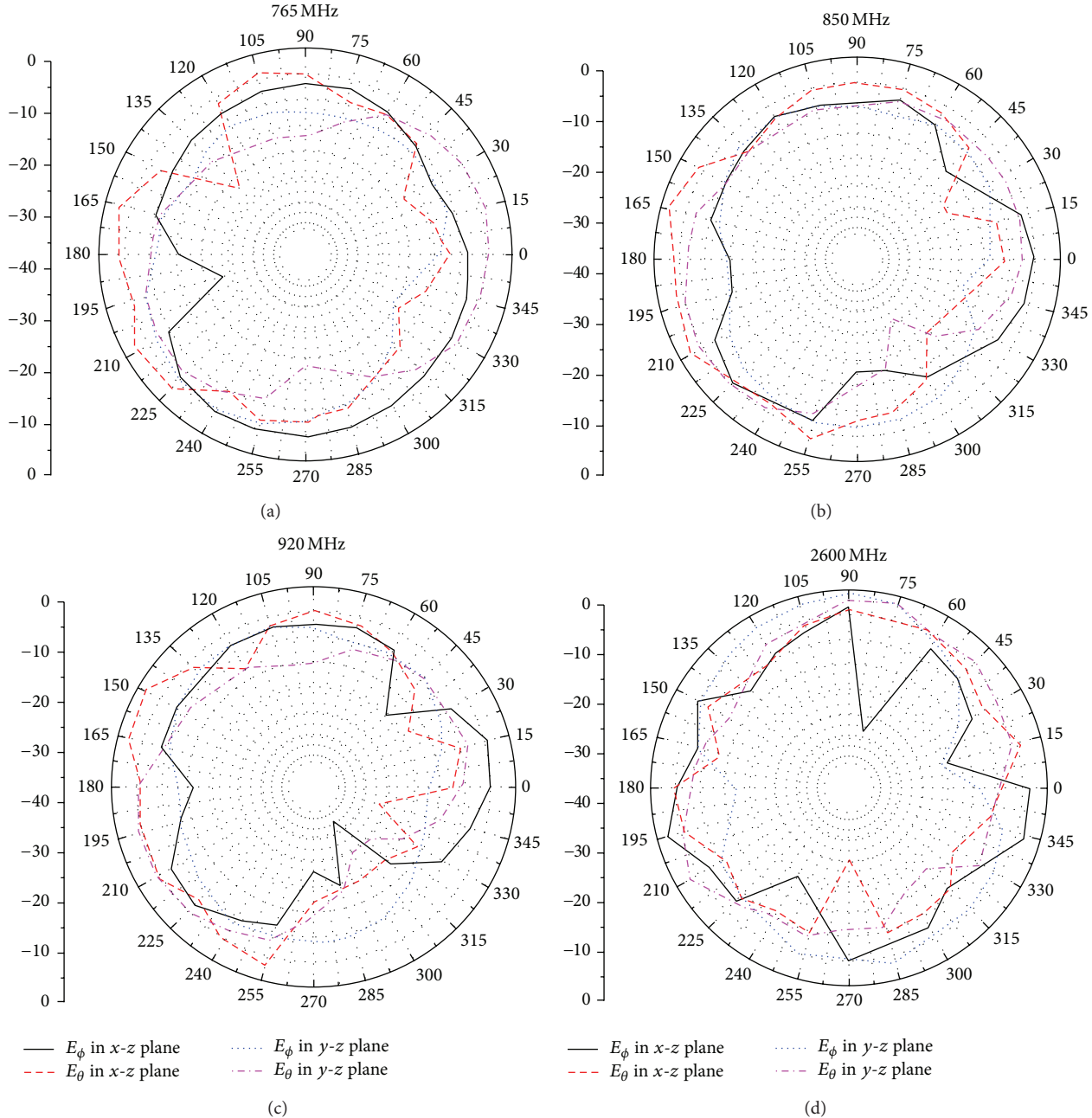


FIGURE 8: Measured two-dimensional radiation patterns of antenna 1 in the MIMO system.

antenna. The peak gain is approximately over 4 dB across the high frequency band and over 3 dB at the low frequency band. Measured two-dimensional radiation patterns of antenna 1 at 765 MHz, 850 MHz, 920 MHz, and 2600 MHz are plotted in Figure 8, respectively. In addition, Figure 9 shows the three-dimensional radiation patterns of two antennas at 890 MHz and 2600 MHz. The measured radiation patterns were not exactly omnidirectional but sufficient for USB dongle services in the service bands.

#### 4. Conclusion

MIMO antenna system with a compact size of  $25\text{ mm} \times 30\text{ mm} \times 3.5\text{ mm}$  covering the LTE band 13 (746–787 MHz), GSM850/900 (824–960 MHz), and LTE 7 (2500–2690 MHz) has been proposed for 4G USB dongle. The proposed antenna element in the MIMO system operates in dual ZOR modes, and thus a wide bandwidth can be obtained. A pair of L-shaped parasitic strips and an etching slot on the ground

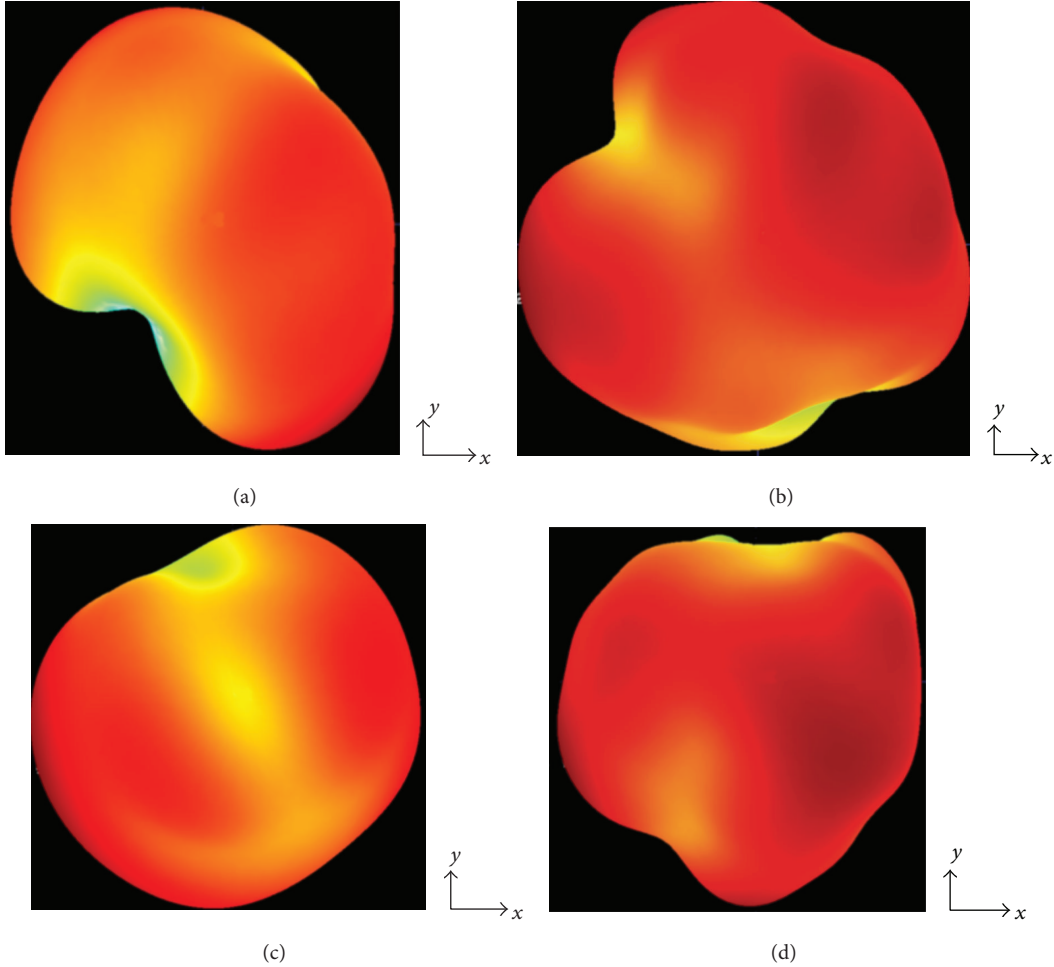


FIGURE 9: Measured three-dimensional radiation patterns of two antennas in the MIMO system: (a) antenna 1 at 890 MHz, (b) antenna 1 at 2600 MHz, (c) antenna 2 at 890 MHz, and (d) antenna 2 at 2600 MHz.

are introduced so that the isolation between two antennas is less than  $-8$  dB over the lower band and  $-16$  dB across the upper band, respectively. Therefore, the proposed antenna is applicable to 4G USB dongle applications due to its small size and good performance for each band.

### Conflict of Interests

The authors declare that there is no conflict of interests regarding the publication of this paper.

### Acknowledgments

This work is supported partly by the Program for the New Scientific and Technological Star of Shaanxi Province (no. 2013KJXX-66), Natural Science Basic Research Plan in Shaanxi Province (nos. 2013JZ019 and 2015JM6292), National Natural Science Foundation of China under Contract no. 51477126, Technology Innovation Research Project of the CETC, and Fundamental Research Funds for the Central Universities (no. SPSZ031410).

### References

- [1] C.-J. Lee, W. Huang, A. Gummalla, and M. Achour, "Small antennas based on CRLH structures: concept, design, and applications," *IEEE Antennas and Propagation Magazine*, vol. 53, no. 2, pp. 10–25, 2011.
- [2] Y. Yu, G. Kim, W. Seong, and J. Choi, "An internal multiband antenna with zeroth-order resonator for USB dongle applications," *Microwave and Optical Technology Letters*, vol. 52, no. 10, pp. 2212–2214, 2010.
- [3] R. A. Bhatti, S. Yi, and S.-O. Park, "Compact antenna array with port decoupling for LTE-standardized mobile phones," *IEEE Antennas and Wireless Propagation Letters*, vol. 8, pp. 1430–1433, 2009.
- [4] S. Zhang, A. A. Glazunov, Z. Ying, and S. He, "Reduction of the envelope correlation coefficient with improved total efficiency for mobile LTE MIMO antenna arrays: mutual scattering mode," *IEEE Transactions on Antennas and Propagation*, vol. 61, no. 6, pp. 3280–3291, 2013.
- [5] K.-S. Min, D.-J. Kim, and Y.-M. Moon, "Improved MIMO antenna by mutual coupling suppression between elements," in *Proceedings of the 8th European Conference on Wireless Technology*, vol. 1, pp. 125–128, Paris, France, October 2005.

- [6] Y. Ding, Z. W. Du, K. Gong, and Z. Feng, "A novel dual-band printed diversity antenna for mobile terminals," *IEEE Transactions on Antennas and Propagation*, vol. 55, no. 7, pp. 2088–2096, 2007.
- [7] A. C. K. Mak, C. R. Rowell, and R. D. Murch, "Isolation enhancement between two closely packed antennas," *IEEE Transactions on Antennas and Propagation*, vol. 56, no. 11, pp. 3411–3419, 2008.
- [8] A. Cihangir, F. Ferrero, G. Jacquemod, P. Brachat, and C. Luxey, "Neutralized coupling elements for MIMO operation in 4G mobile terminals," *IEEE Antennas and Wireless Propagation Letters*, vol. 13, pp. 141–144, 2014.
- [9] M. Karakoikis, C. Soras, G. Tsachtsiris, and V. Makios, "Compact dual-printed inverted-F antenna diversity systems for portable wireless devices," *IEEE Antennas and Wireless Propagation Letters*, vol. 3, no. 1, pp. 9–14, 2004.
- [10] G. A. Mavridis, J. N. Sahalos, and M. T. Chryssomallis, "Spatial diversity two-branch antenna for wireless devices," *Electronics Letters*, vol. 42, no. 5, pp. 266–268, 2006.
- [11] Y.-L. Ban, J.-H. Chen, L.-J. Ying, J. L.-W. Li, and Y.-J. Wu, "Ultrawideband antenna for LTE/GSM/UMTS wireless USB dongle applications," *IEEE Antennas and Wireless Propagation Letters*, vol. 11, pp. 403–406, 2012.
- [12] W.-J. Liao, S.-H. Chang, J.-T. Yeh, and B.-R. Hsiao, "Compact dual-band WLAN diversity antennas on USB dongle platform," *IEEE Transactions on Antennas and Propagation*, vol. 62, no. 1, pp. 109–118, 2014.
- [13] B. Kim, Y. Park, H. Wi et al., "Isolation enhancement of USB dongle MIMO antenna in LTE 700 band applications," *IEEE Antennas and Wireless Propagation Letters*, vol. 11, pp. 961–964, 2012.
- [14] C. Caloz and T. Itoh, *Electromagnetic Metamaterials: Transmission Line Theory and Microwave Applications*, Wiley, New York, NY, USA, 2006.
- [15] M. Han and J. Choi, "Compact multiband MIMO antenna for next generation USB dongle applications," *Microwave and Optical Technology Letters*, vol. 54, no. 1, pp. 246–250, 2012.

## Research Article

# The Communication Solution for LTE System under Radar Interference Circumstance

**Hang Zheng, Yunjie Li, and Yunpeng Zhu**

*School of Information and Electronics, Beijing Institute of Technology, Beijing 100081, China*

Correspondence should be addressed to Yunjie Li; liyunjie@bit.edu.cn

Received 18 November 2014; Accepted 19 January 2015

Academic Editor: Nima Chamanara

Copyright © 2015 Hang Zheng et al. This is an open access article distributed under the Creative Commons Attribution License, which permits unrestricted use, distribution, and reproduction in any medium, provided the original work is properly cited.

The interferences of radar and communication system coexistent environment are analyzed in this paper, and an attractive detection mechanism of the radar video signal and proportional fair scheduling algorithm based on channel sensing are proposed to realize the communication by using radar radiant intermissions. And the simulation is designed based on the proposed model to test this plan. The simulated results show that the packet scheduling algorithm is an excellent candidate for the communication solution for LTE system under radar radiant intermissions.

## 1. Introduction

The Third Generation Partnership Project (3GPP) has launched Long Term Evolution (LTE) of next generation mobile communications on the frequency bands of 1710–1885 MHz, 2300–2400 MHz, and 2500–2690 MHz based on the number 223 resolution of the World Radiocommunication Conference in 2007, as discussed elsewhere [1, 2]. The development of 3GPP LTE has witnessed explosive growth driven by the wireless communication system. In addition, version R9 of LTE has been released in March 2010, which forms executive standard of LTE. At present, the Chinese Mobile Communication Corporation (CMCC) has developed the Time Division Long Term Evolution (TD-LTE) system, which has been tested and utilized in many cities across the whole country.

However, the shortage of spectrum resources becomes an increasingly serious problem for LTE system, especially in high-frequency bands, that is, 2500–2690 MHz. The LTE system with working frequency band of 2500–2690 MHz has interference problems with high power radars in the adjacent frequency band, such as the S-waveband weather radars and air traffic-control radars. When the frequency space between radar and LTE system is not large enough, the radar signal power is so high that the band-pass filter

could not filter out the radar dominant frequency signal to an acceptable degree, in the radar pulse signal duration. And the residuals signal with high amplitude will still interfere with the communication signals. Meanwhile, the radar out-of-band spurious signal falls into filter's pass-band, and it will not be attenuated by the filter, thus causing interference. When the radar works at the same frequency band of LTE system, the radar dominant frequency signals could easily burn through the receiver.

The interferences mentioned above will affect the performance of LTE system and restrict its promotion, as well as the further utilization of these new assigned frequency bands. Therefore, this paper applies the principle of cognitive radio (CR) to study the interference between radar and LTE system, as discussed elsewhere [3–5], and it comes up with a precise detection mechanism of radar video signal to realize spectrum sensing, as well as a proportional fair scheduling algorithm based on channel sensing for spectrum allocation. In the past papers, researchers usually suggested a protection distance between radar and communication system to ensure a "clean" electromagnetism reserve. In this paper, when LTE system is not so far away from radar, LTE system can establish communication in radar radiant intermittent periods, so they can work compatibly with slightly lower data rate and approximate block error rate.

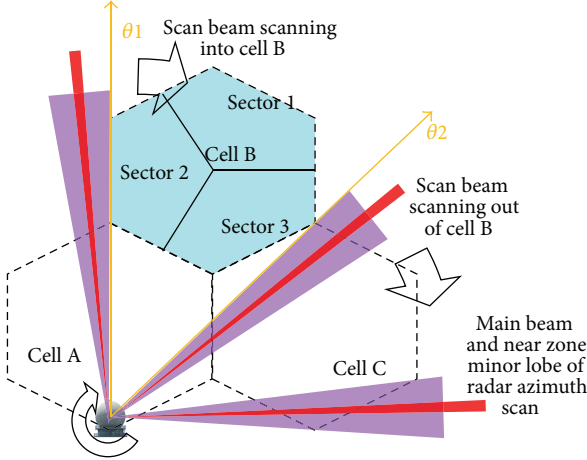


FIGURE 1: Radar and LTE coexistent environment.

TABLE 1: Main technical parameters of weather radar in S-waveband.

Parameters	Value
Working frequency	$2720 \pm 1 \text{ MHz}$
Peak power	650 Kw
Pulse width ( $\tau$ )	1 $\mu\text{s}$ or 4 $\mu\text{s}$
Beam width	1°
Antenna gain	44 dB
Antenna near zone minor lobe	-29 dB (from 2° to 10°)
Antenna far zone minor lobe	-40 dB (over 10°)
Receiver sensitivity	-113 dBm
Intermediate frequency	30 MHz
Pulse repetition time (PRT)	300 Hz, 450 Hz, 600 Hz
Pulse intermittent period (PJ)	$PJ = PRT - \tau$
Polarization mode	Horizontal polarization

## 2. Materials and Methods

### 2.1. Materials

**2.1.1. Basic Characteristics of Target System.** When radar and LTE cells are located as in Figure 1, the main beam and near zone minor lobe of radar will interfere with the receivers of LTE system in varying degree. There are two radar intermissions that can be utilized: the first one is the pulse intermission when radar beam passes over the cell B area and the second one is scanning intermission when radar beam scans out of cell B area.

By requiring from meteorological department, main technical parameters of weather radar can be shown in Table 1, while the parameters of LTE base stations (eNodeBs) and user equipment (UE) can be listed in Tables 2, 3, by looking up related literatures and actual measurements, as discussed in [6]. These parameters can be used to compute the strength of signal, in order to judge interference condition, or calculate intermissions for communication, or be used for simulation.

TABLE 2: Main technical parameters of LTE base station (eNodeB).

Parameters	Value
Working frequency	2500–2690 MHz
Peak power	40 Kw
Antenna gain	16.5 dB
Intersite distance	1000 meters
Antenna near zone upper minor lobe	-16 dB (from 0° to 60°)
Antenna far zone upper minor lobe	-23 dB (over 60°)
Receiver sensitivity	-117 dBm
Horizontal beam width	Consists of multiple 60° beams and covers 360°

TABLE 3: Main technical parameters of user equipment (UE).

Parameters	Value
Working frequency	2500–2690 MHz
Peak power	2 w
Beam mode	Omnidirectional
Antenna gain	0 dB
Receiver sensitivity	-110 dBm

**2.1.2. Interference Analysis on Radar and LTE Coexistent Environment.** According to Friis transmission formula, the receiving power can be calculated by the following formula, which reflects interference signal strength, and it helps in judging whether a certain system is interfered or not:

$$P_r = \frac{P_t G_t}{4\pi R^2 G_{tf}} \frac{G_r \lambda^2}{4\pi G_{rf}} \frac{1}{L_t L_r L_d} \frac{1}{L_j} \frac{1}{Q_t Q_j}. \quad (1)$$

For evaluating whether a LTE system, such as eNodeBs or UE, is interfered with weather radar, it needs to calculate the radar antenna power density in eNodeBs at first, that is,  $P_t G_t / 4\pi R^2 G_{tf}$ , where subscript  $t$  represents radar system,  $P_t$  is the antenna power,  $G_t$  is antenna gain,  $G_{tf}$  means antenna minor lobe, and  $R$  represents distance between radar and LTE system. Then, the signal power received by the LTE system can be computed by  $P_t G_t G_r \lambda^2 / (4\pi R)^2 G_{tf} G_{rf}$ , where subscript  $r$  means LTE system,  $G_r$  is the antenna gain,  $G_{rf}$  is the antenna minor lobe, and  $\lambda$  means radar wavelength. In addition, it needs considering of different transmission losses  $L_t L_r L_d L_j$ , where  $L_t$  and  $L_r$  are antenna feeder losses,  $L_d$  represents maximum multipath signal of radar, and  $L_j$  means polarization mismatching loss of the coexistent system. Finally, it needs computing the different spurious suppressions  $Q_t Q_j$ , where  $Q_t$  is radar spurious suppression at the frequency of LTE system and  $Q_j$  is the out-of-band and filter suppression of LTE system. In this way, the power of radar interference signal received by LTE system can be calculated, and the interference conditions can be defined by comparing with receiver sensitivity.

For instance, when the LTE system is working at 2670 MHz, weather radar works at 2720 MHz, and Tables 4, 5

TABLE 4: Transmitter parameters in meteorological radars (dominant frequency interference).

Parameters	Value
Peak power ( $P_t$ )	88.1 dBm
Gain ( $G_t$ )	44 dB
Minor lobe level ( $G_{tf}$ )	0 dB
Frequency band factor $\lambda^2$	-19.1 dB
Constant $(4\pi)^2$	-21.98 dB
Feeder loss ( $L_t$ )	-3 dB
Maximum multipath signal ( $L_d$ )	0 dB
Distance $R^2$ (300 m)	-49.54 dB
Spurious suppression in LTE's working frequency ( $Q_t$ )	0 dB

TABLE 5: Receiver parameters in LTE base station.

Parameters	Value
Antenna gain ( $G_r$ )	16.5 dB
Minor lobe level ( $G_{rf}$ )	0 dB
Feeder loss ( $L_r$ )	-1.5 dB
Polarization loss ( $L_j$ )	-1.5 dB
Out-of-band spurious and filter suppression ( $Q_j$ )	-150 dB
Receiver sensitivity	-117 dBm

list other related parameters. The interference power received by LTE system can be obtained in decibel by

$$\begin{aligned}
 P_r &= \frac{P_t G_t}{(4\pi)^2 R^2 G_{tf}} \frac{G_r \lambda^2}{G_{rf}} \frac{1}{L_t L_r L_d} \frac{1}{L_j} \frac{1}{Q_t Q_j} \\
 &= 88.1 + 44 + 16.5 - 19.1 - 21.98 - 49.54 - 0 \\
 &\quad - 0 - 3 - 1.5 - 1.5 - 150 \\
 &= -98.02 \text{ dBm},
 \end{aligned} \tag{2}$$

which is higher than the receiver sensitivity of eNodeB with value of -117 dBm; it can foresee that the eNodeB is interfered by the main beam of weather radar within 300 meters away.

When considering other effects including near or far zone minor lobe, multipath echo signal, and different distances, it can be concluded that when the weather radar is within 30 to 2500 meters away from the LTE base station, the LTE system is interfered by radar, while interferences from LTE system to radar can be ignored.

*The Communication Solution in the Coexistent Systems.* After analyzing interference condition, the radar pulse intermissions need to be found for communication; therefore, a precise detection mechanism of radar video signal is designed to realize the spectrum sensing, and a channel-sensing-based LTE packet scheduling algorithm is proposed to approach spectrum access.

**2.1.3. Sensing of Radar Radiant Environment.** The technical parameters of weather radar remain stationary and simple, which also can be detected previously, and it is required for a cognitive system (LTE system) to detect the authorized

users (weather radars) precisely in real time. Therefore, this paper proposes an attractive detection mechanism of the radar video signal based on the matched filter in frequency domain, which can be divided into three parts as shown in Figure 2.

(i) *RF Pilot Frequency Matching Channel.* The first part is the RF pilot frequency matching channel. This channel is imported with the high-frequency signal of the weather radar, and the signal passes through the band-pass filter, RF amplifier, mixer, and analog to digital conversion in turn, to be transformed to digital IF signal.

(ii) *Matching Detection in Frequency Domain.* The second part is the matching detection in frequency domain. The matching detection part is made up of computation modules, such as FFT, square, and threshold comparison.

This part uses spectral transform and computation to detect the radar signal and obtain the frequency and energy of the radar signal, as well as the raw detection of pulse repetition period. Because the energy of spectrum  $E_{FD}$  with central frequency  $f_c$  and bandwidth  $w$  is

$$E_{FD} = \frac{f_s}{2\pi N} \sum_{k=k_1}^{k_2} |x(k)|^2, \tag{3}$$

where  $N$  is the FFT length,  $x(k)$  represents digital radar signal,  $f_s$  means sample rate, and  $k_2$  and  $k_1$  are the upper and lower bounds of frequency points. After comparing with (3) and detection threshold  $\lambda$ , which is detected in the engineering environment, the proposed mechanism can ascertain whether there is authorized signal received in cognitive system receiver by formula (4) and detect the frequency and energy of the authorized signal and make detection on pulse repetition period

$$\begin{aligned}
 E_{FD} &\leq \lambda_1, \text{ (no authorized signal),} \\
 E_{FD} &> \lambda_1, \text{ (1 } \mu\text{s authorized signal),} \\
 E_{FD} &> \lambda_2, \text{ (4 } \mu\text{s authorized signal).}
 \end{aligned} \tag{4}$$

(iii) *Precise Video Signal Detection.* The final part is the precise video signal detection. In this part, the processed radar signal passes through envelope detection, amplifier, threshold detection, and computation modules in turn. As long as the matching detection part detects radar signal, the mechanism can immediately obtain the measurement of pulse start time  $T_{ai}$ , pulse end time  $T_{bi}$ , pulse width  $\tau = T_{bi} - T_{ai}$ , and pulse amplitude  $P_a$ . These parameters are used to ascertain which LTE scheduling period is interfered.

And then, the mechanism can acquire the repetition period of pulse signal by  $T = T_{a(i+1)} - T_{ai}$  and the antenna scanning period  $Q = T_{E_{max}+1} - T_{E_{max}}$ , which is the intermission between the two maximum values of pulse amplitudes measured by statistics. Finally, the scanning intermission is got as  $Q_{jx} = Q - (T_{ai} + \tau - T_{a1})$ .

This sensing mechanism starts sensing when the LTE eNodeB begins working. After the sensing mechanism has

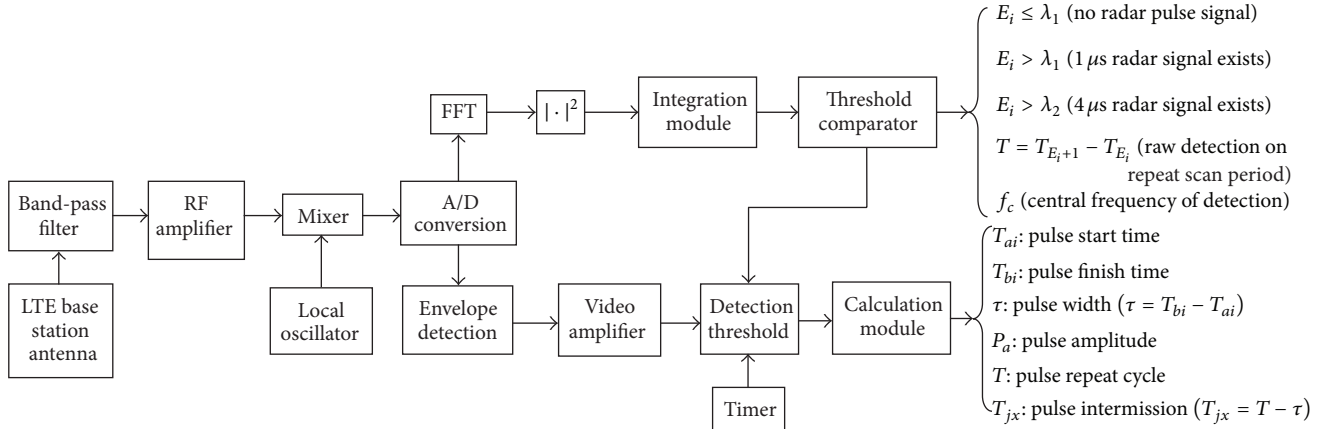


FIGURE 2: Compositions of precise radar detection mechanism.

detected and calculated radar pulse start time  $T_{ai}$ , the scheduler of eNodeB system will use the detected parameters for scheduling. Although radar signal changes within a period length of several microseconds ( $\mu s$ ), the radar radiant sensing scheme should operate precisely to catch changes, which may lead to high time consumption. However, the weather radar does not change its working parameters frequently. Therefore, when sensing scheme has detected and known all parameters mentioned above, the eNodeB system can use these “fixed” parameters for a long period, until the sensing scheme finds the changes in parameters. In this long period, the sensing scheme focuses more on validating interfered periods for eNodeB’s scheduler comparing with the simple precise detection. Hence, the scheduler uses predetected parameters to compute which transmission time interval (TTI) is interfered and skips those TTIs, while sensing scheme detects and tells the latest pulse start time to the eNodeB system, to check whether it skips interference in right TTIs. In this way, tiny time consumption is permitted, and sensing scheme can tell pulse start time to the eNodeB system immediately for validation, which is before completing all other parameters to find out changes and do regularly precise detection at set intervals, for example, half an hour.

**2.1.4. LTE Packet Scheduling Algorithm for Spectrum Access.** Orthogonal frequency division multiple access (OFDMA) system is the downlink multiple access technology of LTE system, and it uses packet scheduling mechanism to allocate subchannels, which can be seen as resource blocks (RBs), to different users. There are three common packet scheduling algorithms, as discussed elsewhere [7], and proportional fair (PF) scheduling algorithm is chosen in this work, because it makes a compromise between system throughput and user fairness.

(i) *Proportional Fair Scheduling Algorithm.* PF scheduling algorithm means every user can obtain equal scheduling opportunities, as discussed elsewhere [8, 9]. In each scheduling period, each user will be assigned a corresponding priority by user’s instantaneous speed  $r_i(n)$  divided by average

speed  $R_i(n)$ , and each subchannel will choose the user with highest priority to transmit data. Hence, if there are  $K$  users who require for transmitting data at scheduling period  $n$ , the chosen user will be

$$i^* = \arg \max_{1 \leq i \leq K} \frac{r_i(n)}{R_i(n)}. \quad (5)$$

After one scheduling period, the average rates of users will be updated as

$$R_i(n+1) = \begin{cases} \left(1 - \frac{1}{T_c}\right) R_i(n) + \frac{1}{T_c} r_i(n), & i = i^* \\ \left(1 - \frac{1}{T_c}\right) R_i(n), & i \neq i^*, \end{cases} \quad (6)$$

where  $T_c$  is a time window parameter.

(ii) *Proportional Fair Scheduling Algorithm Based on Channel Sensing.* Because working frequency of the LTE system is near radar’s operating frequency band, when the radar pulse signal occurs in a certain scheduling period, that is, transmission time interval (TTI), all subchannels in the system will be interfered with radar radiant pulse signal. At this time, all channel qualities are not good enough for users to communicate. Hence, this project adopts channel sensing factor  $A$  to proportional fair scheduling algorithm and makes the channel qualities of all TTIs interfered with pulse signals zero. And then, the scheduler will not assign that channel to that user. Because all channels are interfered, the scheduler will stop working for the TTI and recalculate users’ priority for scheduling in the next TTI. Then PF algorithm will be revised as

$$i^* = \arg \max \{P_i(n)\} = \arg \max \left\{ \frac{r_i(n) * A}{R_i(n)} \right\}, \quad (7)$$

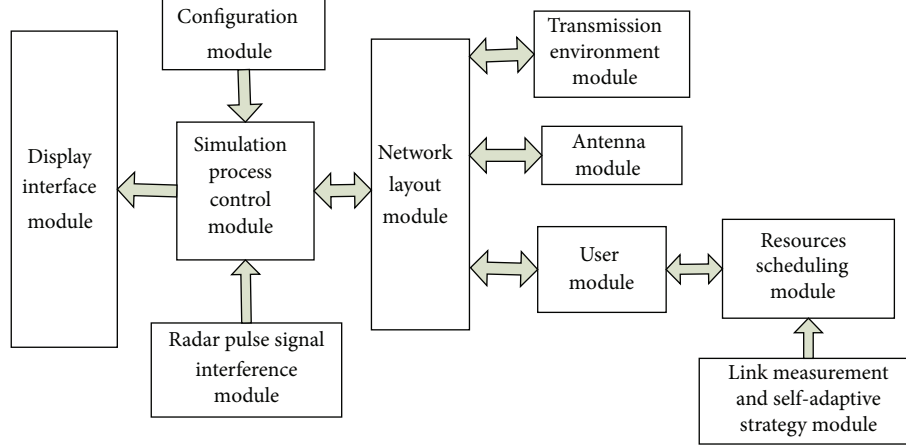


FIGURE 3: Module architecture.

where

$$R_i(n) = \begin{cases} \left(1 - \frac{1}{T_c}\right) R_i(n) + \frac{1}{T_c} r_i(n-1), & i = i^* \\ \left(1 - \frac{1}{T_c}\right) R_i(n), & i \neq i^*, \end{cases} \quad (8)$$

$$A = \begin{cases} 0, & n = n_0 + \left|T_{a1} - T_0 + \frac{a * T}{1000}\right| + b * 1000 * Q \\ 1, & \text{other TTI}, \end{cases} \quad (9)$$

$$a \in \left[0, \left\lfloor \frac{(\theta/360^\circ) * 10^6 * Q}{T} \right\rfloor\right], \quad a \in Z, \quad b \in Z, \quad (10)$$

where  $T_0$  is the start time of the scheduling period  $n_0$  when radar pulse signal occurs for the first time and  $T_{a1}$  is the start time of the first detected pulse signal when radar antenna scanning into sector  $B$ ; then  $T_{a1} - T_0$  is used to find when radar pulse occurs in the TTI.  $T$  is the pulse repetition period,  $a$  represents the pulse number detected by eNodeB within one antenna scan cycle,  $Q$  is the antenna scan cycle, while  $\theta$  is the antenna scan angle over sector  $B$ , and  $\lfloor \cdot \rfloor$  is doing decimals to round down numbers. Therefore,  $a * T/1000$  represents pulse repetition time, and  $|T_{a1} - T_0 + a * T/1000|$  is used to compute the TTI number when radar pulses occur. Besides,  $b$  represents the antenna scan times, and  $b * 1000 * Q$  is computing the time of different antenna scan cycles. In addition, the unit of  $T$ ,  $T_{a1}$  is microsecond ( $\mu s$ ), the unit of  $Q$  is second, and the duration of one TTI is 1ms, which is also the length of scheduling period.

### 3. Results and Discussion

**3.1. System Level Simulation Platform of Radar and LTE Coexistent System.** For the system level simulation platform, it mainly concentrates on problems of scheduling and interference management. The platform is set up by Matlab with ten modules, which can be seen from Figure 3. The main

body of the simulation platform includes the simulation process control module, the configuration module, the radar pulse signal interference module, the network layout module, and the display interface module, while the transmission environment module, the antenna module, and the user module are the submodules of the network layout module. In addition, the link measurement and self-adaptive strategy module provides channel conditions for the resources scheduling module, which belongs to the user module. The simulation mainly concentrates on three modules: the first one is the radar pulse signal interference module to produce interference, the second one is the user module for detecting interference, and the third one is the resources scheduling module to allocate RBs.

Data rate and block error ratio (BLER) are used as evaluation metrics for this simulation platform. Data rate is the transmitted data flow per second, while BLER is the ratio of the number of received error blocks and that of total received blocks.

And the simulation parameters configuration can be seen in Table 6, where some parameters are chosen as discussed elsewhere [10–13]. The users are dropped randomly and immovably in the entire LTE cell, while the traffic model is Full-Buffer, thus simplifying the simulation model.

#### 3.2. Simulation Results and Analysis

**3.2.1. Channel Allocation.** When 10 pieces of UE are assigned to each sector randomly, then RBs allocation can be seen from Figure 4. When the number of RBs assigned to each user decreases to 0, there are special blue broken lines occupying all 25 RBs, which occur in every three or four TTIs. It is a virtual UE piece 0, which represents the scheduler of eNodeB. The RBs assigned to UE piece 0 represent that these RBs are interfered by radar pulse signal at that TTI, and they are not assigned to any real user due to their poor channel quality but reserved by the scheduler itself.

When the first pulse signal starts at 23.211 ms, that is, TTI 23, if the scan period of radar antenna is 1s, the scan angle of the radar antenna over the cell area is 5 degrees;

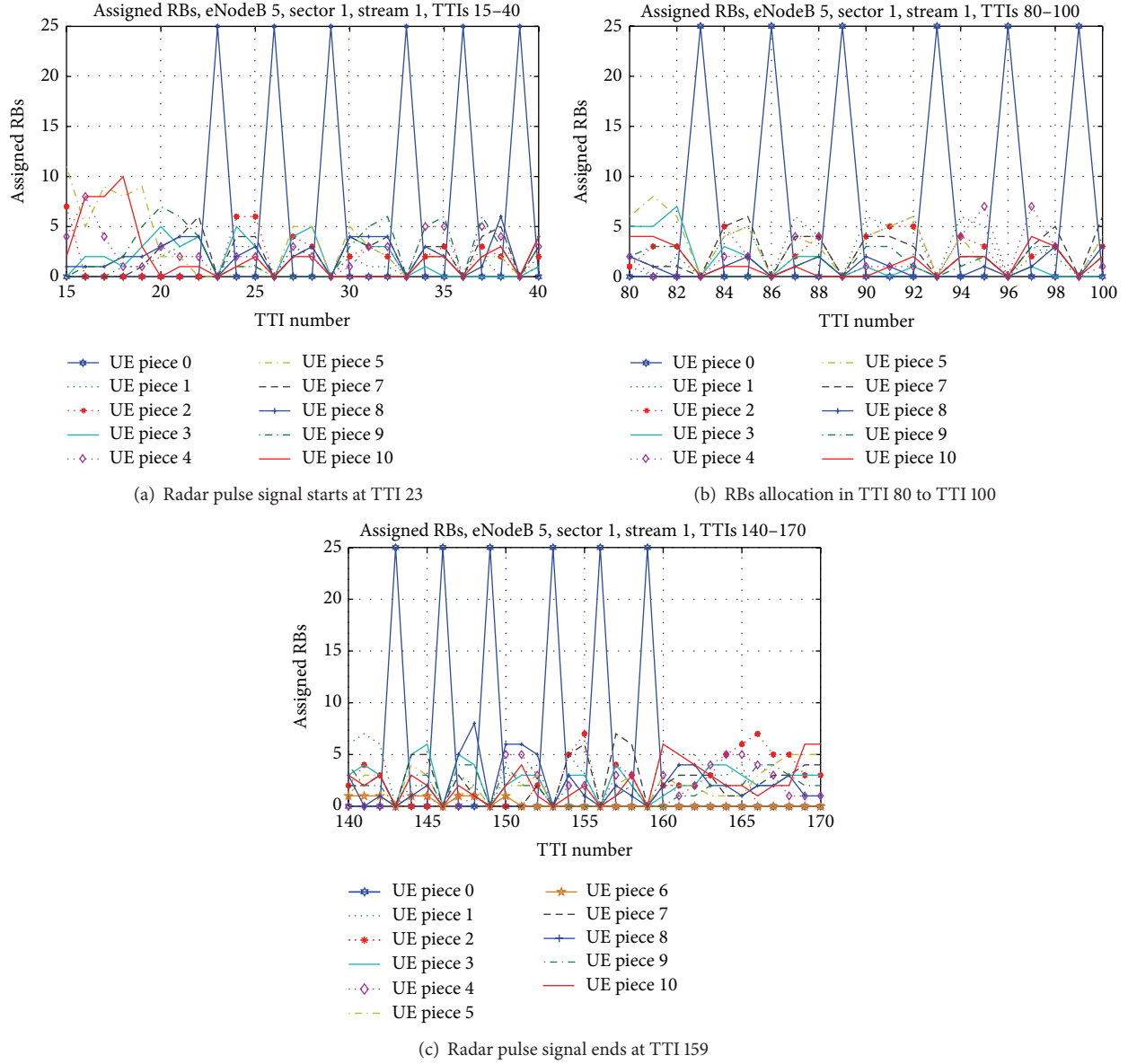


FIGURE 4: Channel allocation with radar pulse signal interference.

then all pulse start times and their corresponding TTIs can be calculated by formula (9), and the results are in accordance with the time when UE piece 0 occurs as shown in Figure 4. Hence, this simulation platform can certainly keep away from the interfered TTIs and then communicate in other TTIs by using precisely detected parameters of radar pulse signal when radar pulse signals occur.

**3.2.2. Data Rate.** By allocating a different number of users in each sector, such as 5, 10, 15, 20, 25, 30 pieces of UE, this platform can obtain the data rate of the entire cell with or without radar interference, as shown in Figure 5.

When 5 users are allocated in each sector, the average data rate of interfered cell is 10.7865 Mbps, while that of cell without interference is 11.023 Mbps. Hence, the attenuation of average data rate is 2.1455%. The attenuation trend increases

with the increase of UE pieces number and is stable to 7%, which is within the acceptable range, as shown in Figure 6. Hence, the simulation results show that the proposed communication scheme for the radar and LTE coexistent system is effective.

In addition, the above data is mainly obtained when radar antenna beam scans over cell B area, as shown in Figure 3, which occupies only a small part of the whole radar antenna scan period. After considering the periods when radar antenna scans over the other directions, the data rate of cell B is not interfered. Therefore, when comparing a normal LTE system (which is not adjacent to a radar), with a LTE system that is affected by radar and that used the presented solution, the data rate of the first and the second case should be the same. And then, the data rate attenuation ratio should decrease a lot in the whole radar antenna scan period.

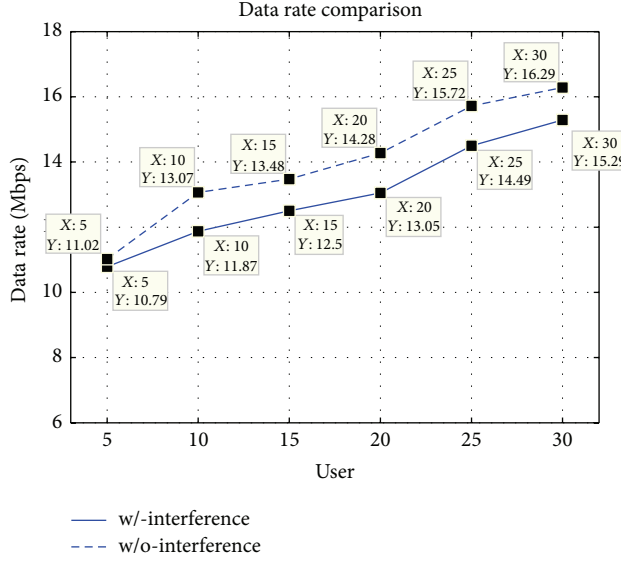


FIGURE 5: Data rate comparison.

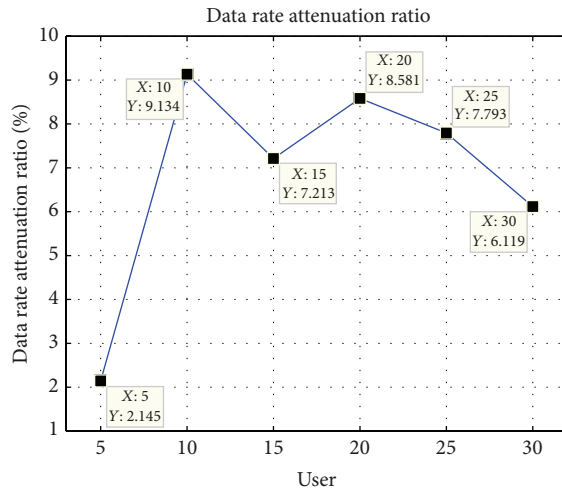


FIGURE 6: Data rate attenuation ration.

**3.2.3. BLER.** By allocating a different number of users in each sector, such as 5 to 30 pieces of UE, the BLER variations can be seen from Figure 7.

When 5 pieces of UE are allocated in each sector, BLER of interfered cell is 0.0467, while that of cell without interference is 0.0482. Hence, BLER gain is 3.3195%. The trend of average BLER gain decreases with increase of UE pieces number, and finally it is stable within 1% range comparing with BLER value of cell without interference.

In general, the BLER of interfered cell is floating slightly around that of cell without interference. Hence, by sensing of radar pulse signal, this communication scheme can make the LTE system keep away from TTIs when radar pulse signals occur. And then, the LTE system can communicate at other TTIs, which will decrease radar influences on BLER.

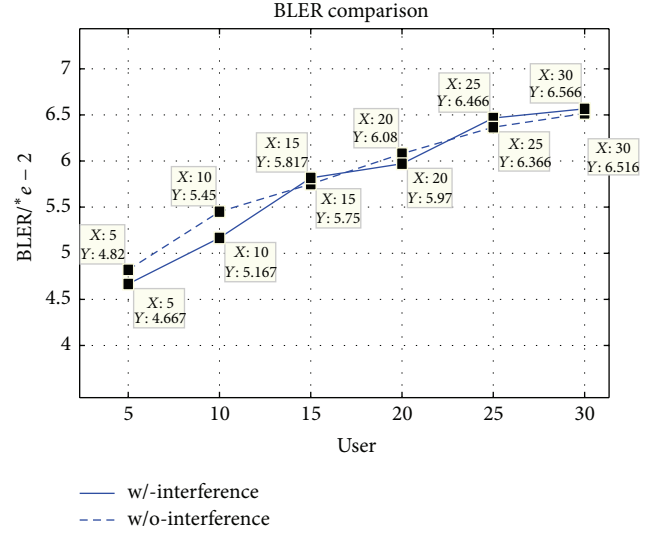


FIGURE 7: BLER comparison.

TABLE 6: Simulation parameters configuration.

Parameters	Value
Cellular layout	Hexagonal grid, 1 cell site, 3 sectors per site
Cell radius	250 m
Traffic model	Full-Buffer [10]
Macroscopic path loss model	TS 36.942 [11]
Fast fading	PedB model
Radar pulse signal repetition period	3.333 ms
UE distribution	Users dropped randomly in entire cell
UE speeds	0
Bandwidth	5 MHz
Simulation length	200 TTIs
TTI length	1 ms
Channel model	Typical urban (TU) [12]

## 4. Conclusions

This paper applies the principle of cognitive radio to interdisciplinary knowledge of radar and LTE system. And then, a communication scheme is proposed, which utilizes radar radiant intermittent periods to realize communication in radar and communication coexistent system. The proposed scheme has been analyzed and the analysis proves that it can keep away from interference of radar pulse signal and communicate in radar pulse intermission according to precisely detected signal parameters. Simulation results show that the data rate attenuation is stable to 7%, while BLER gain is stable within 1%, which proves the effectiveness of the communication scheme.

## Conflict of Interests

The authors declare that there is no conflict of interests regarding the publication of this paper.

## Acknowledgments

In this research, my knowledge of radar and LTE system has improved greatly, and I have learnt many useful learning methods and thinking perspectives to solve problems. All thanks are due to our tutors, Yunjie Li and Zhenglei Huang, and other friends who helped us a lot and encouraged us when we had problems.

## References

- [1] S. Sesia, I. Toufik, and M. Baker, *LTE—The UMTS Long Term Evolution: From Theory to Practice, Including Release 10 for LTE-Advanced*, John Wiley & Sons, New York, NY, USA, 2nd edition, 2011.
- [2] “IEEE standard for safety levels with respect to human exposure to radio frequency electromagnetic fields, 3 kHz to 300 GHz,” IEEE Standard C95.1, 2005.
- [3] J. Mitola III and G. Q. Maguire Jr., “Cognitive radio: making software radios more personal,” *IEEE Personal Communications*, vol. 6, no. 4, pp. 13–18, 1999.
- [4] J. Mitola, *Cognitive radio: an integrated agent architecture for software defined radios [Ph.D dissertation]*, Royal Institute of Technology (KTH), Stockholm, Sweden, 2000.
- [5] S. Haykin, “Cognitive radio: brain-empowered wireless communications,” *IEEE Journal on Selected Areas in Communications*, vol. 23, no. 2, pp. 201–220, 2005.
- [6] F. J. Harris, C. Dick, and M. Rice, “Digital receivers and transmitters using polyphase filter banks for wireless communications,” *IEEE Transactions on Microwave Theory and Techniques*, vol. 51, no. 4, pp. 1395–1412, 2003.
- [7] 3GPP TS 36.814 V9.0.0. Evolved Universal Terrestrial Radio Access (E-UTRA); Further advancements for E-UTRA Physical layers aspects, Dec. 2009.
- [8] C. Suh, S. Park, and Y. Cho, “Efficient algorithm for proportional fairness scheduling in multicast OFDM systems,” in *Proceedings of the IEEE 61st Vehicular Technology Conference (VTC '05)*, vol. 3, pp. 1880–1884, Stockholm, Sweden, June 2005.
- [9] H. Kim, K. Kim, Y. Han, and S. Yun, “A proportional fair scheduling for multicarrier transmission systems,” in *Proceedings of the IEEE 60th Vehicular Technology Conference (VTC-Fall '04)*, vol. 1, pp. 409–413, September 2004.
- [10] R. love, R. Kuchibhotla, A. Ghosh et al., “Downlink control channel design for 3GPP LTE,” pp. 813–818, IEEE, Las Vegas, Nev, USA, March-April 2008.
- [11] 3GPP TR 36.942 V8.1.0, “Technical Specification Group Radio Access Network, Evolved Universal Terrestrial Radio Access (E-UTRA), Radio Frequency (RF) system scenarios,” September 2009.
- [12] H. Asplund, K. Larsson, and P. Ökvist, “How typical is the ‘typical urban’ channel model?” in *Proceedings of the IEEE 67th Vehicular Technology Conference-Spring (VTC '08)*, pp. 340–343, May 2008.
- [13] N. Arsalane, M. Mouhamadou, C. Decroze, D. Carsenat, M. A. Garcia-Fernandez, and T. Monedi  re, “3GPP channel model emulation with analysis of MIMO-LTE performances in reverberation chamber,” *International Journal of Antennas and Propagation*, vol. 2012, Article ID 239420, 8 pages, 2012.